

VORTEX DYNAMICS OF A VORTEX PAIR IN
WALL EFFECT AND FLAPPING AIRFOIL
PROPULSION

A Dissertation

Presented to the Faculty of the Graduate School

of Cornell University

in Partial Fulfillment of the Requirements for the Degree of

Doctor of Philosophy

by

Daniel Joseph Asselin

August 2018

© 2018 Daniel Joseph Asselin

ALL RIGHTS RESERVED

VORTEX DYNAMICS OF A VORTEX PAIR IN WALL EFFECT AND
FLAPPING AIRFOIL PROPULSION

Daniel Joseph Asselin, Ph.D.

Cornell University 2018

Vorticity provides the means to exchange momentum between objects and their surrounding fluid. As such, vorticity can be potentially harmful, as seen in the hazard posed by strong counter-rotating vortex pairs generated behind aircraft in flight. Conversely, the production of strong vortical wakes is beneficial to birds and fish, which exploit their generation to produce thrust. In this work, we will examine two classes of flows in which vorticity plays a key role.

In the first flow, we simulate the trailing vortex pair of an aircraft in a water tank. Such counter-rotating vortex pairs are commonly observed to undergo an instability involving a sinusoidal displacement, which ultimately leads to the generation of a series of large vortex rings. As these trailing vortices are most dangerous when aircraft are in close proximity, such as near the ground, we study the behavior of this instability when it is interrupted by a solid wall. In the presence of the wall, the interaction between the primary vortex pair and secondary vorticity generated in the boundary layer leads to significant topological changes and the production of arrays of smaller-scale vortex rings, the precise configuration of which depends on the extent of development of the instability before wall interaction.

In the second flow, we examine the behavior of an airfoil oscillating with pitching and heaving motions. Many animal studies have shown that such flapping airfoils enable high agility and are also quite effective in producing thrust.

Similar vehicles are under development for applications such as search and rescue, environmental monitoring, and reconnaissance. In order to reduce weight and complexity of the propulsive mechanism, however, we equip the airfoil with an actuator in the heave direction but allow it to pitch passively under the control of a torsion spring. In this system, variation of the spring stiffness and the chordwise pivot location allows control of the vortex wake produced by the airfoil, enabling it to produce either thrust or drag as desired. If these parameters are well selected, performance can even be comparable to that of a system with two actively controlled degrees of freedom.

Finally, the majority of existing studies of flapping airfoils use a fixed incoming flow velocity, achieved either by towing the vehicle at a constant speed or by placing it in a water channel. This imposed velocity does not necessarily correspond to that at which the vehicle would naturally travel, determined by a balance of the vehicle's drag and the thrust produced by the airfoil. Using a cyber-physical fluid dynamics technique, in which force-feedback determines the acceleration of the airfoil in real time, we can simulate self-propulsion for a wide range of heaving and pitching amplitudes. For a given cruising velocity, we determine the combination of pitch and heave that enables the most efficient propulsion and examine the characteristics of the forces and vorticity produced that correspond to this condition.

BIOGRAPHICAL SKETCH

Daniel Asselin grew up in West Springfield, MA, and has been fascinated by anything that flies for most of his life. He attended Worcester Polytechnic Institute, where he earned a B.S. in Aerospace Engineering in 2009 and an M.S. in Mechanical Engineering in 2011. He completed his Ph.D. in Aerospace Engineering at Cornell University in 2018. He is the recipient of the NASA Aeronautics Scholarship and an instrument-rated private pilot.

ACKNOWLEDGEMENTS

There are several people and organizations that deserve special recognition for their roles in helping me to complete this research and degree.

Financial support was generously provided by the NASA Aeronautics Scholarship Program, the Office of Naval Research (Award No. N00014-12-421-0712), and the Air Force Office of Scientific Research (Grant No. FA9550-15-1-0243).

My parents, Mary-Ann and Ron, and my brother, Mike, deserve special recognition for putting up with my near-permanent student status over the past seven years. They have always supported me in whatever endeavors I chose to pursue, and I am very thankful for that.

Two-thirds of this research were made possible by the existence of the cyber-physical fluid dynamics facility, which was designed and built by Andrew Mackowski. I very much appreciated that Andrew was always willing to lend a hand whenever I had questions, even after he completed his work at Cornell.

I am also indebted to Thomas Leweke, Dan Harris, Kevin Fuhr, and Adam Trofa, for constructing, improving, and instructing me on the operation of the vortex generator facility.

Jay Young, Sarah Morris, Riley Schutt, and Phil Alley deserve special recognition as the best friends that I made at Cornell. They have all been valuable sources of support throughout my time there.

I would particularly like to thank Jay for being a fine research partner. We solved many problems with the CPFDF system together over the past several years and survived more than one episode of momentary panic. It is extremely valuable to be able to consult someone else who fully understands the research. Completing this degree would have been far more difficult without him.

Zach Taillefer, though completing his own Ph.D., always found time to listen

and offer advice. I always looked forward to our many conversations and fun times together and am very grateful for his friendship.

Marcia Sawyer and Matt Steel provided invaluable and reliable administrative and facilities support, always handling any request I made of them diligently and efficiently.

I would also like to thank the East Hill Flying Club for allowing me to pursue a passion outside of research and for many valuable lessons in the practical applications of aerodynamics.

Finally, my academic advisor, Charles Williamson, should be acknowledged as the guiding force behind this work. His zealous commitment to excellence in design and presentation has greatly improved my skills in these areas. He also set a professional example that will provide invaluable guidance for the rest of my career.

TABLE OF CONTENTS

Biographical Sketch	iii
Acknowledgements	iv
Table of Contents	vi
List of Figures	vii
List of Tables	xi
List of Publications	xii
1 Influence of a wall on the three-dimensional dynamics of a vortex pair	1
1.1 Introduction	3
1.2 Experimental Details	12
1.3 Two Base Studies in Vortex Dynamics	18
1.4 Modes of Vortex Pair Dynamics Interacting with a Wall	22
1.4.1 Vertical Rings Mode: Secondary-Secondary Vortex Interaction	22
1.4.2 Horizontal Rings Mode: Secondary-Primary Vortex Interaction	30
1.4.3 Large Rings Mode: Vortex Ring-Surface Interaction	38
1.5 Discussion	39
1.5.1 Vortex Dynamics	39
1.5.2 Axial Flow	43
1.6 Discussion of Other Relevant Studies of Vortex-Wall Interactions	47
1.7 Conclusions	51
2 Addition of passive dynamics to a heaving airfoil to improve performance	61
2.1 Introduction	63
2.2 Experimental Methods	72
2.3 Preliminary Studies	81
2.4 [Active Heave]-[Passive Pitch]: Thrust and Efficiency	84
2.5 Passive Pitching: Motion Dynamics	94
2.6 Vortex Dynamics	105
2.7 Conclusions	107
3 Self-propulsion of a pitching and heaving airfoil	116
3.1 Introduction	118
3.2 Experimental Methods	124
3.3 Propulsive Performance	134
3.4 Trajectory Plots	142
3.5 Vortex Dynamics	147
3.6 Chordwise Variation of Angle of Attack	158
3.7 Conclusions	161

LIST OF FIGURES

1.1	Principal instabilities associated with a counter-rotating vortex pair	5
1.2	Crow instability approaching a wall	8
1.3	Vortex generator facility schematic	10
1.4	Motion profile for closing flaps and super-position of two Gaussian vortices	11
1.5	Light sheets used for PIV experiments	15
1.6	Dual light-sheet experiment schematic	16
1.7	Crow instability out of ground effect	19
1.8	Circulation of a vortex pair subject to the unbounded Crow instability, measured at the peak and trough cross sections as a function of time.	20
1.9	Two-dimensional vortices interacting with a wall	21
1.10	Circulation of two-dimensional vortices in wall effect	23
1.11	Flow visualization of primary vorticity in Vertical Rings Mode	25
1.12	Flow visualization of secondary vorticity in Vertical Rings Mode	26
1.13	Late-time development of primary and secondary vorticity in Vertical Rings Mode	27
1.14	Schematic showing principal vortex dynamics of Vertical Rings Mode	29
1.15	Vorticity contours for two-dimensional vortices and Vertical Rings Mode in transverse plane	31
1.16	Vorticity contours and flow visualization for Vertical Rings Mode in horizontal plane	32
1.17	Flow visualization of primary vorticity in Horizontal Rings Mode	33
1.18	Vorticity contours for Horizontal Rings Mode	34
1.19	Vorticity contours and flow visualization for Horizontal Rings Mode in longitudinal plane	35
1.20	Schematic showing principal vortex dynamics of Horizontal Rings Mode	37
1.21	Flow visualization of Large Rings Mode	39
1.22	Amplitude of Crow instability in- and out-of-wall effect	41
1.23	Crow instability plane angle for Vertical Rings Mode	42
1.24	Circulation for Vertical Rings Mode and fully developed Crow instability, in- and out-of-wall effect	44
1.25	Pressure at peak and trough cross sections and circulation for Horizontal Rings Mode	46
1.26	Comparison of primary vorticity of a vortex pair and a vortex ring in wall effect	48
1.27	Comparison of secondary vorticity of a vortex pair and a vortex ring in wall effect	49

2.1	Heaving and pitching motions	64
2.2	Schematic of an actively heaving, passively pitching airfoil	70
2.3	Schematic of cyber-physical fluid dynamics facility	73
2.4	Schematic showing operation of the Cyber-Physical Fluid Dynamics control system	74
2.5	Experiments used to validate the results produced by the CFPD simulation technique	76
2.6	Contours of thrust coefficient vs. Strouhal number and maximum angle of attack	82
2.7	Contours of propulsive efficiency vs. Strouhal number and maximum angle of attack	83
2.8	Thrust coefficient and propulsive efficiency vs. maximum angle of attack for $St = 0.30$ and $h_0/c = 0.75$	84
2.9	Free-body diagram showing the forces and moments acting on the airfoil. In this case, the pivot point is located at the leading edge.	85
2.10	Thrust coefficient vs. frequency ratio for various pivot points . .	87
2.11	Thrust coefficient vs. frequency ratio for upstream pivot locations	88
2.12	Maximum thrust coefficient vs. pivot location	89
2.13	Contours of thrust coefficient as a function of pitching amplitude and pitching phase	90
2.14	Propulsive efficiency vs. frequency ratio for various pivot locations	91
2.15	Comparison of thrust coefficient vs. frequency ratio from current experiments and vortex impulse theory (<i>a posteriori</i> predictions) .	92
2.16	Comparison of thrust coefficient vs. frequency ratio from current experiments and vortex impulse theory (<i>a priori</i> predictions) . . .	94
2.17	Thrust coefficient and propulsive efficiency vs. frequency ratio for various values of reduced frequency	95
2.18	Pitching amplitude as a function of frequency ratio and pivot location for a passively pitching airfoil	96
2.19	Maximum pitching amplitude vs. pivot location from current experiments and predictions from vortex impulse theory	98
2.20	Phase angle as a function of frequency ratio for several pivot locations	99
2.21	Schematic showing the angle of attack produced by pitching and heaving motions	100
2.22	Trajectory, thrust coefficient, and angle of attack of an airfoil pivoting about its leading edge	101
2.23	Trajectory, thrust coefficient, and angle of attack of an airfoil pivoting about its trailing edge	102
2.24	Example to illustrate role of phase angle in determining angle of attack	103
2.25	Long-period and offset pitching behavior of an airfoil pivoting about its trailing edge	105

2.26	Instantaneous vorticity field for an airfoil pivoting about its leading edge	106
2.27	Time-averaged vorticity field for an airfoil pivoting about its leading edge	106
2.28	Instantaneous vorticity field for an airfoil pivoting about its trailing edge	108
2.29	Time-averaged vorticity field for an airfoil pivoting about its trailing edge	109
3.1	Heaving and pitching motions	119
3.2	Schematic of cyber-physical fluid dynamics facility	125
3.3	Schematic showing operation of the CPFDF control system	126
3.4	Example showing that the combination of carriage velocity and water channel flow speed maintain the proper incident flow velocity on the airfoil	128
3.5	Heave-pitch diagram	131
3.6	Contours of propulsive economy	135
3.7	Propulsive economy vs. pitching amplitude for several velocities	136
3.8	Input power from pitching and heaving motions vs. pitching amplitude	137
3.9	Schematic illustrating how the maximum propulsive economy is found	138
3.10	Contours of reduced velocity for $Li = 0.35$ with points of maximum propulsive economy labeled	139
3.11	Contours of reduced velocity for $Li = 0.35$ with points of maximum propulsive economy and minimum transverse impulse labeled	140
3.12	Schematic showing the angle of attack produced by pitching and heaving motions	141
3.13	Contours of maximum angle of attack	142
3.14	Schematic showing three operating conditions to be examined .	143
3.15	Airfoil trajectory, transverse force coefficient, and angle of attack for maximum propulsive economy	145
3.16	Airfoil trajectory, transverse force coefficient, and angle of attack for pure heave	146
3.17	Airfoil trajectory, transverse force coefficient, and angle of attack for high pitching amplitude case	148
3.18	Velocity fluctuations for multiple pitch amplitudes	149
3.19	Vorticity distribution generated for best propulsive economy . .	150
3.20	Vorticity distribution generated by pure heave	151
3.21	Vorticity distribution generated by high pitching amplitude . . .	152
3.22	Circulation generated by three flapping motions as functions of time	153

3.23	Maximum circulation generated by the airfoil as a function of pitching amplitude	154
3.24	Maximum leading edge vortex circulation generated by the airfoil as a function of pitching amplitude	155
3.25	Contours of vorticity showing evolution of leading edge vortex with changing pitch amplitude	156
3.26	Contours of vorticity generated at optimal economy for two different velocities	157
3.27	Schematic illustrating chordwise variation of angle of attack . . .	160
3.28	Chordwise variation of the angle of attack	160

LIST OF TABLES

1.1	Summary of principal modes of wall interaction	53
2.1	Parameters defining each cyber-physical experiment for actively and passively pitching systems.	77
2.2	Non-dimensional parameters for an active heave, passive pitch system.	78
3.1	Three operating points along the $U^* = 3.20$ contour.	143

LIST OF PUBLICATIONS

REFEREED PUBLICATIONS

- ASSELIN, D.J. & WILLIAMSON, C.H.K. 2017 Influence of a wall on the three-dimensional dynamics of a vortex pair. *J. Fluid Mech.* **817**, 339–373.
- ASSELIN, D.J., YOUNG, J.D. & WILLIAMSON, C.H.K. 2018a Addition of passive dynamics to a heaving airfoil to improve performance. *J. Fluid Mech.* (*in preparation*) .
- ASSELIN, D.J., YOUNG, J.D. & WILLIAMSON, C.H.K. 2018b Self-propulsion of a pitching and heaving airfoil. *J. Fluid Mech.* (*in preparation*) .
- WILLIAMSON, C.H.K., LEWEKE, T., ASSELIN, D.J. & HARRIS, D.M. 2014 Phenomena, dynamics and instabilities of vortex pairs. *Fluid Dyn. Res.* **46**, 061425.

CONFERENCE PUBLICATIONS

- ASSELIN, D.J. & WILLIAMSON, C.H.K. 2012 Dynamics of a vortex pair impinging on a horizontal ground plane. *Bull. Amer. Phys. Soc.* **57** (17).
- ASSELIN, D.J. & WILLIAMSON, C.H.K. 2013a Formation of small-scale vortex rings from vortex pairs close to the ground. *Bull. Amer. Phys. Soc.* **58** (18).
- ASSELIN, D.J. & WILLIAMSON, C.H.K. 2013b Vortex pair impinging on a horizontal ground plane. *Phys. Fluids* **24**, 091104.
- ASSELIN, D.J. & WILLIAMSON, C.H.K. 2014 Evolution of vortex pairs subject to the crow instability in wall effect. *Bull. Amer. Phys. Soc.* **59** (20).
- ASSELIN, D.J. & WILLIAMSON, C.H.K. 2015a Evolution of vortex pairs subject to the crow instability in wall effect. *Bull. Amer. Phys. Soc.* **60** (21).
- ASSELIN, D.J. & WILLIAMSON, C.H.K. 2015b Vortex pair impinging on a horizontal ground plane. In *Fluid-Structure Interactions and Vortex Dynamics in Aerodynamics*. Porquerolles, France.
- ASSELIN, D.J., YOUNG, J.D. & WILLIAMSON, C.H.K. 2016 Performance of active and passive control of an airfoil using cpfd. *Bull. Amer. Phys. Soc.* **61** (20).
- ASSELIN, D.J., YOUNG, J.D. & WILLIAMSON, C.H.K. 2017 Addition of passive dynamics to a flapping airfoil to improve performance. *Bull. Amer. Phys. Soc.* **62** (14).
- YOUNG, J.D., ASSELIN, D.J. & WILLIAMSON, C.H.K. 2016 Implementation of cpfd to control active and passive airfoil propulsion. *Bull. Amer. Phys. Soc.* **61** (20).
- YOUNG, J.D., ASSELIN, D.J. & WILLIAMSON, C.H.K. 2017 Self-propulsion of a flapping airfoil using cyber-physical fluid dynamics. *Bull. Amer. Phys. Soc.* **62** (14).

CHAPTER 1
INFLUENCE OF A WALL ON THE THREE-DIMENSIONAL DYNAMICS
OF A VORTEX PAIR

Abstract

In this research, we are interested in perturbed vortices under the influence of a wall or ground plane. Such flows have relevance to aircraft wakes in ground effect, to ship hull junction flows, to fundamental studies of turbulent structures close to a ground plane, and to vortex generator flows, among others. In particular, we study the vortex dynamics of a descending vortex pair, which is unstable to a long-wave instability (Crow, 1970), as it interacts with a horizontal ground plane. Flow separation on the wall generates opposite-sign secondary vortices which in turn induce the “rebound” effect, whereby the primary vortices rise up away from the wall. Even small perturbations in the vortices can cause significant topological changes in the flow, ultimately generating an array of vortex rings which rise up from the wall in a three-dimensional “rebound” effect. The resulting vortex dynamics are almost unrecognizable when compared to the classical Crow instability.

If the vortices are generated below a critical height over a horizontal ground plane, the long-wave instability is inhibited by the wall. We then observe two modes of vortex-wall interaction. For small initial heights, the primary vortices are close together, enabling the secondary vortices to interact with each other, forming vertically oriented vortex rings in what we call a “Vertical Rings Mode.” In the “Horizontal Rings Mode,” for larger initial heights, the Crow instability develops further before wall interaction; the peak locations are farther

apart and the troughs closer together upon reaching the wall. The proximity of the troughs to each other and the wall increases vorticity cancellation, leading to a strong axial pressure gradient and axial flow. Ultimately, we find a series of small, horizontal vortex rings which “rebound” from the wall. Both modes comprise two small vortex rings in each instability wavelength, distinct from Crow instability vortex rings, only one of which is formed per wavelength. The phenomena observed here are not limited to the above perturbed vortex pairs. For example, remarkably similar phenomena are found where vortex rings impinge obliquely with a wall.

1.1 Introduction

We study the approach of a vortex pair to a wall, in the case where the vortices are perturbed by a long-wavelength instability. The instability takes the form of a sinusoidal perturbation along the span of the vortices. This causes some regions of the vortex to encounter the wall before other regions, leading to dramatic changes in the vortex topology and the generation of many small-scale coherent structures. While we specifically examine vortices subject to the long-wave instability, the results we present are relevant to many flows in which vortices experience small perturbations close to a boundary, such as vortex rings approaching a boundary obliquely or initially two-dimensional vortices approaching a wavy wall, among other examples.

The study of vortex-wall interactions has relevance to many practical flows in both fundamental fluid mechanics and practical engineering applications. The presence of coherent vortical structures is vital to the energy cascade in turbulent flows, as is discussed extensively in the reviews of Cantwell (1981), Robinson (1991), and Panton (2001). Furthermore, a vortex whose axis is parallel to a bounding wall generates a boundary layer at the surface. As fluid is pushed between the vortex and the wall, this boundary layer is subject to an adverse pressure gradient and can separate, rolling up into a secondary vortex as shown by Harvey & Perry (1971). The presence of the secondary vortex can lead to distinctly complex dynamics. In fact, experiments have demonstrated that structures resembling vortex rings can exist in the boundary layer and evolve into much more complex vortical structures (Chu & Falco, 1988).

The most well-known application of such a flow is the vortex wake gener-

ated by an aircraft, which is the subject of an extensive review by Spalart (1998). All wings generating lift produce a sheet of streamwise vorticity in their wake which ultimately rolls up into a strong counter-rotating vortex pair, although the near-wake can comprise other vortex configurations. This trailing vortex phenomenon is particularly important in the context of airport operations, where many large aircraft operate in close proximity to each other and to the ground. Small aircraft following heavy, transport-class aircraft for takeoff and final approach are subject to uncommanded rolling moments induced by the rotation of these trailing vortices which can, in some cases, pose a significant hazard. The need to avoid such situations leads to constraints on runway and airport capacity.

In some cases vortices near boundaries are used to modify aircraft performance rather than pose a hazard. Vortex generators are positioned on aircraft wings in order to adjust their stall behavior by manipulating the turbulent boundary layer, thereby delaying separation. Beyond aviation, the interaction of vorticity with surfaces is relevant to any situation in which streamwise vorticity is generated near solid bodies. The flow around submersible vehicles and their appendages and control surfaces is one such application, and research into methods of accelerating the destruction of the vortex wake in order to enhance stealth has been conducted (Quackenbush *et al.*, 1996).

Counter-rotating and co-rotating vortex pairs are subject to several instabilities, which have recently been reviewed by Leweke *et al.* (2016). There have been a considerable number of studies of such flows due to their practical aerodynamic applications. The well-known Crow instability (Crow, 1970) is often observed behind real aircraft due to the presence of condensation trails at high

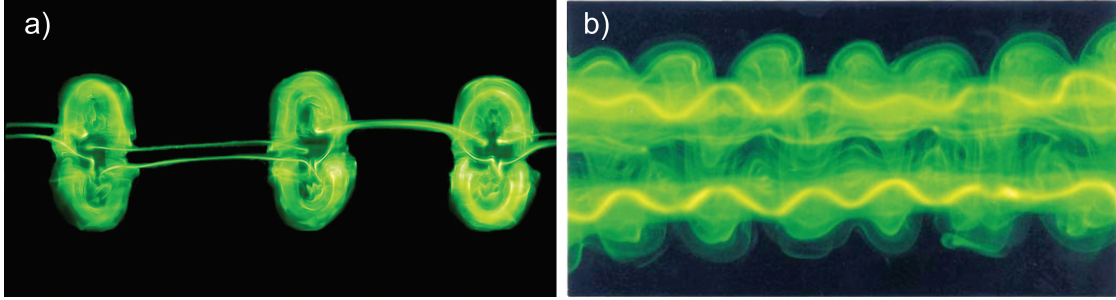


Figure 1.1: The principal instabilities associated with a counter-rotating vortex pair. (a) Long-wave Crow instability. (b) Short-wave elliptic instability (Leweke & Williamson, 1998). (Note that the images are not to the same scale.)

altitudes. This phenomenon causes a pair of initially straight vortex tubes to become sinusoidally displaced in an axisymmetric fashion with a wavelength several times that of the vortex spacing (see figure 1.1a) and eventually to undergo a reconnection process. Ultimately, a periodic series of vortex rings is formed. Reconnection has been studied computationally by a number of authors, including Melander (1988), Melander & Hussain (1988), and Shelley *et al.* (1993), analyzed by Saffman (1989), and reviewed by Kida & Takaoka (1994). The Crow instability has also been observed in experiments performed in the laboratory (Leweke & Williamson, 2011), as shown in figure 1.1(a). Experimental studies show remarkable similarity to full-scale aircraft wakes observed in the atmosphere, despite several orders of magnitude difference in Reynolds number. In this work, we observe significant changes in vortex topology upon interaction of the Crow instability with a solid surface; however, the extent to which these changes exist at higher Reynolds numbers is presently unknown.

Crow's instability theory was later extended to unequal-strength vortex pairs, which were also shown to be unstable for any ratio of vortex circulations (Klein *et al.*, 1995). This situation commonly arises when real aircraft deploy flaps during takeoff or landing and has been studied numerically by Crouch

(1997). Crouch models the vortex wake as a system of two vortex pairs: for each wing, one vortex is generated by the wingtip and one by the flap. This vortex system exhibits both long-wavelength and short-wavelength instabilities which are dependent on the vortex spacing and core size and the circulation ratio between the vortices in each pair. This scenario has also been examined experimentally by Ortega *et al.* (2003) in which a wing equipped with adjustable flaps was towed in a towing tank. The flaps could be configured in a variety of ways to produce vortices of different strengths relative to vortices generated at the wingtip. Several scenarios emerge: in one case, the flap vortex deforms into a series of Ω -shaped loops. Ultimately, these loops can reconnect with part of the tip vortex, yielding a series of vortex rings.

In addition to the long-wavelength Crow instability, counter-rotating vortex pairs are also subject to an instability of shorter wavelengths. Widnall *et al.* (1974) found that perturbations of a more complex structure can cause deformations within the vortex core to grow. This growth occurs when the rotation rate of the plane containing the perturbation, which is caused by its self-induced motion and effects induced by the presence of the other vortex, becomes zero. Subsequently, the perturbation is amplified by the strain rate field of the other vortex. This instability is often referred to as an elliptic instability since two-dimensional flows with elliptic streamlines become unstable in the presence of three-dimensional perturbations, as demonstrated by Bayly (1986), Pierrehumbert (1986), and Waleffe (1990). This instability was observed experimentally in the case of vortex pairs by Leweke & Williamson (1998), as shown in figure 1.1(b), who also discovered that the instability develops with a distinct anti-phase relationship between the two vortices.

In the present work, we consider the approach of a counter-rotating vortex pair to a wall. Line vortex pairs were investigated by Lamb (1932), in which he calculated that the vortices would move away from each other along hyperbolic trajectories as they approach a wall. Dee & Nicholas (1968) measured the actual trajectories of aircraft wake vortices and observed that they appeared to rebound away from the surface instead of continuing on an ideal hyperbolic trajectory. This effect was explained by Harvey & Perry (1971) and further analyzed by Peace & Riley (1983). The rebound of the primary vortices is a consequence of the generation of secondary vorticity at the wall. A vortex approaching a wall creates a boundary layer between itself and the wall that is subject to an adverse pressure gradient. The vorticity contained in the boundary layer then separates and rolls up into a discrete secondary vortex of the opposite sign, which then induces an upward velocity on the primary vortices, significantly changing their trajectories.

These secondary vortices are themselves subject to an instability of the Crow type in which the entire vortex tube is displaced. This instability was simulated by Luton & Ragab (1997), in which they observed the weaker secondary vortex to become wrapped around the stronger primary vortex and concluded that the instability was of the elliptic type. Other research groups including Moet (2003), Georges *et al.* (2006), and Duponcheel *et al.* (2007) reached the same conclusion. Experimental evidence of the existence of this secondary vortex instability was provided by Harris & Williamson (2012) in which they observed bending of the entire secondary vortex tube. Comparison of the measured instability wavelength with that predicted from stability theory indicates that, at low Reynolds numbers, a displacement-type instability mode is principally responsible for the vortex dynamics rather than a higher-order elliptic instability, though it is pos-

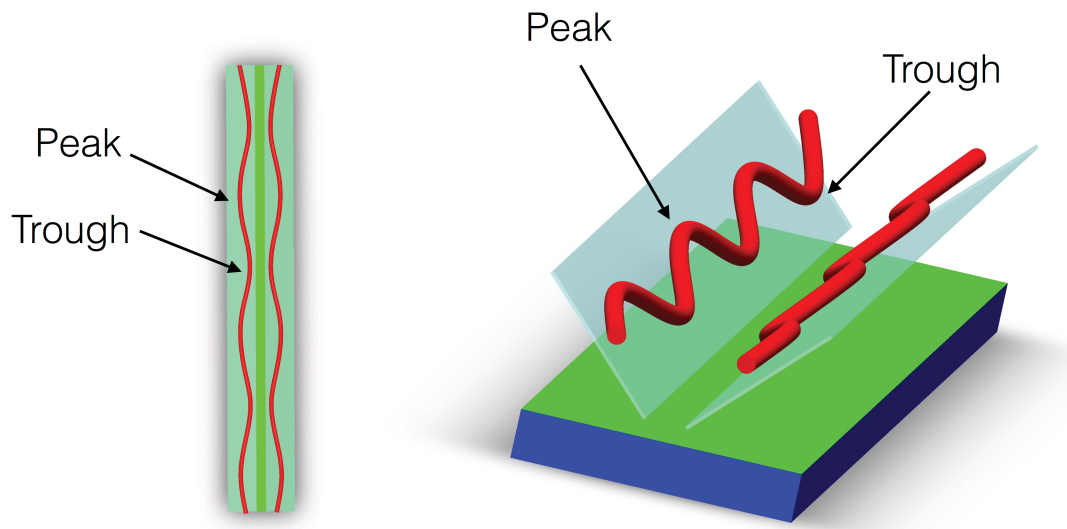


Figure 1.2: Schematic showing the approach of a vortex pair subject to the Crow instability to a wall. The Crow instability causes an initially straight vortex pair to develop a sinusoidal waviness with distinct “peak” and “trough” regions in a plane inclined at about 45° to the horizontal.

sible that an elliptic instability might become dominant at early times at higher Reynolds numbers, as discussed in Williamson *et al.* (2014) and Leweke *et al.* (2016).

The formation of secondary vorticity can have a significant influence on the later evolution of the primary vorticity. The rebound effect and the above instabilities are the most obvious initial phenomena to be found in this flow. In fact, this effect can occur more than once, as demonstrated through computations by Orlandi (1990), who showed that the secondary vorticity can be advected around the primary vortex for more than one revolution. Kramer *et al.* (2007) studied the interaction of a vortex dipole with a wall and demonstrated that multiple eruptions of secondary vorticity from the wall can occur, which strongly influence the trajectory of the primary vortex pair. A similar effect has also been observed for the collision of a vortex ring with a wall, in which

multiple secondary rings are generated and then ejected from the wall (Walker *et al.*, 1987), in some cases forming loop-like structures. The wavy instability of the secondary vortex ring was also observed numerically by Swearingen *et al.* (1995). Further studies of vortex rings in wall effect were conducted by Lim (1989) in which the collision was oblique, meaning that the ring's trajectory was not normal to the boundary. Rather than expanding in an axisymmetric fashion, as is the case for a normal (perpendicular) collision with the wall, the ring experienced significant axial flow away from the region of first contact with the wall (i.e. the location where secondary vorticity is first generated). Ultimately, one observes a secondary vortex loop lifting up away from the wall. This structure contains many features that bear a remarkable resemblance to the present experiments involving counter-rotating vortex pairs subject to the long-wave instability in wall effect.

The experiment conducted by Lim (1989), in which an oblique collision of a vortex ring with a wall was studied, was also simulated by Verzicco & Orlandi (1994). In their simulation, a similar ejection of a secondary vortex structure was observed, which they explain as a consequence of the interaction of vortex stretching and viscous annihilation. The part of the ring interacting with the wall first experiences a high rate of stretching, which leads to a local intensification of vorticity and the generation of secondary vorticity at small scales. The secondary vorticity annihilates the primary vortex through viscous vorticity cancellation. Ultimately, enough vorticity is canceled in this region to produce a locally high pressure relative to the rest of the ring. Fluid is then advected by this pressure gradient to the part of the ring furthest from the wall, where it coalesces into a loop-like structure.

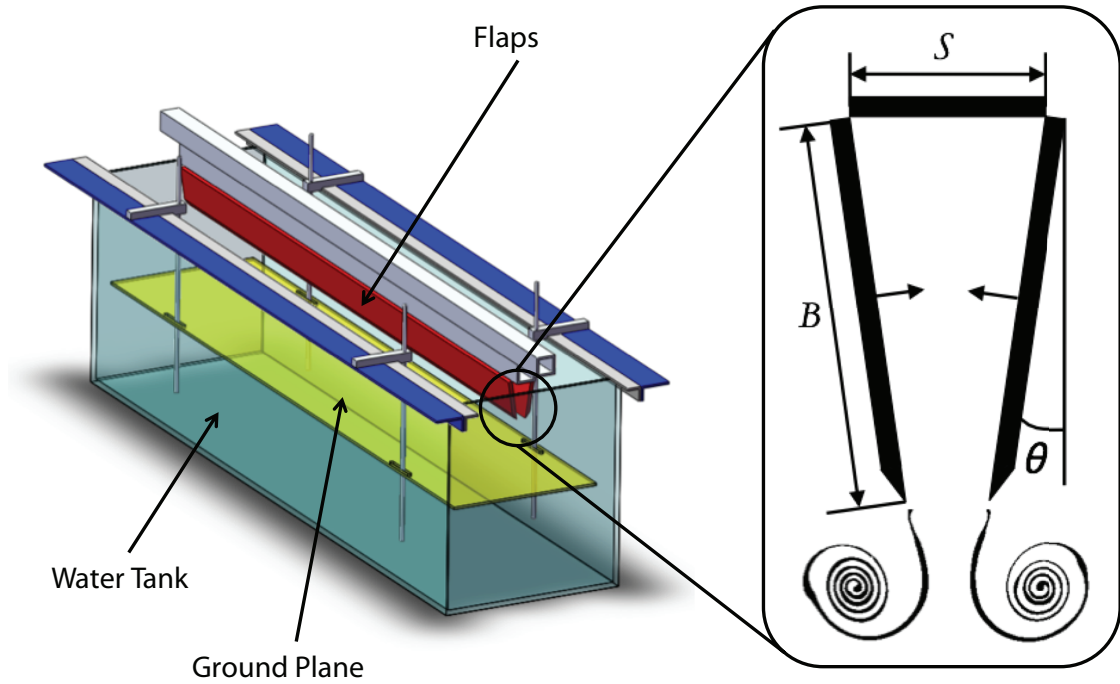


Figure 1.3: Schematic of the vortex generator facility.

The manipulation of secondary vorticity might also serve as a practical method for accelerating the decay of the primary vortices. From our own experiments, we see that a rapid decrease in circulation occurs upon wall interaction. Stephan *et al.* (2013) have simulated the approach of a counter-rotating vortex pair to a wall containing a large rectangular obstacle. The obstacle is positioned such that it transects both descending vortices. Secondary vorticity is produced there first and then forms an Ω -shaped loop. Simultaneously, the circulation of the primary vortices decreases dramatically as a result of the primary-secondary interaction. Other researchers have sought to engineer the vortex wake to keep the trailing vortices in a region of high strain (Rennich & Lele, 1999). For example, if the wake trailing an aircraft equipped with flaps is modeled with four vortices, two shed from the wingtips and two from the flaps, the inboard flap vortices could be kept in the strain field of the wingtip vortices by adjusting their relative strengths. If this is achieved, a Crow-type instability can grow

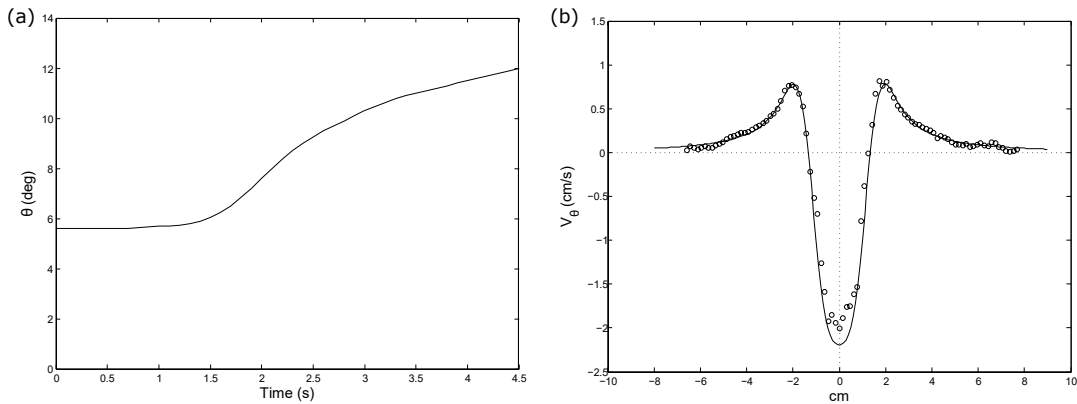


Figure 1.4: (a) The motion profile used for closing the flaps, based on that developed by Leweke & Williamson (2011). (b) A least-squares best fit of the superposition of two Gaussian vortices to the measured azimuthal velocity profile.

very rapidly. The strain field of these perturbed vortices then induces a similar displacement-type perturbation on the stronger wingtip vortices, leading to accelerated destruction of the vortex wake. Analysis by Fabre & Jacquin (2000) shows that the growth rate can be much larger than that of the Crow instability alone. Crouch (2005) also describes several schemes involving purposeful oscillations in the lift distribution that can be used to accelerate vortex decay. The lift oscillations cause perturbations in the spatial position of the trailing vortices which cause them to approach each other. If the frequency of the lift oscillations is properly selected to excite a long-wave instability, then the vortices will pinch off into a series of vortex rings. Measurements indicate that this configuration poses much less risk to aircraft at closer following distances (Crouch, 2005).

The present study specifically examines the interaction of a counter-rotating vortex pair subject to the Crow instability with a wall. The vortex pair is displaced from its initial position and develops distinct “peak” and “trough” regions (see figure 1.2) before it encounters a solid boundary. We present experimental methods in §1.2, followed by §1.3, which provides overviews of two

fundamental flows, namely the Crow instability and the interaction of a two-dimensional vortex with a wall. These fundamental base flows are later compared with the behavior of a counter-rotating vortex pair in the presence of a wall. In §1.4, we present the topological changes produced when the vortices subject to the Crow instability encounter a solid boundary. These changes include the reorganization of the vorticity into a series of smaller rings which then rebound from the surface. The presence of these rings is observed from flow visualization experiments and confirmed by PIV measurements. In §1.5, we present quantitative measurements of parameters describing the evolution of the vortices as they interact with the wall. These measurements include the trajectories followed by the vortices, the amplitude and angular orientation of the instability, and the circulation as a function of time at several axial positions along the vortex. Axial flow along each vortex tube is an important feature of the phenomena we describe, and we discuss evidence for the presence of this flow and describe its driving mechanisms. Importantly, the phenomena we observe are not limited to the flow studied, and in §1.6, we discuss other flows involving perturbed vortices close to a wall which develop structures similar to those associated with the long-wave instability in wall effect. Conclusions follow in §1.7.

1.2 Experimental Details

Experiments are conducted at Cornell University's Fluid Dynamics Research Laboratories using a Vortex Generator Facility. This facility was originally constructed by Thomas Leweke, as described in Leweke & Williamson (1998), and has since been modified to improve the reliability and repeatability of the ex-

periments. The facility consists of a rectangular glass water tank of dimensions 180 cm x 45 cm x 60 cm. A schematic of the facility is shown in figure 1.3. A horizontal pair of aluminum flaps, which are hinged to a rectangular base and driven by a stepper motor, is lowered into the water using a separate system of lead screws and stepper motors. The flaps are 170 cm long, so that they extend to almost the entire length of the water tank. In order to ensure repeatability of the experiment, the Crow instability is triggered by including a very small (1-mm amplitude) sinusoidal perturbation on the lower edges of the flaps (see also Leweke & Williamson, 2011). The perturbation causes the peaks and troughs of the instability to develop in the same spanwise locations during each experiment, allowing the accurate placement of light sheets and cameras for investigation of flow features. In addition, the facility includes a horizontal transparent acrylic ground plane whose vertical position and angle can be adjusted using manual lead screws. The vortex pair encounters this horizontal wall during its descent in the tank. In each experiment, care was taken to ensure that the vortex generation process was unaffected by the presence of the wall. We determined the minimum height above the ground plane at which this is true, and all experiments were begun above this height.

The counter-rotating vortex pair is formed by closing the flaps (shown in figure 1.3) underwater. Fluid is forced out through the gap between the flaps as they are closed, and the shear layers generated roll up into a vortex pair. The profile used to define the motion of the edges of the flaps was defined empirically by Leweke & Williamson (2011) in order to produce laminar vortex pairs and is shown in figure 1.4(a). Helpfully, the vortex pairs produced by this facility are well modeled by a superposition of two Lamb-Oseen (Gaussian) vortices, as shown in figure 1.4(b). The azimuthal velocity profile for a Lamb-Oseen vor-

tex is given by

$$v_{\theta}(r) = \frac{\Gamma}{2\pi r} \left[1 - \exp\left(-\frac{r^2}{a^2}\right) \right] \quad (1.1)$$

where Γ is the vortex circulation, r is the distance measured from the vortex center, and a is a parameter characterizing the vortex core size.

This flow was investigated using several techniques, including both fluorescent dye visualization and particle image velocimetry (PIV). For flow visualization, a mixture of fluorescein dye and water is painted onto the flaps prior to running the experiment. This dye then marks the primary vorticity that is generated by the flaps. Illumination, which could be either of the entire flow or of a particular cross section, is provided by a 5-W Coherent Innova 70 argon-ion laser. In addition, the secondary vorticity generated at the wall can also be visualized by first pooling a fluorescein dye mixture on the ground plane, as discussed in Harris & Williamson (2012). A similar technique was used by Lim (1989) for his vortex ring studies. This technique is particularly powerful in that it allows selective visualization of either the primary or secondary vortices or both. Images of the flow visualization experiments are acquired by computer-controlled digital single lens reflex (DSLR) cameras at a rate of 1 Hz.

For PIV measurements, the tank was seeded with particles (Potters' Industries Spherical 110P8, mean diameter $10\mu\text{m}$ and density 1.10gcm^{-3}) prior to running the experiment. Illumination of various cross sections was again supplied by a 5-W argon-ion laser which was used with a cylindrical lens to create a 3-mm thick light sheet. Images were acquired by a Kodak MegaPlus 1-megapixel digital camera at a rate of 15 Hz. Pairs of images were then processed by PIVLab

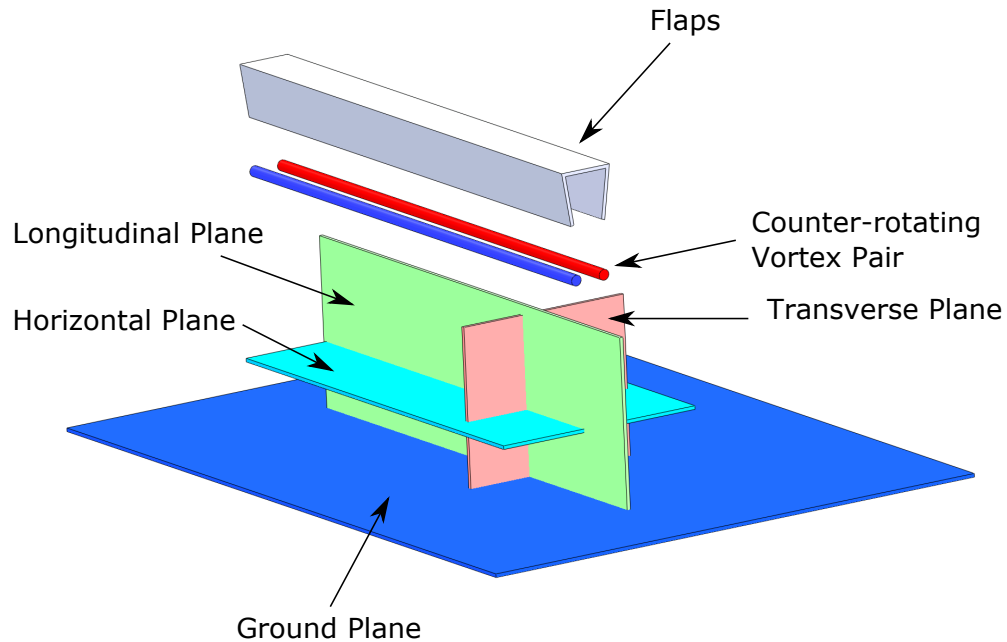


Figure 1.5: Schematic showing the various planes in which light sheets were positioned for PIV experiments.

software (Thielicke & Stamhuis, 2014*a,b*; Thielicke, 2014) in order to compute the velocity fields. A typical velocity field measures 800 by 500 pixels and contains approximately 100 by 60 velocity measurements, spaced approximately 1.5 mm apart. For orientation, figure 1.5 shows the various cross sections used for PIV measurements and flow visualizations in this study. They will be referred to repeatedly in subsequent sections.

Velocity fields obtained from PIV experiments were then further processed to obtain other parameters of interest. Vortex position was measured by tracking the point of maximum vorticity over time. Other parameters, such as the angular orientation of the plane containing the instability and the amplitude of the instability, could then be derived. Circulation was computed by taking the line integral of the velocity field around a contour representing 5% of the maximum measured vorticity.

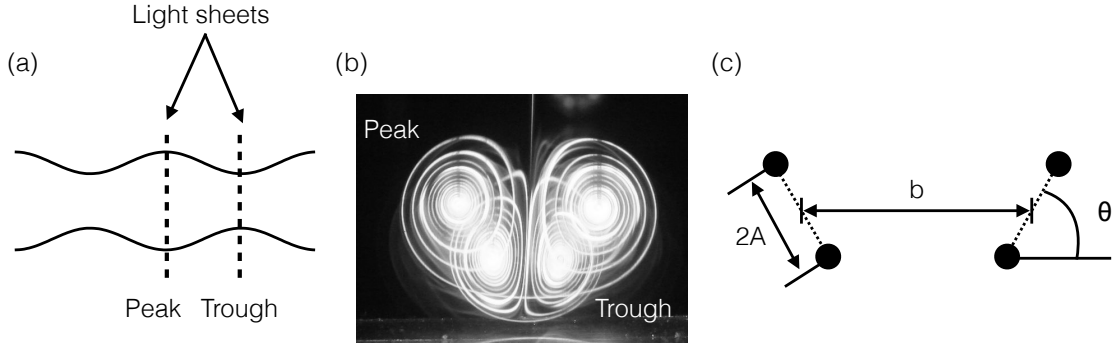


Figure 1.6: Measurement technique used to determine the instability amplitude and the angle of the plane containing the instability. (a) Position of dual light sheets at the peak and trough. (b) An example image acquired using the dual light sheet technique, showing both peak and trough cross sections. (c) Schematic illustrating the relevant geometrical parameters, where A is amplitude, b is vortex separation, and θ is the angle of the plane containing the instability.

As the Crow instability produces a vortex pair with a defined “peak” and “trough” location (figure 1.2), PIV and flow visualization experiments were conducted at both of these cross sections. Figure 1.6(a) shows the position of the light sheet relative to the vortex pair for each of these configurations. In addition, some experiments were conducted with light sheets positioned at the peak and at the trough simultaneously, making use of a beam splitter. These dual light sheet experiments were previously used by Leweke & Williamson (2011) and greatly simplified the task of tracking the relative positions of the two cross sections. In particular, these dual light sheet experiments are especially helpful for determining the amplitude of the instability, as both the peak and trough cross sections are made visible simultaneously. The amplitude can then be computed by simply noting their relative positions in the photographs. Figure 1.6(b) shows an example flow visualization image obtained in this way.

Time for each experiment is measured from the first motion of the flaps and is nondimensionalized by the time required for the vortex pair to descend a

distance equal to one initial vortex spacing. Therefore, the nondimensional time t^* is given by

$$t^* = t \frac{\Gamma_0}{2\pi b_0^2} \quad (1.2)$$

where t is dimensional time, Γ_0 is the initial vortex circulation, and b_0 is the initial vortex spacing.

Other parameters of interest in these experiments include the Reynolds number based on circulation, $Re = \Gamma_0/\nu$, where Γ_0 is the initial circulation and ν is the kinematic viscosity of water. The ratio of initial core size to initial vortex spacing, a_0/b_0 is also relevant. In all experiments presented in this study, $Re \approx 1000$ and $a_0/b_0 \approx 0.4$. The initial height h_0 of the flap edges above the ground plane was the principal variable parameter, and experiments were conducted for values of h_0/b_0 ranging from 3 to 12. In addition, the extent to which the Crow instability has developed was characterized by measuring the amplitude of the instability, A , at a height of b_0 above the wall. Using this parameter, experiments were conducted for A/b_0 between 0.10 and 0.60.

In order to characterize the uncertainty associated with measurements of circulation and other quantities, multiple experiments with the same initial conditions were conducted. The 95% confidence interval for the value of Γ when the vortex pair is not in wall effect ($t^* \approx 3$) is $\pm 2.8\%$. In wall effect, at $t^* \approx 8$, the uncertainty for Γ is $\pm 4.4\%$. Variation in initial vortex spacing b_0 is $\pm 4.4\%$, and variation in vortex core size a_0 is $\pm 3.5\%$. For the amplitude of the instability, the uncertainty out of wall effect ($t^* \approx 3$) is $\pm 6.2\%$ and $\pm 6.6\%$ in wall effect ($t^* \approx 8$).

1.3 Two Base Studies in Vortex Dynamics

Before discussing the effects of wall interaction on the development of a long-wave instability, it is important to appreciate the key features of two fundamental scenarios. First, we study the free development of the Crow instability in the absence of a wall. Second, we examine the interaction of 2D straight vortices with a boundary.

We present a visual overview of the developing Crow instability in figure 1.7, in the manner of Leweke & Williamson (2011). The initially straight vortex tubes are displaced from their original positions. This displacement occurs when the rotation rate of the plane containing a perturbation is zero. This condition is met for perturbations located in a plane oriented at approximately $48^\circ - 50^\circ$ to the horizontal. As shown by Crow (1970), in order to achieve instability, three rotational effects are balanced in this plane: rotation of a vortex due to self-induction, rotation due to the mean strain field of the other vortex, and rotation due to the perturbation strain field of the other vortex. In this “frozen” plane orientation, the strain induced by the other vortex causes the perturbation amplitude to grow exponentially.

As the wavy vortices approach each other at the trough cross section, vorticity cancellation occurs, leading to a decrease in circulation and an increase in pressure at this location. The pressure gradient established by this process drives flow in the axial direction from the troughs to the peaks of the wavy vortex tube, as shown in figure 1.7. (Evidence for this pressure gradient in the case of wall interaction is shown in §1.5.2.) Reconnection occurs between the two vortices at the troughs (Leweke & Williamson, 2011), leaving a periodic series

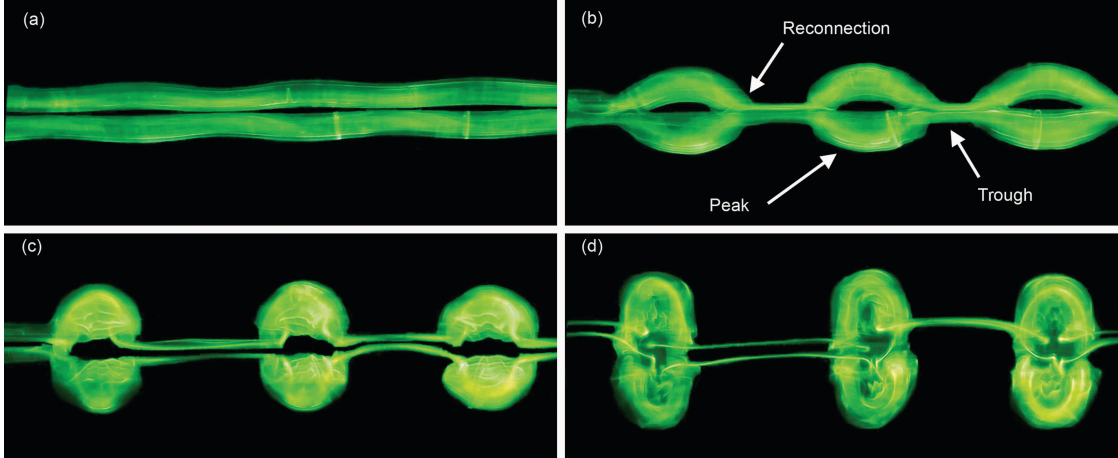


Figure 1.7: Development of the Crow instability, seen in plan view. The vortex pair is moving toward the observer. (a) $t^* = 2.96$ (b) $t^* = 6.52$ (c) $t^* = 7.70$ (d) $t^* = 11.0$

of vortex rings linked by weak bridges, as shown in figure 1.7(c). These bridges of vorticity retain only about 10% of their original circulation.

We show in figure 1.8 the circulation measured at the peak and trough cross sections for the Crow instability using the technique described in §1.2. The circulation at the peak remains relatively constant throughout the evolution of the instability, showing only minor and gradual decay due to diffusion. The circulation at the trough cross section, however, decreases rapidly as the two vortices are forced into close proximity in this region. These data will be contrasted with those measurements for the same experiment conducted with a ground plane installed in §1.5.

As a second basic flow to which comparisons can be made, we consider the case of a two-dimensional counter-rotating vortex pair interacting with a solid boundary. For these experiments, we ensure that the vortex pair remains two-dimensional for reasonable times by using flaps with straight edges. Combined with the low Reynolds number for the flow and a small $h_0/b_0 \approx 4$, the vor-

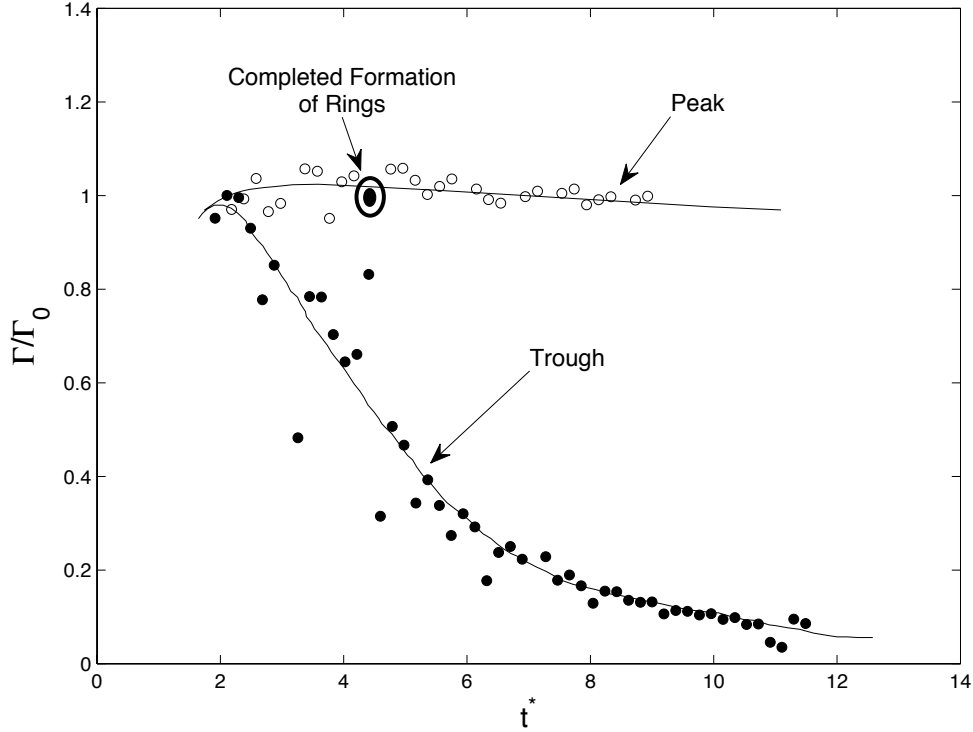


Figure 1.8: Circulation of a vortex pair subject to the unbounded Crow instability, measured at the peak and trough cross sections as a function of time.

tices remain observably free of instabilities prior to reaching the wall. In this flow, the generation of secondary vorticity at the boundary is critically important to the evolution of the pair. According to Lamb (1932), a point vortex pair approaching a free-slip wall should follow a hyperbolic trajectory, as discussed in §1.1. When the no-slip condition is imposed at the wall, however, a boundary layer forms between the primary vortex and the wall and begins to separate, rolling up into secondary vortices of the opposite sign, as shown in figure 1.9(a). Though weaker than the primary vortices, this secondary vorticity is able to modify the motion of the primary vortices significantly. This effect was first explained by Harvey & Perry (1971) and further analyzed by Peace & Riley (1983). The primary vortices rebound from the wall and often follow an

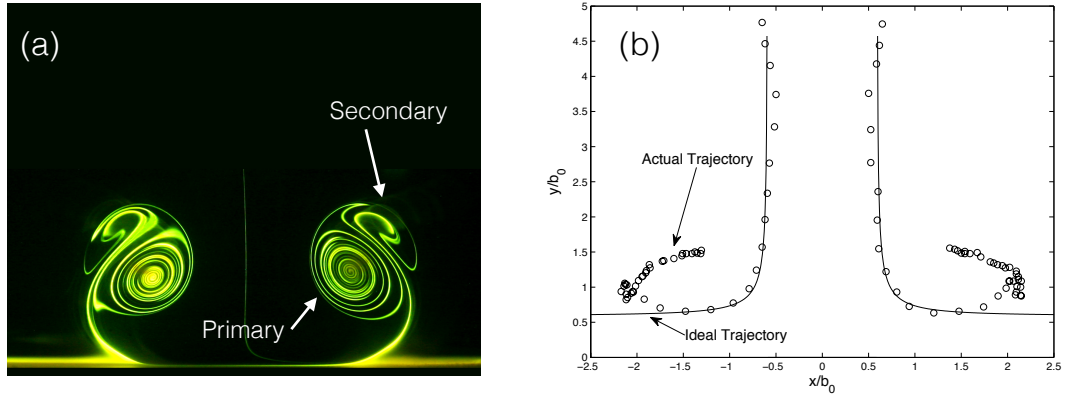


Figure 1.9: (a) Flow visualization from the transverse plane (see figure 5) of two-dimensional (straight) vortices interacting with the wall, showing the development of the secondary vorticity (Harris & Williamson, 2012). (b) Comparison of the measured trajectories of the two primary vortices with the ideal hyperbolic trajectories predicted by Lamb (1932).

epicyclic trajectory. Figure 1.9(b) shows the ideal hyperbolic vortex trajectories (solid lines) and the actual vortex trajectory measured from flow visualization images (symbols). Similar trajectories are shown in Kramer *et al.* (2007).

Measurements of circulation for the two-dimensional vortex-wall interaction are presented in figure 1.10 and compared with numerical simulations for a two-dimensional vortex pair evolving without the presence of the wall (Gupta, 2003). Without the wall interaction, the circulation decays slowly and gradually due to viscous diffusion. However, in the case with a wall present, the primary circulation decays rapidly as the secondary vortices begin to strengthen at $t^* = 4$. Eventually, the circulations of both the primary and secondary vortices become comparable for $t^* > 16$. This dramatic reduction of the primary vortex strength as the primary and secondary vortices are “pushed together” is responsible for many of the changes in vortex topology we observe in cases involving a perturbed vortex in the presence of a wall.

1.4 Modes of Vortex Pair Dynamics Interacting with a Wall

In this section, we discuss the results of three-dimensional experiments in which a counter-rotating vortex pair, subject to a long-wave instability, encounters a solid boundary. It might be expected that a critical height would exist, above which the Crow instability would have sufficient time to cause reconnection of the primary vortices into vortex rings before interaction with the wall boundary. A series of vortex rings would then encounter the boundary. Below this critical height, we might suspect the development of the Crow instability would be inhibited by the wall because the two vortices are pulled apart by the wall interaction. In this case, various final vortex configurations are produced, depending on the extent to which the instability has been allowed to develop before wall interaction. Specifically, we have identified three distinct modes, which may be delineated by the initial height h_0/b_0 above the ground at which the vortices are generated, where h_0 is the initial height and b_0 is the initial vortex spacing. These modes may also be distinguished by the amplitude of the Crow instability measured at a distance b_0 above the wall. This parameter serves as a gauge of the degree of progression of the Crow instability before wall interaction.

1.4.1 Vertical Rings Mode: Secondary-Secondary Vortex Interaction

For h_0/b_0 between 3 and 6, (A/b_0 between 0.1 and 0.3, measured at b_0 above the wall) the vortices evolve as shown in figures 1.11 and 1.12, which present the primary and secondary vorticity, respectively, from both plan and side views.

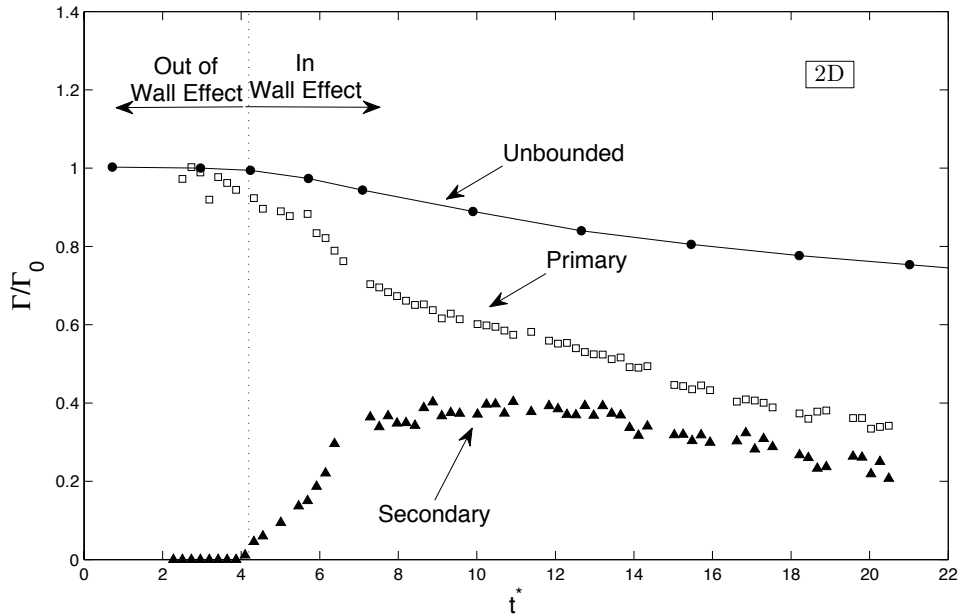


Figure 1.10: Measured circulation of two-dimensional vortices in wall effect as a function of time, compared with a numerical simulation of the circulation for two-dimensional vortices out of ground effect (Gupta, 2003). Also shown is the circulation of the secondary vorticity which develops as the primary pair encounters the wall. Note that the sign of the secondary circulation has been inverted.

At these low initial heights, the Crow instability is inhibited as the vortex pair approaches the wall, and the vortices do not reconnect into rings. Instead, from examination of the primary vorticity, the principal feature is a strong axial flow, driven by a pressure gradient, which transfers fluid from the region of first contact, the trough, to the peak of the vortex tube, as shown in figure 1.11(a)-(h). This “collapsed vortex,” visible in figure 1.11(c), then rebounds away from the wall. “Vortex collapse” is defined as the loss of spanwise uniformity as a result of axial pressure gradients and axial flows, which transport vorticity to concentrated regions along the vortex. The reason for the rebound of the collapsed region is the formation of small vertical vortex rings at the locations of the “collapsed vortices,” as discussed below. The final configuration of the primary

vortices, seen in figure 1.11(d), comprises two regions of concentrated vorticity per instability wavelength and is markedly different from the rings associated with the Crow instability in unbounded fluid.

The mechanism by which this configuration is produced can be discerned through examination of the evolution of the secondary vorticity. The small difference in height between the peak and the trough of the primary vortex means that the trough encounters the wall and generates secondary vorticity there first. The secondary vortex, shown in figure 1.12(a), then rolls up and separates from the wall, forming a “tongue” that wraps around the primary vortex. The secondary vortex tongue (see figure 1.12a) and other parts of the rolled up secondary vortex are transported to the peak, where distinct secondary vortex loops (marked T1 and T2) are formed. (See figures 1.12d and 1.12h.) Simultaneously, the primary vortex circulation at the trough is weakened by viscous vorticity cancellation. This effect creates a region of higher pressure at the trough, as shown later, which drives fluid toward the peak, where the circulation is higher and the pressure is lower.

The tops T1 and T2 of the secondary vortex loops rotate by self-induction into a vertical orientation, as is apparent in figure 1.12(h). The loops from each side of the flow then move toward each other by self-induction and interact along the centerplane of the primary vortex system, as shown in figures 1.12(d) and 1.12(h). They then expand rapidly in a vertical plane, as shown in figure 1.13, in which side views of the primary vorticity (a) and secondary vorticity (b) are shown at a later time in their evolution. The vertical vortex loops are principally composed of the secondary vorticity in (b), although they are more faintly visible in the primary visualization in (a) due to diffusion of the dye into

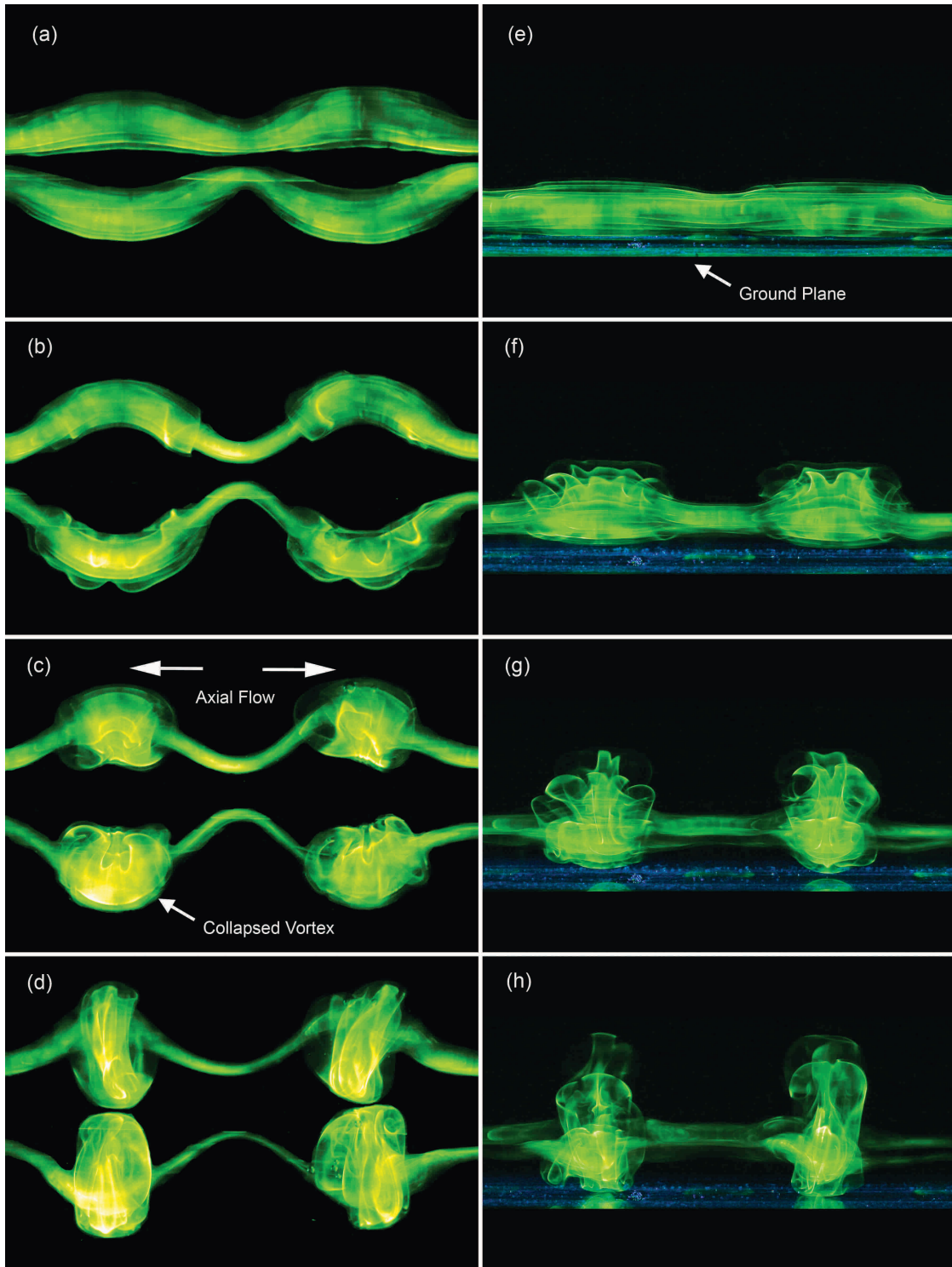


Figure 1.11: Visualization of the primary vorticity associated with the Vertical Rings Mode ($h_0/b_0 = 5$). The left column shows a plan view, in which the vortices are moving toward the observer. The right column shows a side view, with images taken at the same time as those on the left. From top to bottom, the images depict $t^* = 5.68, 7.78, 9.57$ and 12.0 .

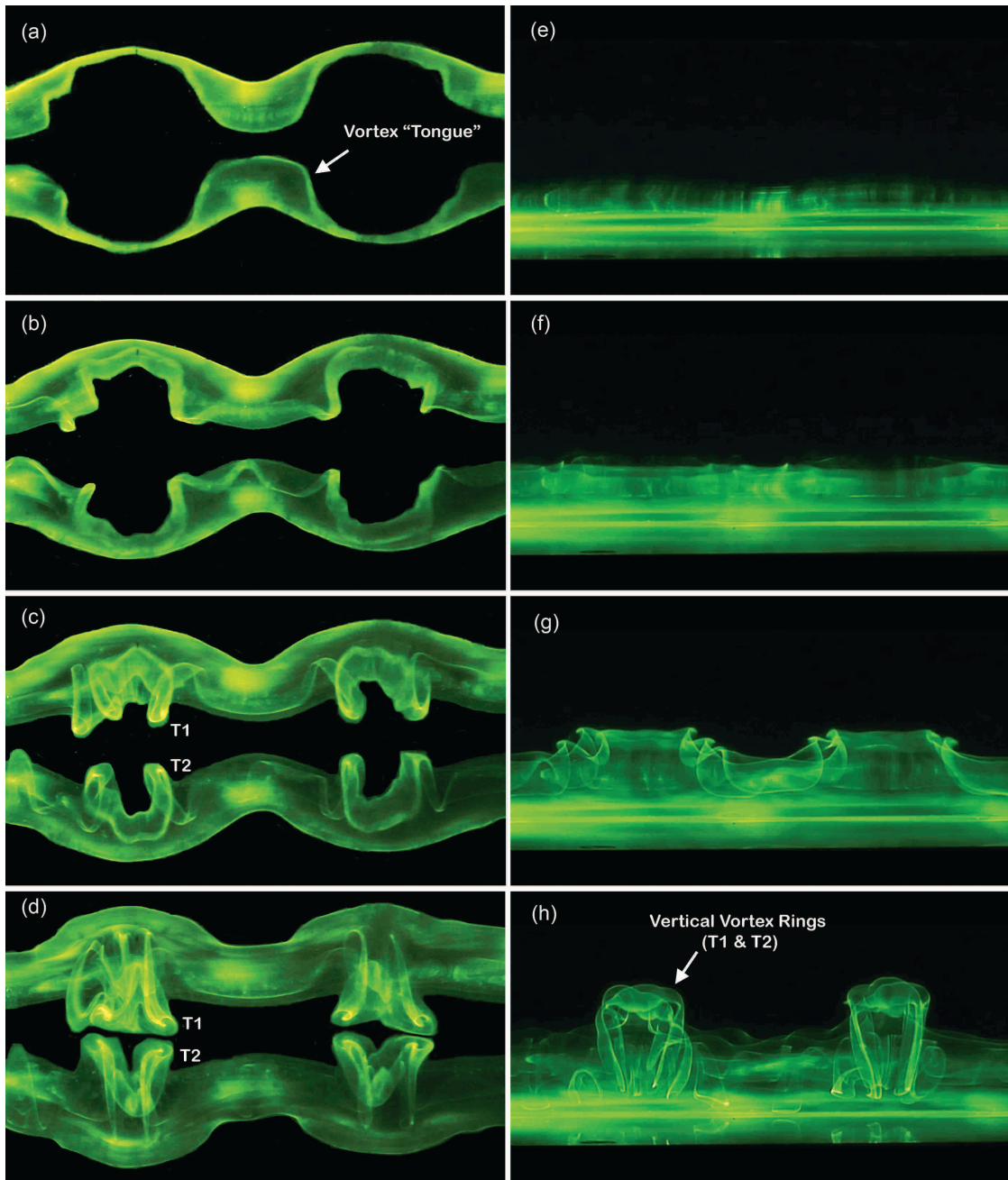


Figure 1.12: Visualization of the secondary vorticity associated with the Vertical Rings Mode ($h_0/b_0 = 5$). As in figure 1.11, the left column shows a plan view and the right column shows a side view. Images were acquired at the same times as those referred to in figure 1.11.

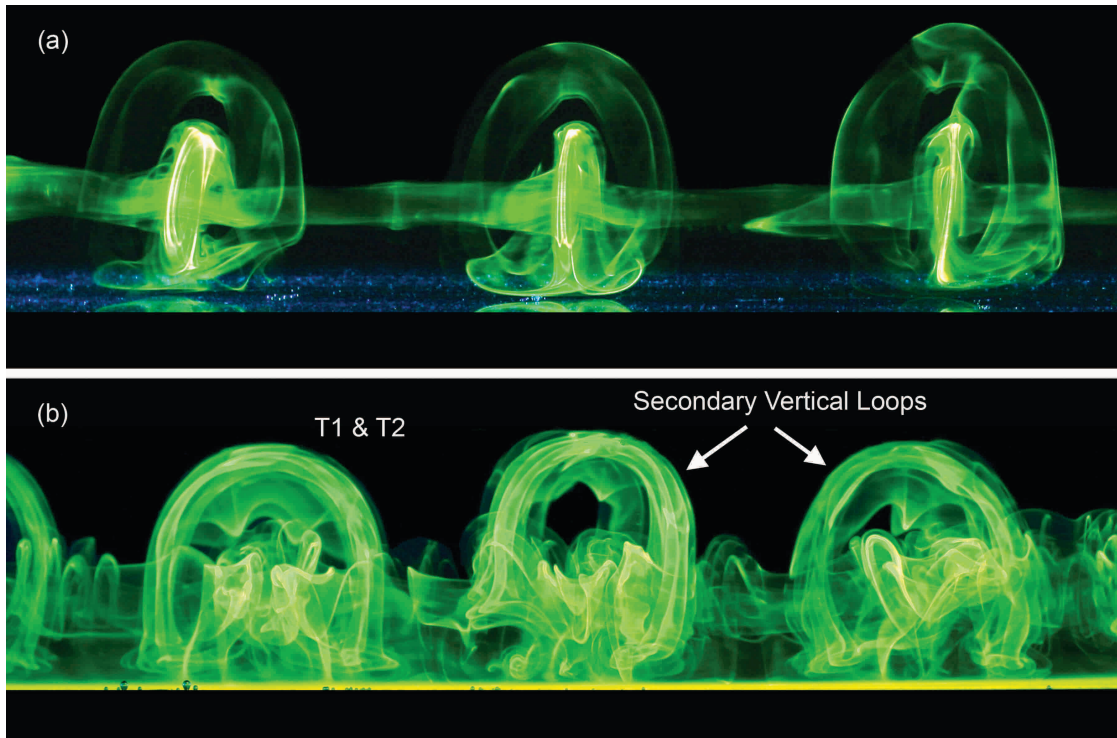


Figure 1.13: (a) Late-time development of the primary vorticity for the Vertical Rings Mode ($h_0/b_0 = 5$), shown from the side. (b) Development of the secondary vorticity for the Vertical Rings Mode, taken at the same time as (a).

the secondary vorticity.

We show in figure 1.14 a schematic depicting our interpretation of the principal vortex dynamics involved in this wall interaction. In (a), the secondary vortex is generated first at the trough location and then becomes wrapped around the primary vortex, forming a “tongue” of vorticity. As the primary vortex is weakened by viscous vorticity cancellation, the pressure at the trough becomes higher, driving fluid toward the peaks of the primary vortex. Measurements of these effects are presented later. The result of this axial flow is the formation of a vortex loop from the secondary vorticity at the peak cross section, as shown in (b). At this stage, the direction of rotation of the secondary vortex loops at T1 and T2 is such that they induce themselves to move upward away from the

wall and then toward the centerline dividing the primary vortices, as depicted in (c). Reconnection of the secondary vorticity at the bottom of the loop to form a ring appears to occur and is visible in the flow visualization of figure 1.13(a). Further evidence suggesting reconnection from PIV measurements is discussed below.

The sequence by which vertical vortex loops (in figures 1.13 and 1.14) rebound from the wall differs from the traditional two-dimensional rebound effect in several important ways. Figure 1.15 shows vorticity contours taken from PIV measurements made using the transverse cross-section plane (see figure 1.5) superposed with streamlines. The left column shows a two-dimensional vortex pair in ground effect, while the right shows a vortex pair subject to the Crow instability in ground effect. In the two-dimensional flow, the secondary vortices orbit the primaries and eventually return to the vicinity of the ground plane between the primary vortices, as shown in figure 1.15(a-d). The flow streamlines advect the secondary vortices down between the primaries. In contrast, when the flow has become three-dimensional by the action of the Crow instability, the secondary vorticity is induced upwards above the primary vortices, with no tendency to get pulled down between the primary vortex pair, as shown in (e)-(h). This is also indicated by the streamlines which, in contrast with the 2D case, are aligned upwards at the locations of the secondary vortices, taking the secondary vorticity away from the wall. The principal vortex interactions are between the secondary vortices. This “secondary-secondary” interaction is indicated by the labeling in figure 1.15(h), which shows a vortex pair in cross section, representing a cut into the top of the vertical vortex loops described earlier. Evidence suggesting that reconnection has occurred at the bottom of the loop to form a ring is visible in figure 1.15(h). There, two patches of vorticity,

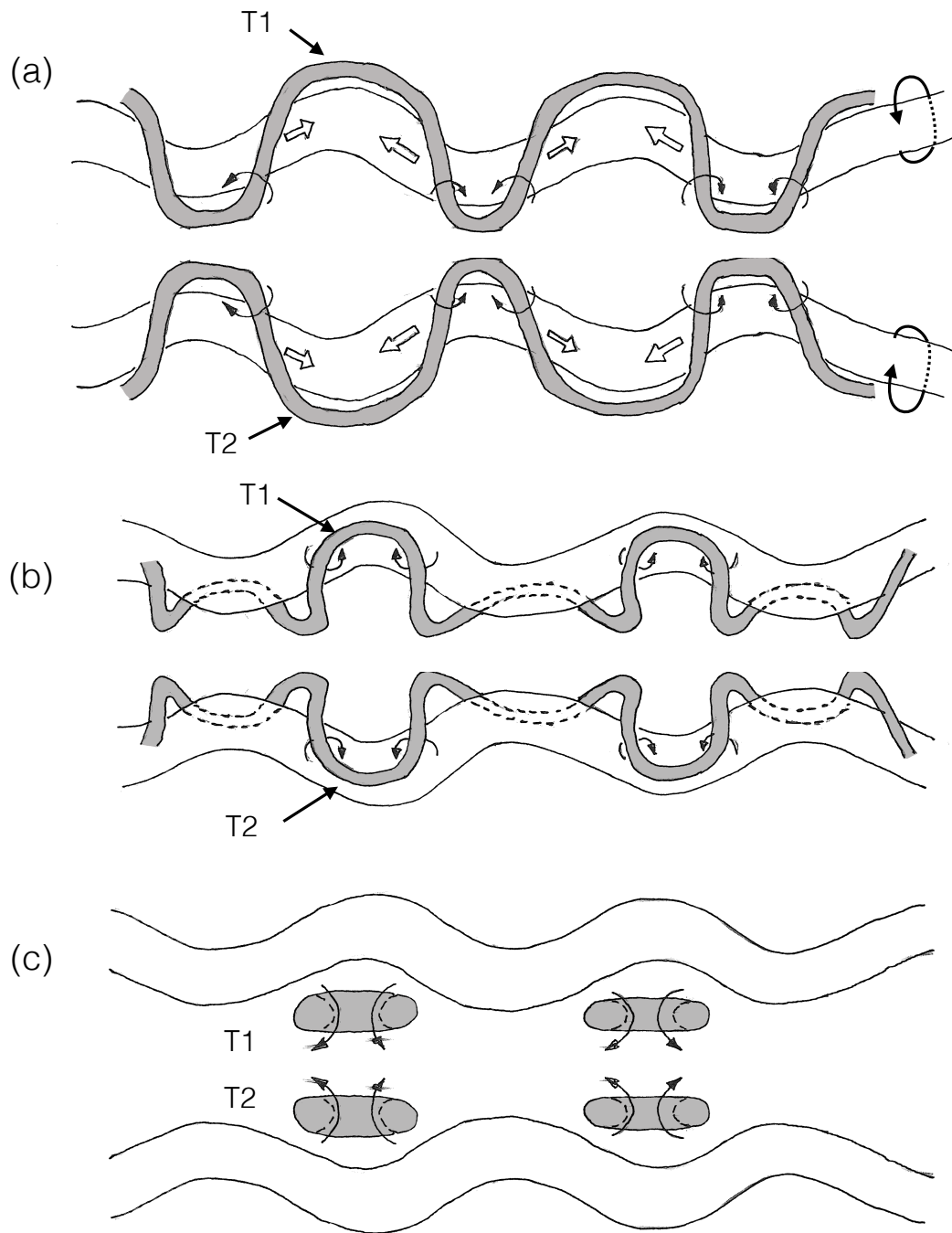


Figure 1.14: Schematic showing the authors' interpretation of the principal vortex dynamics in the Vertical Rings Mode ($h_0/b_0 = 5$).

distinct from the primary vortices, are visible at the bottom of the PIV image. We suggest that these patches represent the bottom of each vortex ring.

In order to confirm the presence of a vortex loop, additional experiments were conducted using a light sheet positioned in the horizontal plane (see figure 1.5). Figure 1.16 shows vorticity contours derived from PIV and flow visualization from the same cross section. Two “vortex pairs,” representing the vertical arms of the vortex loops, are visible in this view. Furthermore, the circulation of the vortex pair measured in this plane is comparable to that measured for the secondary vortices in the transverse plane (approximately 20% of the initial circulation of the primary vortex). As the cross sections depicted in figure 1.15 and figure 1.16 are orthogonal and both depict vortex pairs, we have reasonable evidence that a vertical vortex ring has formed.

1.4.2 Horizontal Rings Mode: Secondary-Primary Vortex Interaction

For values of h_0/b_0 between 6 and 9 (A/b_0 between 0.3 and 0.5, measured at b_0 above the wall), the behavior of the vortex pair is distinctly different. Figure 1.17 shows the evolution of the primary vorticity in plan view. Immediately apparent here is the stronger axial flow from the trough to the peak. The trough cross sections become almost entirely evacuated of dye and later measurements of circulation show that they are weakened much more than for vortex pairs generated at lower values of h_0/b_0 in §1.4.1 The weakening of the trough cross section is caused by two effects. First, the Crow instability has developed further and has consequently moved the vortices closer together at the trough, leading

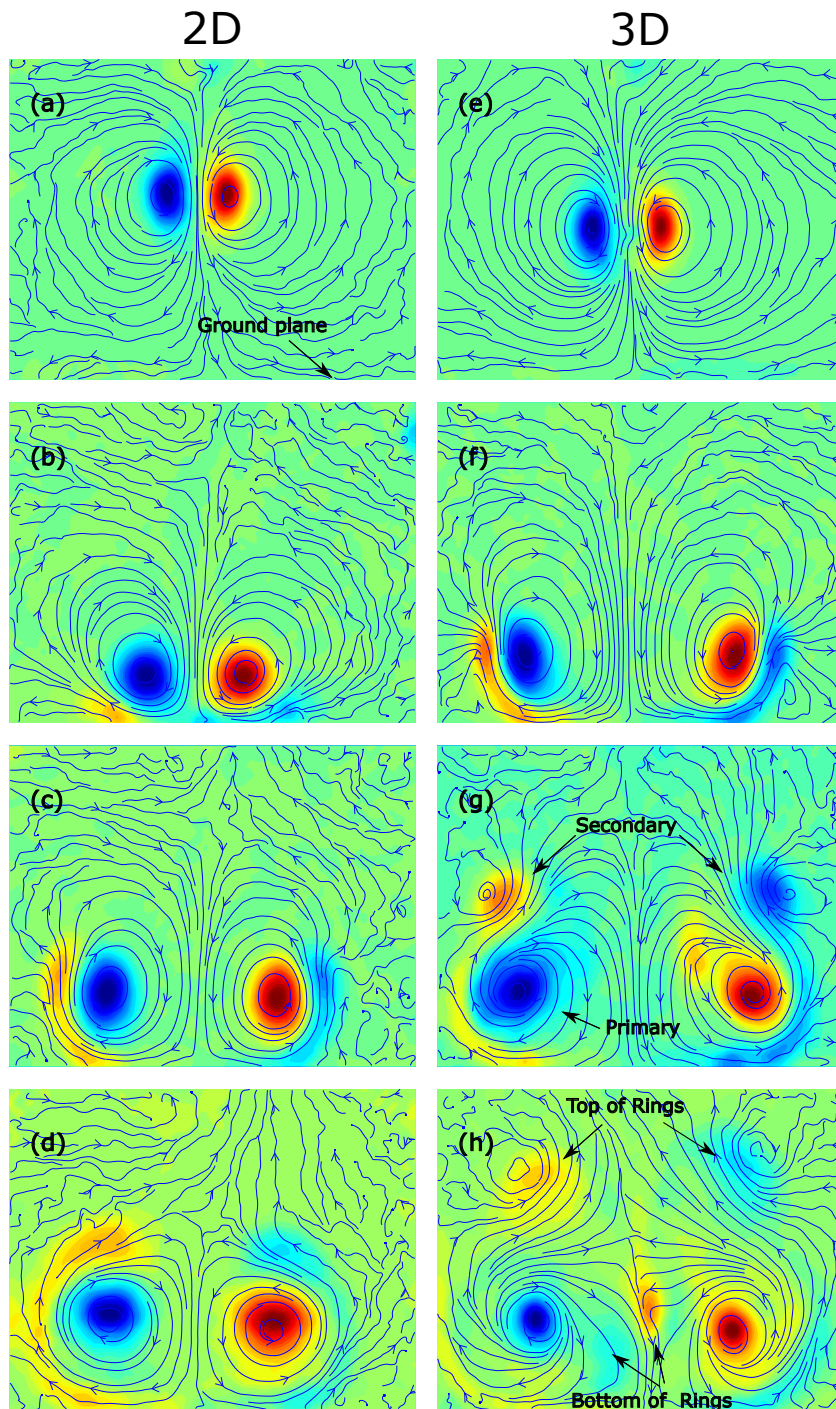


Figure 1.15: Contours of vorticity and streamlines for a two-dimensional vortex pair interacting with a wall (left column) and a vortex pair subject to the Crow instability interacting with a wall in the Vertical Rings Mode (right column). From top to bottom, the images depict the vorticity at times $t^* = 2.74, 5.93, 8.31,$ and 11.1 .

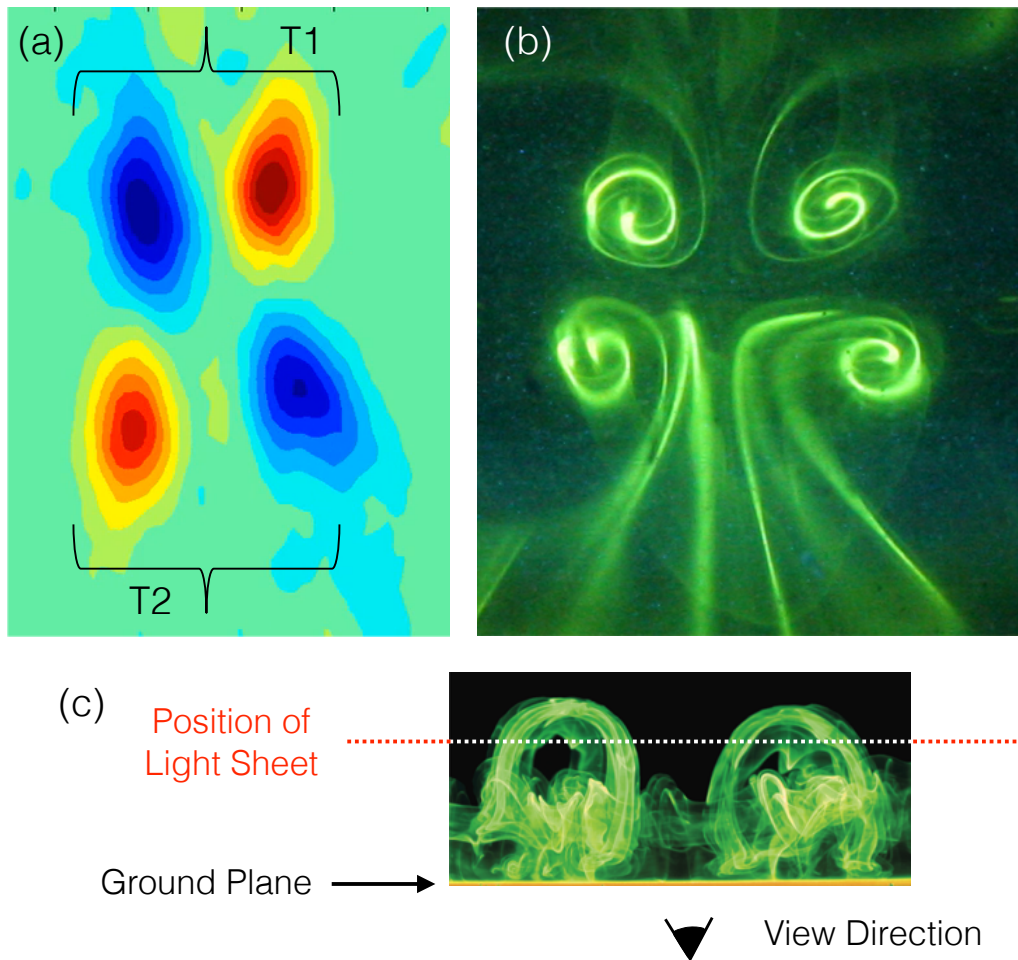


Figure 1.16: Contours of vorticity (a) and corresponding flow visualization (b) image taken in the horizontal plane (see figure 1.5), cutting through the legs of the vertical vortex loops. The position of the light sheet is shown in (c).

to more vorticity cancellation between the two primary vortices. This effect is visible in figures 1.17(b) and 1.17(c). Second, the primary vortices are further eroded by interaction with the secondary vorticity that is generated at the wall. The reduced circulation in the trough produces a higher pressure which drives the stronger axial flow from trough to peak. The Crow instability remains inhibited, and the wall interaction produces two “collapsed vortex” structures per instability wavelength instead of forming a single vortex ring. These structures

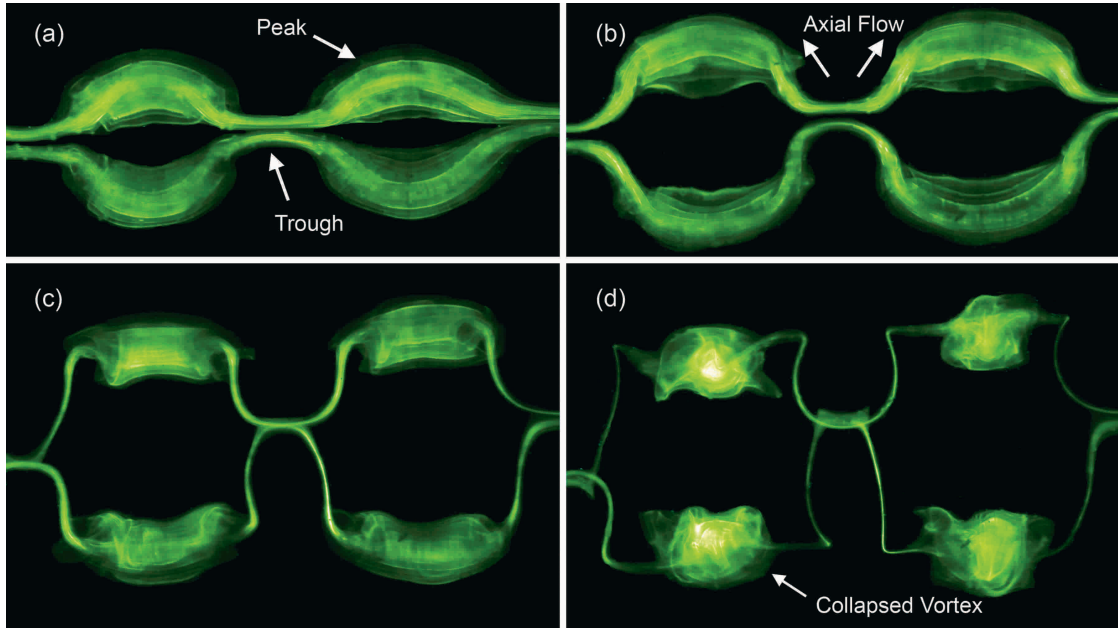


Figure 1.17: Visualization of the primary vorticity associated with the Horizontal Rings Mode ($h_0/b_0 = 7.5$) in plan view. (a) $t^* = 8.39$. (b) $t^* = 10.1$. (c) $t^* = 12.7$. (d) $t^* = 15.6$.

are labeled in (d).

Each of the “collapsed vortices” contains a horizontally-oriented vortex ring which then rebounds vertically upwards from the wall, although this is not clearly evident from the visualization alone. Figure 1.18 shows vorticity contours computed from PIV measurements taken in the transverse plane and in the longitudinal plane (see figure 1.5). During the time that the secondary vorticity is generated at the wall, the primary vortex topology is altered by the axial flow moving toward the peak, and the structure begins to resemble a hollow vortex (see figure 1.18b), in which the principal vorticity is situated around the perimeter of the vortex, similar to the hollow vortex described by Baker *et al.* (1976) and in Saffman (1992). It seems that the vortex is entraining some irrotational fluid during the course of its evolution, likely as a result of the axial flow. The upper portion of the hollow vortex, labeled P1 in figure 1.18(c),

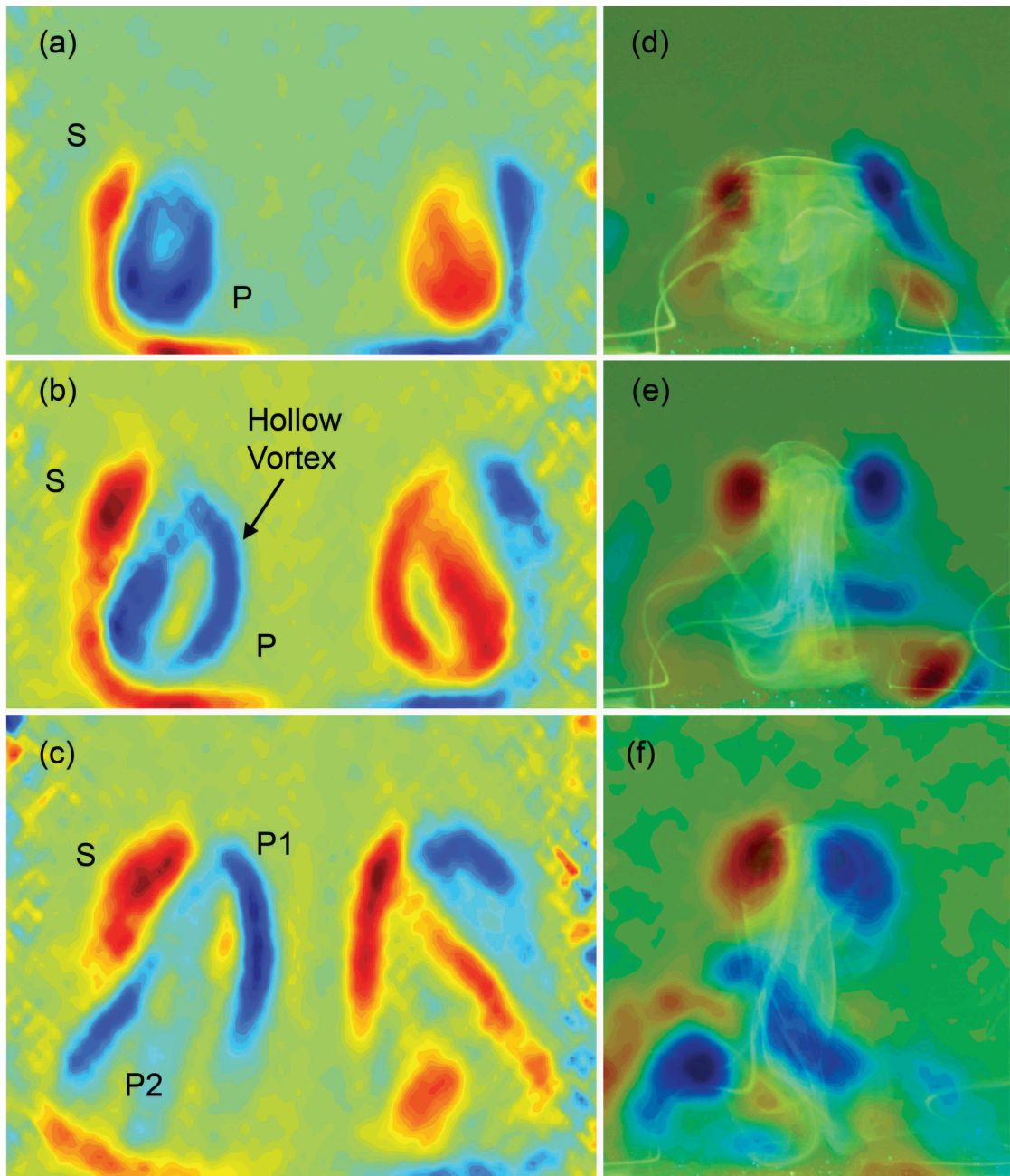


Figure 1.18: Contours of vorticity associated with the Horizontal Rings Mode ($h_0/b_0 = 7.5$). The left column shows contours acquired using the transverse plane, and the right column shows the longitudinal plane at the same time. Superimposed on the vorticity contours in (d)-(f) are flow visualization images acquired at the same nondimensional time. From top to bottom, the images depict times $t^* = 12.1$, 14.4 , and 20.2 .

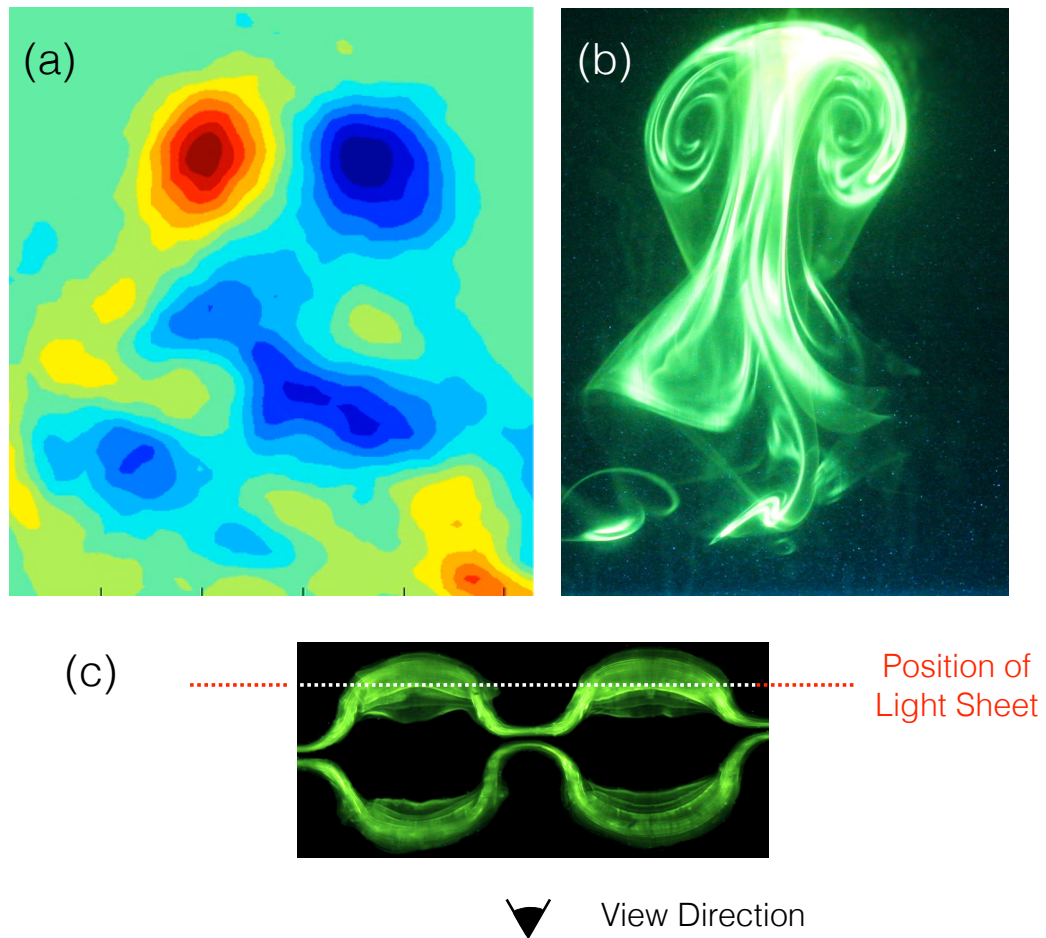


Figure 1.19: Contours of vorticity (a) and corresponding flow visualization image (b) taken in the longitudinal plane (see figure 1.5), showing the rebounding horizontal vortex ring of the Horizontal Rings Mode ($h_0/b_0 = 7.5$). The position of the light sheet is shown in (c).

interacts with and reconnects with the secondary vortex to form a vortex ring. The right column of figure 1.18 shows the flow observed from the longitudinal plane (see figure 1.5). Here, vorticity contours and flow visualization images are overlaid and show the development of a vortex pair that rebounds rapidly from the wall. As this view is orthogonal to the transverse plane of (a)-(c), and both views contain “vortex pairs” in the same location, we can confirm that a vortex ring has formed, although the actual process of reconnection is difficult

to observe directly. Furthermore, the circulations of the “vortex pairs” observed in each plane are comparable, approximately 25% of the initial circulation of the primary vortex. In figure 1.19, we compare the vorticity contours acquired in the longitudinal plane with a flow visualization image acquired using the same cross-sectional light sheet. The sense of rotation of the ring is clearly marked by the dye.

In figure 1.20 we present a schematic illustrating the principal vortex dynamics involved in the evolution of the Horizontal Rings Mode. The secondary vortex is represented by the shaded regions shown in (a). During the evolution of the instability, the secondary vortex is deformed by the stronger primary in (b) and advected toward the peak cross section by the axial flow described earlier. According to our PIV vorticity measurements, it seems that reconnection occurs between the secondary vortex and the primary vortex, leaving two horizontal vortex rings for each instability wavelength, as depicted in (c). These horizontal rings then propel themselves vertically away from the wall by self-induction (towards the observer in figure 1.20).

Reconnection is a critical process in the evolution of the vortex rings described above. This process has been extensively studied as it is a fundamental process by which vortical structures interact and change topology. It is well known as a key to the classical problem of the Crow instability without ground effect and to the evolution of vortex rings. The present flows are complex and would benefit from numerical simulations to interpret the vortex dynamics and topological changes in the vorticity distribution.

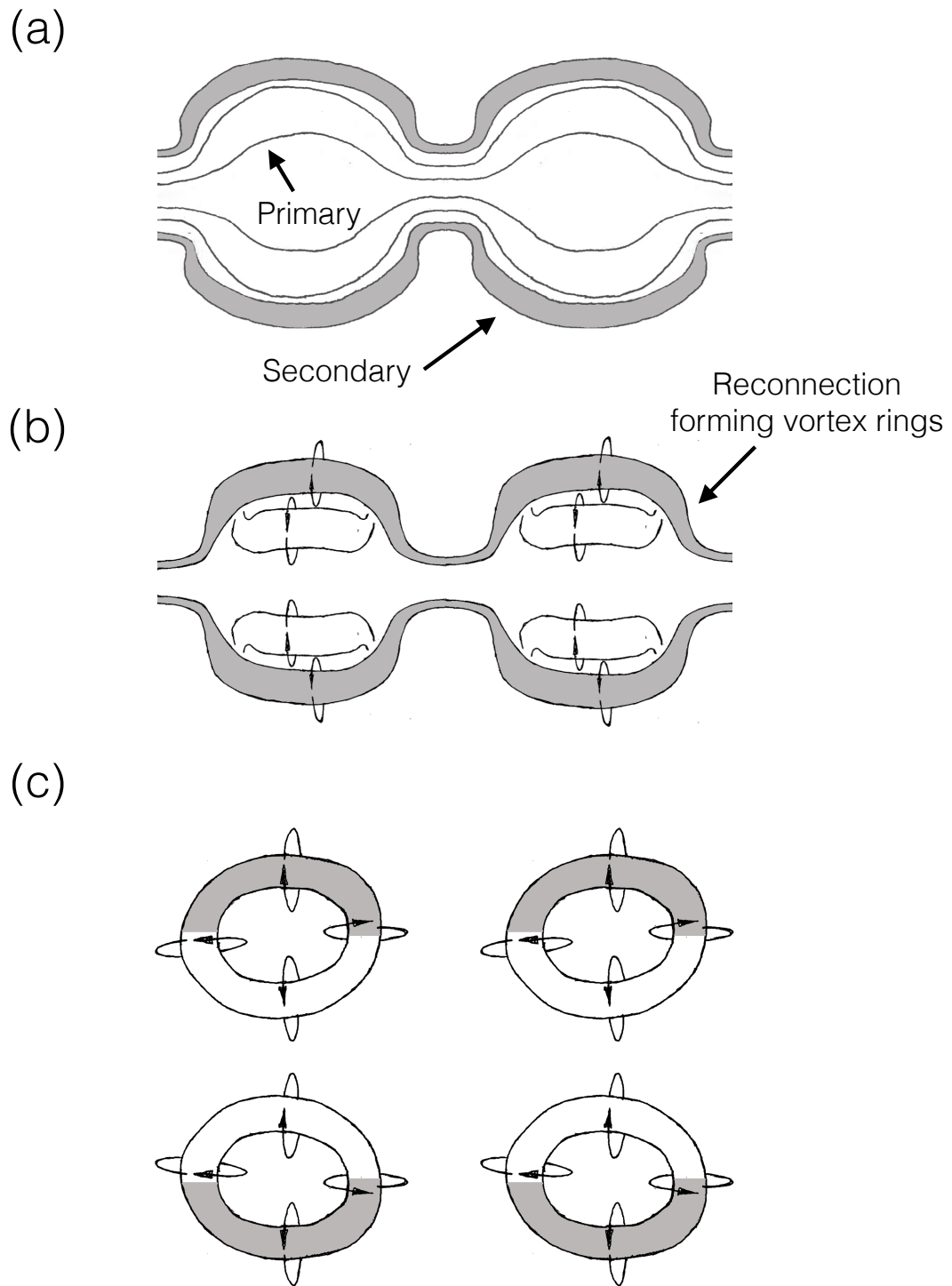


Figure 1.20: Schematic showing the authors' interpretation of the principal vortex dynamics leading to the development of horizontal vortex rings in the Horizontal Rings Mode ($h_0/b_0 = 7.5$).

1.4.3 Large Rings Mode: Vortex Ring-Surface Interaction

As we shift to larger values of h_0/b_0 greater than 9 (A/b_0 greater than 0.5, measured at b_0 above the wall), the long-wave instability develops to the point of reconnection and the formation of vortex rings prior to the vortices' reaching the ground plane. Figure 1.21 shows the result of wall interaction for vortex rings formed in this manner. The final configuration of vorticity in this case is significantly different from both previously considered cases, with the rings rapidly expanding upon experiencing the effects of the wall. The primary ring can then generate secondary and tertiary vorticity at the wall. This effect has been observed in many other studies, and may itself result in the generation of other instabilities, such as those observed in the work of Swearingen *et al.* (1995) and Walker *et al.* (1987). Interestingly, this is not the only possible final vortex configuration for the ring-wall interaction. Because the Crow instability develops in a plane that is inclined to the horizontal, it produces rings which are nonplanar. Furthermore, as described by Leweke & Williamson (2011), the rings can change their orientation due to the effects of self-induction. Consequently, depending on the precise moment at which the rings encounter the wall, other phenomena, including the axial flow and vortex collapse described for the Vertical and Horizontal Rings Modes, can be triggered in addition to the behavior shown in figure 1.21.

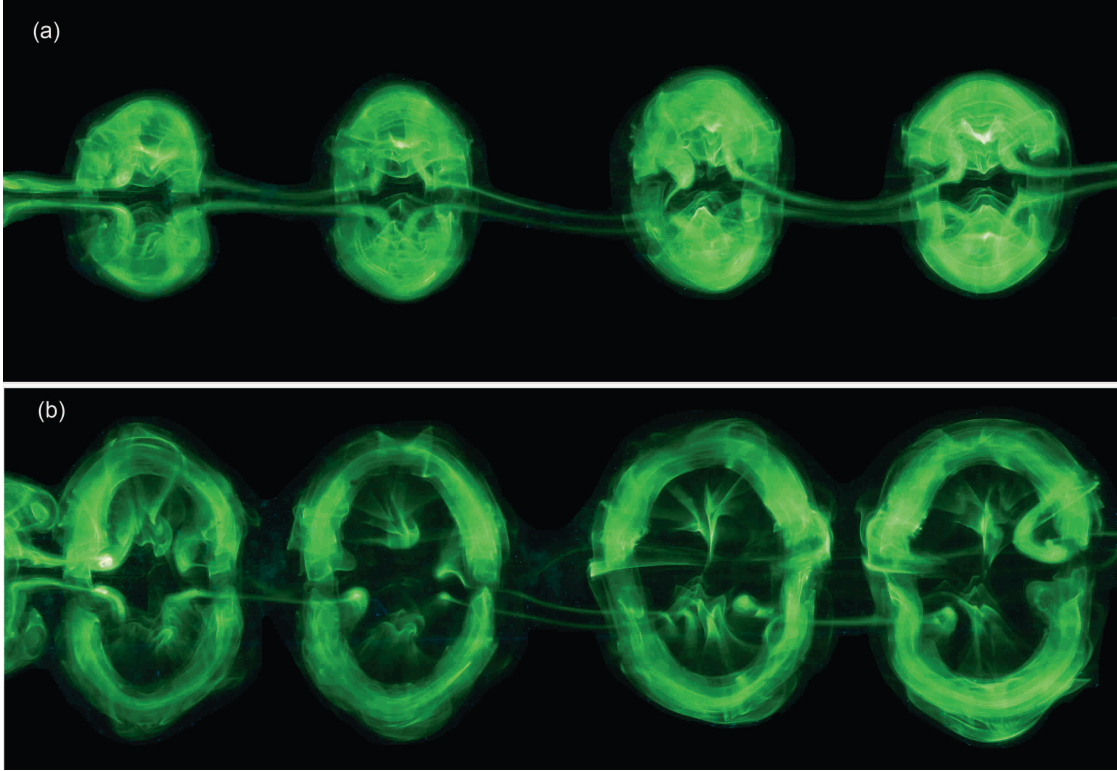


Figure 1.21: Interaction of vortex rings formed by the Crow instability with a wall in the Large Rings Mode ($h_0/b_0 = 10$). (a) $t^* = 8.00$ (b) $t^* = 10.7$

1.5 Discussion

1.5.1 Vortex Dynamics

In this section we discuss how wall interaction alters other quantities describing the evolution of the vortex pair, such as the circulation of the vortices as a function of time, the amplitude of the instability, the angle of the plane containing the instability, and the vortex pair trajectories. Figure 1.22 shows the instability amplitude as a function of time for the Vertical Rings Mode and the Large Rings Mode and the unbounded Crow instability. The amplitude was determined from dual light sheet visualization experiments conducted in the

transverse plane (see figure 1.5), as described in §1.2. Figure 1.22 presents the actual amplitude of the instability in the plane in which the instability exists.

The long-wave instability proceeds through several phases of development as the amplitude grows and the vortices reconnect to form vortex rings. The amplitude for the Large Rings Mode tracks that for the unbounded long-wave instability very closely until the wall effect is observed around $t^* = 11$. After that point, the rings stop their downward motion and the amplitude reaches a plateau. In the unbounded case, the rings continue downward, leaving the trough regions behind and causing the amplitude to continue to grow. For the Vertical Rings Mode, the Crow instability is inhibited long before it is able to form vortex rings. Consequently, the amplitude diverges from the other two cases early in its evolution, around $t^* = 5$ in our example. Interestingly, following wall interaction, the amplitude of the instability actually decreases due to rotation of the plane containing the instability, as explained below.

One characteristic of this flow becomes significantly modified when the ground plane is present: namely the orientation of the instability plane angle as a function of time. (The instability plane angle is the angle of the plane that contains the instability waviness, and it can be measured using the dual-light sheet technique discussed earlier with figure 1.6). Initially, with or without a wall, the instability angle is around 48° - 50° . Sketches of the peak locations (solid symbols) and trough locations (open symbols) are shown in figure 1.23 for different times A, B, C, D, where we also show a plot of the variation of instability angle. There is a significant difference when there is a ground plane present when compared with the variation of the angle for the unbounded Crow instability in Leweke & Williamson (2011). After the initial phase close to A, the instability

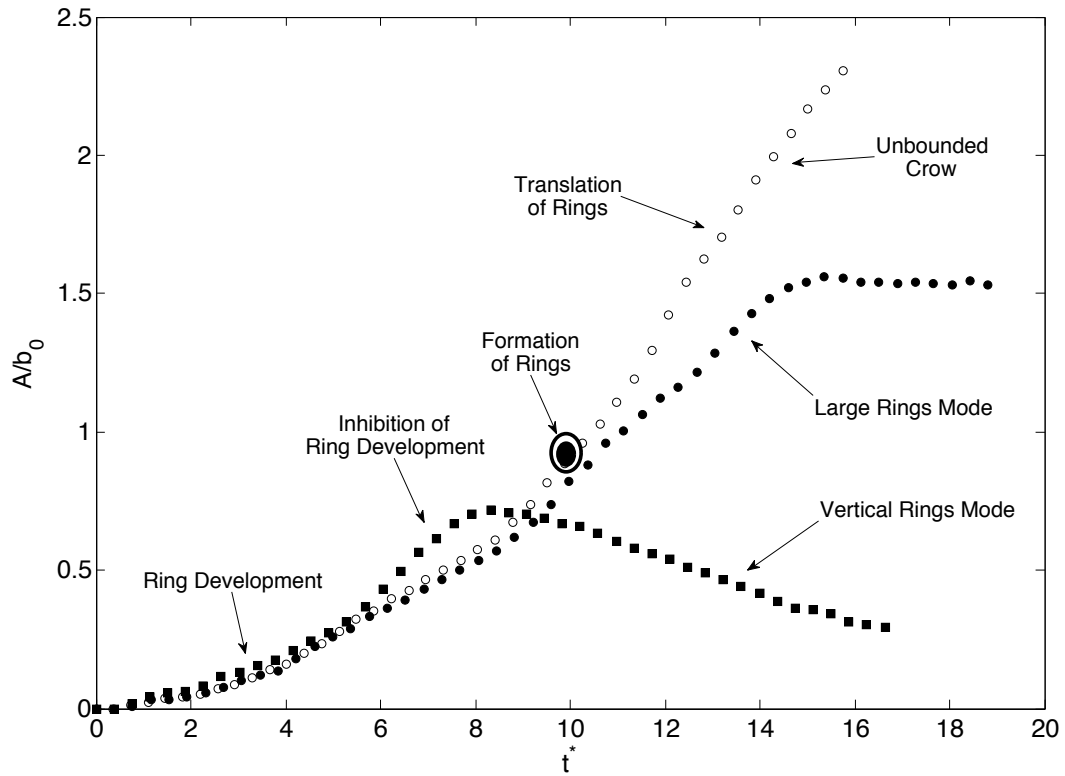


Figure 1.22: Amplitude of the unbounded Crow instability, the Vertical Rings Mode, and the Large Rings Mode as functions of time. The amplitude presented here is measured in the plane of the instability and includes both its horizontal and vertical components.

plane angle decreases to point B, due to the rebound effect of secondary vorticity acting on the trough primary vorticity earlier than the peak primary vorticity. Thereafter the plane angle increases as the ground effect pulls the troughs away from each other along the wall, and at C the plane angle is close to 90° (vertical). The angle further increases to point D. In essence, if one looks at the instability in plan view (vertically downwards in the diagrams of figure 1.23), for cases C and D, there is what could be called a “reverse waviness.” The trough is the location at which vortices initially make their closest approach in the long-wave instability; the effect of the ground causes the peaks to be the parts of the vortices that come closest together. In this sense the waviness is reversed.

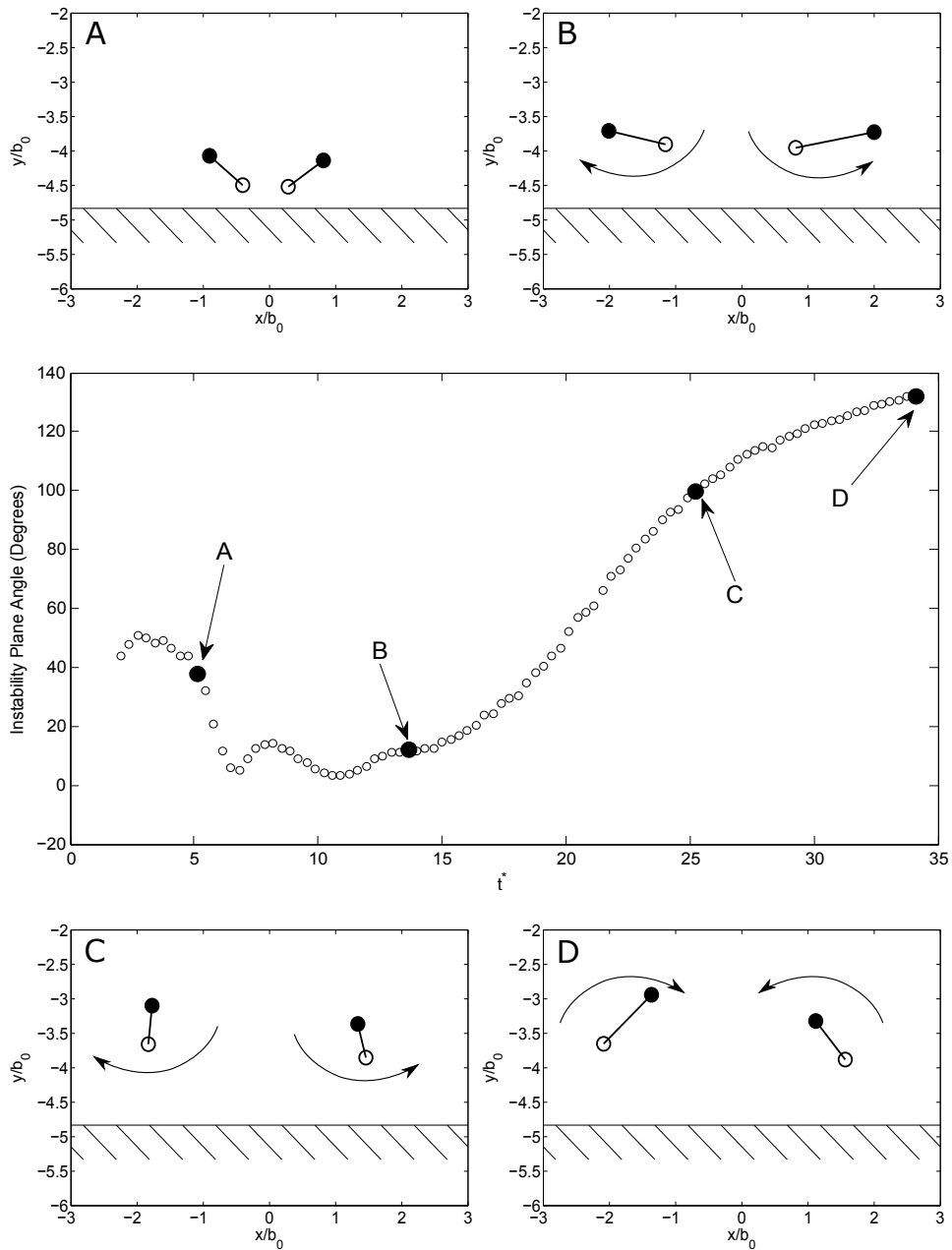


Figure 1.23: The angle of the plane containing the instability as a function of time for the Vertical Rings Mode ($h_0/b_0 = 5$). Schematics depicting the relative positions of the peak and trough at the labeled points are also shown, in which the peak is represented by a filled circle and the trough by an open circle.

The circulation of the primary vortices experiences distinct changes upon wall interaction. Figure 1.24(a) shows the circulation measured at the peak and trough cross sections for a vortex pair evolving according to the Vertical Rings Mode. Here, the trough cross section enters wall effect before the peak cross section because the developing Crow instability has moved the troughs below the peaks, as shown in figure 1.23(A). Because of this difference, the circulation of the trough decreases sooner and more rapidly than that of the peak cross section. This spanwise difference in circulation creates a pressure gradient and drives axial flow along the vortex.

Figure 1.24(b) presents the circulation measured at the peak location for the unbounded Crow instability as well as circulation at the peak location for the Large Rings Mode, with $h_0/b_0 = 10$. In this mode, the Crow instability has sufficient time to cause vortex reconnection and the formation of vortex rings. The secondary vorticity near the wall weakens the primary vortices significantly. This is similar to the 2D vortex decay described in §1.3. The trough circulation behavior (not included in figure 1.24) is the same for both flows and also experiences a rapid decrease in vortex strength. In the case of the peak of the vortex, the circulation decay is due to a primary-secondary interaction at the wall. For the trough, the circulation decays as a result of primary-primary interaction as the Crow instability forces the vortices together during their descent.

1.5.2 Axial Flow

Fundamental to all of the possible modes observed in this work is the presence of significant axial flow along the vortex tubes. This flow moves fluid away

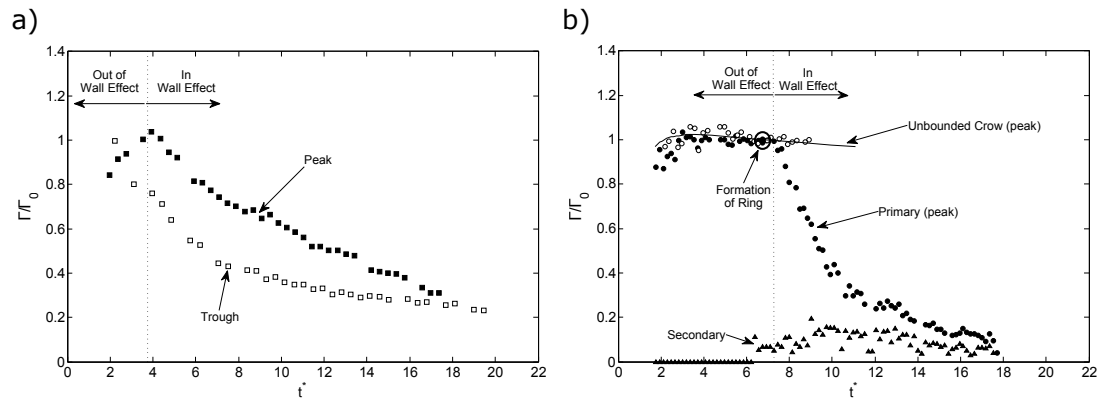


Figure 1.24: (a) Circulation measured at the peak and trough cross sections for a vortex pair subject to the Crow instability, evolving in wall effect in accordance with the Vertical Rings Mode ($h_0/b_0 = 5$). (b) Circulation of a vortex pair subject to the Crow instability at the peak cross section, both with and without the presence of a wall. Also shown is the development of the secondary vorticity at the wall. Note that the sign of the secondary vorticity has been inverted.

from the trough, the part of the vortex that contacts the wall first, and causes the vortex to “collapse” toward the peak region.

Axial flow has been studied in the context of vortex bursting by Moet *et al.* (2005). In their computations, a Gaussian vortex with a variable core radius was used to generate a pressure gradient along the length of the vortex. The region of larger cross section had a correspondingly higher pressure than the part of the vortex with smaller cross section. The consequent pressure gradient then pushed fluid from the larger diameter section toward the smaller cross section.

In our experiment, the pressure gradient is generated not by a change in cross-sectional area along the vortex, but by the weakening of the circulation at specific spanwise locations. In our case, the thinning of the vortex core radius in the trough is associated with an increase in pressure, opposite to the flow illustrated in Moet *et al.* (2005). This effect occurs at the trough cross section first because that is the part of the vortex which encounters the wall first. Viscous

vorticity cancellation caused by interaction with the secondary vorticity at the wall causes the primary circulation to decay, increasing the pressure locally.

In order to quantify the magnitude of the pressure gradient generating the axial flow, we have modeled the vortices as Gaussian. From the Navier-Stokes equations written in cylindrical coordinates, the pressure field in a Lamb-Oseen vortex can be defined by

$$\rho \frac{v_\phi}{r^2} = \frac{\partial p}{\partial r} \quad (1.3)$$

where ρ is the fluid density, v_ϕ is the azimuthal velocity, r is the radial coordinate, and p is the pressure. The azimuthal velocity is given by equation (1.4) below and is a function of circulation Γ and vortex core size a .

$$v_\phi(r) = \frac{\Gamma}{2\pi r} \left[1 - \exp\left(-\frac{r^2}{a^2}\right) \right] \quad (1.4)$$

Using measured values of the circulation and vortex core size in equation (1.4) and integrating equation (1.3), figure 1.25(a) shows the computed pressure in both the peak and the trough as a function of time for the Horizontal Rings Mode. As the troughs are weakened both by primary-primary interaction and then in wall effect by primary-secondary cancellation, the pressure in the trough becomes larger than the pressure at the peak. Consequently, there is a pressure gradient established between the trough and the peak, which drives a relatively strong axial flow, ultimately leading to vortex collapse at the peak. The same weakening of circulation occurs at the peak, but it is delayed compared to the trough, allowing the establishment of the pressure gradient.

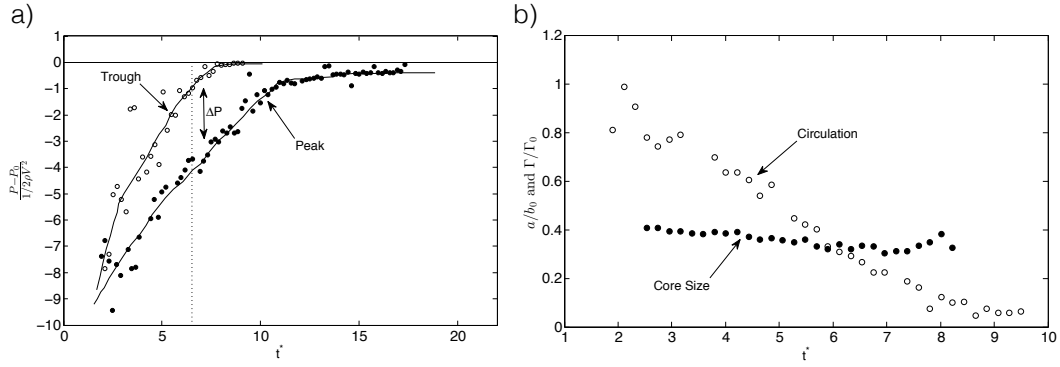


Figure 1.25: (a) Pressure computed at the vortex center for the peak and trough cross sections as a function of time in the Horizontal Rings Mode. P_0 is the pressure far from the vortex center. V is the initial self-induced descent velocity of the vortex pair. (b) Circulation and vortex core size for the trough cross section of the Horizontal Rings Mode ($h_0/b_0 = 7.5$).

From flow visualization images (see figure 1.17), the axial flow driven by this pressure gradient appears to be largely complete between $t^* = 12$ and $t^* = 15$. This estimate correlates well with the computed pressure curves, which show the pressure gradient becoming very small for times greater than $t^* = 15$.

To gain further insight into the parameters that govern the evolution of the pressure, we can consider the pressure coefficient of a Rankine vortex. The pressure at the center of a Rankine vortex is well-known and is given by equation (1.5).

$$p - p_0 = -2 \frac{\rho \Gamma}{8 \pi a^2} \quad (1.5)$$

where p is the pressure, p_0 is the pressure far from the vortex, Γ is circulation, and a is core size.

We define the pressure coefficient in the usual manner:

$$C_p = \frac{p - p_0}{\frac{1}{2}\rho V^2} \quad (1.6)$$

where V is the initial descent velocity of the vortex pair, $\Gamma_0/2\pi b_0$, and Γ_0 and b_0 are the initial vortex circulation and separation, respectively.

Substituting equation (1.5) and the initial descent velocity into equation 1.6, we obtain

$$C_p = -2 \left(\frac{b_0}{\Gamma_0} \right)^2 \left(\frac{\Gamma}{a} \right)^2 \quad (1.7)$$

Equation (1.7) shows that the pressure coefficient is simply a function of the ratio of circulation Γ to core size a . Figure 1.25(b) shows that the increase in pressure at the trough is due largely to the rapid weakening of the circulation at that location. The core size remains relatively constant during the wall interaction, whereas the circulation decreases markedly.

1.6 Discussion of Other Relevant Studies of Vortex-Wall Interactions

The present study is related to an entire class of flows in which a perturbed vortex approaches a parallel boundary. The general problem, in which viscous vorticity cancellation causes a pressure gradient and axial flow, is not solely tied to the existence of a vortex pair or the long-wave instability influenced by a wall. Similar phenomena occur for a single vortex close to a wall, and the perturbations need not be periodic. A single perturbation at some spanwise location

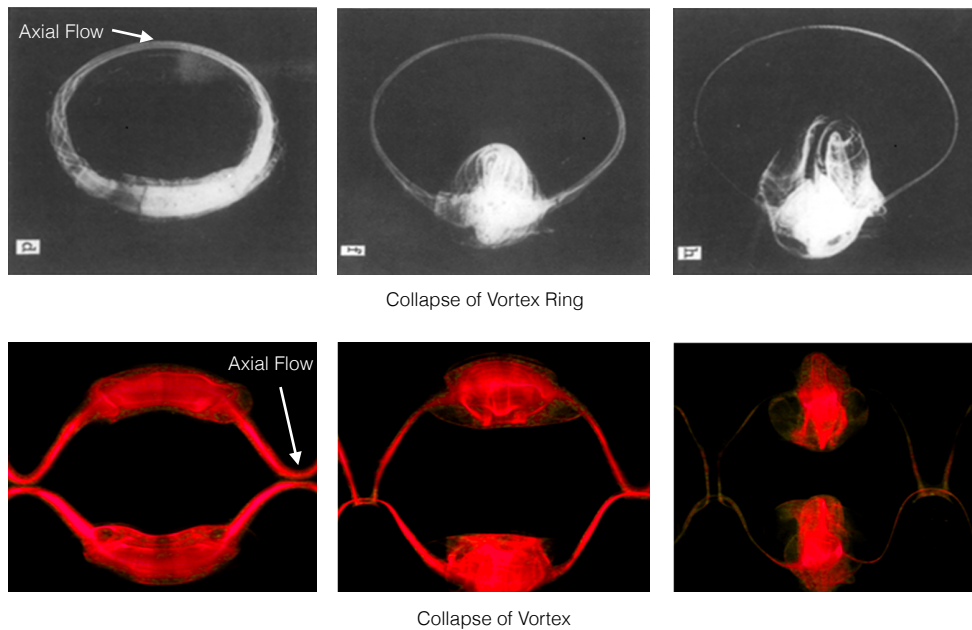


Figure 1.26: Comparison of the evolution of the primary vorticity of a vortex pair in wall effect and the collision of a vortex ring with an inclined wall from (Lim, 1989) (reprinted by permission from Springer). The vortex ring interaction is shown in the top row, and a plan view of the vortex pair is shown in the bottom row.

along a vortex, under the influence of a boundary, can generate similar phenomena to what we have shown in the present work. In addition, remarkably similar phenomena and vortex structures are found resulting from an oblique collision of a vortex ring to a flat boundary, as studied by Lim (1989).

An axial flow phenomenon similar to that observed for the vortex pair appears to occur as the ring encounters the wall, as shown in figure 1.26. Just as for the vortex pair, the flow moves fluid away from the portion of the ring that encounters the wall first. This flow produces what we call a “collapsed vortex.” Both of these flows involve vorticity cancellation, the formation of a spanwise pressure gradient and a spanwise flow. Both flows also involve vortex rebound and the generation of smaller-scale vortex structures.

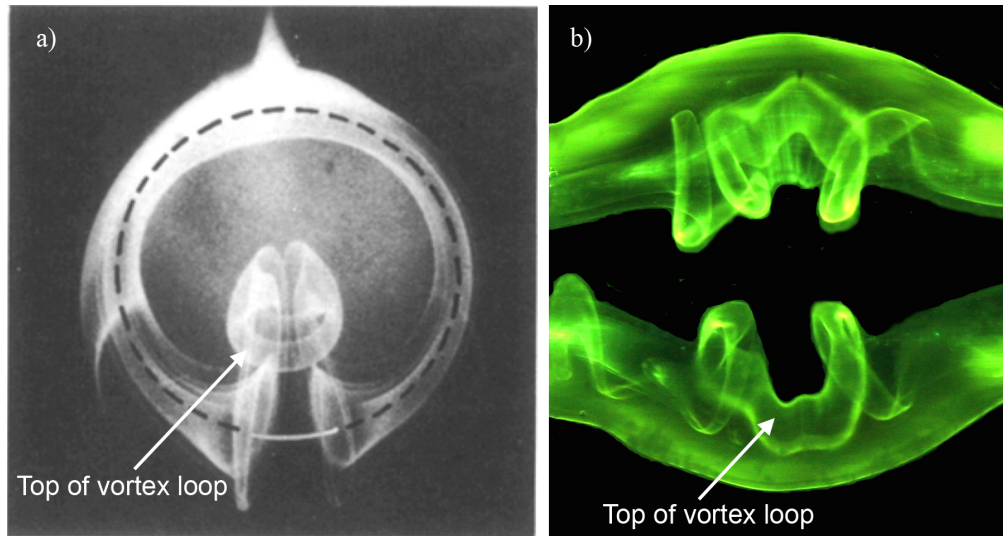


Figure 1.27: Comparison of the evolution of the secondary vorticity of a vortex pair in wall effect with the collision of a vortex ring with an inclined wall from (Lim, 1989) (reprinted by permission from Springer). (a) Secondary vorticity generated by the vortex ring. (b) Secondary vorticity generated by a vortex pair evolving according to the Vertical Rings Mode.

Examination of the secondary vorticity reveals more similarities. Figure 1.27 shows an example of our vortex pair evolving in the manner of the Vertical Rings Mode and Lim’s vortex ring, both in plan view. The secondary vortex structure that gives rise to a vertical vortex ring in the case of the vortex pair is very similar to the loop observed in Lim’s vortex ring. It is possible, then, that a vortex ring colliding obliquely with a wall will change the vortex topology and evolve into a smaller-scale vortex ring or loop, which may then rebound away from the boundary, as we find in our flow. A principal difference between our flow and Lim’s, however, is that the secondary vortices produced by the vortex pair interact with each other along the centerline dividing the two vortices. In the vortex ring experiment, only one such loop is produced.

In presenting his results, Lim (1989) described how the interaction of a vortex ring and an oblique wall causes the formation of “bi-helical” vortex lines close

to the location of first contact between the wall and vortex ring. He suggests that these vortex lines are displaced along the circumferential axis, ultimately compressed around the portions of the ring furthest from the wall, by the induced velocity of the secondary vorticity. He deduces that the no-slip condition of the wall and the corresponding generation of secondary vorticity play a vital role in displacing these vortex lines. In the present work, clearly the generation of secondary vorticity is at the heart of the 3D vortex dynamics, although there is no indication in our flow of the dynamics of helical vortex lines. Certainly, the vortex lines will assume roughly a helical orientation due to the combined axial flow with swirl in the vortex tubes, but we could not observe them directly.

Both Lim (1989) and the subsequent simulations of Verzicco & Orlandi (1994) discuss a sequence of events which leads to the significant changes in vortex topology for the oblique rings. As the oblique ring approaches the wall, vortex stretching occurs first where the ring first comes into contact with the wall. Essentially, in this region of the flow, the radius of the ring grows due to the image effect of the vortex ring in the wall. Due to this stretching, the rate of vorticity annihilation due to viscous diffusion is increased. As the vortex circulation decays, there is a local increase in pressure, which generates axial flow. The above authors then focus on the existence of a vortex loop which arises out of the secondary vorticity, convecting upwards due to its own self-induced motion.

In the case of our flow here, it should be emphasized that vigorous axial flows are found not only in the secondary vorticity but also in the primary vorticity, and both sources of vorticity can have a key role in the subsequent vortex dynamics.

It is suggested by Lim (1989) and Verzicco & Orlandi (1994) that “differen-

tial stretching” causes the axial flow of the secondary vorticity and subsequent ejection of a vortex loop. In our case, the stretching in the manner of a ring spreading out with increasing radius does not occur. We believe that axial flow is not the result of vortex stretching; the stretching is the result of axial flow. However, they clearly occur together.

In the flows discussed here, the initial conditions consist of a vortex pair with a perturbation that approaches a wall. At the point where a vortex first comes into contact with the wall, the presence of the primary vortex causes a boundary layer and pressure gradient to strengthen, resulting in flow separation and the formation of secondary vorticity. Locally, the interaction between the primary and secondary vorticity has a “head start” over other parts of the flow; the rapid growth of secondary vorticity leads to diffusion and rapid cancellation of primary vorticity. The local weakening of the primary vortex strength causes a local increase in pressure and induces axial flow in the vortex tube. The flow away from the point of first contact towards the parts of the vortex furthest from the wall leads to the collapse of the primary vortex. The net result of these vortex dynamics leads typically to the formation of vortex loops or vortex rings which rise up away from the horizontal wall. The formation of these three-dimensional structures “rebounding” from the wall may represent a generic characteristic of such flows.

1.7 Conclusions

In this study, we examine the approach of a vortex pair to a solid boundary, in the case where the vortices are unstable to a long-wave instability. The effects of

a wall lead to distinctly different vortex dynamics, almost unrecognizable compared to the unbounded Crow instability. The interaction of a vortex pair with a wall leads to inhibition of the long-wave instability. The vortices are then subject to localized vorticity cancellation, which causes the development of axial pressure gradients within each vortex, producing strong axial flows. Ultimately quite distinct vortex topologies develop, involving small vortex rings. We believe that these characteristics are not limited to our flow, and are relevant to a broader class of fundamental flows in which a perturbed vortex (or vortex ring) becomes influenced by a wall. The most notable practical application is the vortex wake that forms behind aircraft near a runway and which imposes constraints on airport and runway capacity. However, the phenomena we discuss are also relevant to flows around submerged ship hull appendages as well as flows downstream of vortex generators.

If the vortex pair is generated below a critical initial height, the wall serves to inhibit the three-dimensional (Crow) instability. We observe two modes of vortex-wall interaction. For small heights, the primary vortices are close together, enabling the secondary vortices to interact with each other above the primary pair, forming vertically oriented vortex rings. This unexpected vortex structure represents the principal dynamics of vorticity in this “Vertical Rings Mode,” and represents a three-dimensional version of vortex “rebound.”

In the “Horizontal Rings Mode,” with a range of larger initial heights, the Crow instability develops to a greater extent before wall interaction. The perturbation amplitude grows larger, and this means that the peak locations are farther apart and the troughs closer together upon wall interaction. The proximity of the troughs also increases vorticity cancellation there, leading to a greater

Mode	h_0/b_0	A/b_0 at $h = b_0$	Principal Interaction
Vertical Rings	3 – 6	0.10 – 0.30	Secondary-Secondary
Horizontal Rings	6 – 9	0.30 – 0.50	Primary-Secondary
Large Rings (Crow Instability)	> 9	> 0.50	Primary-Secondary

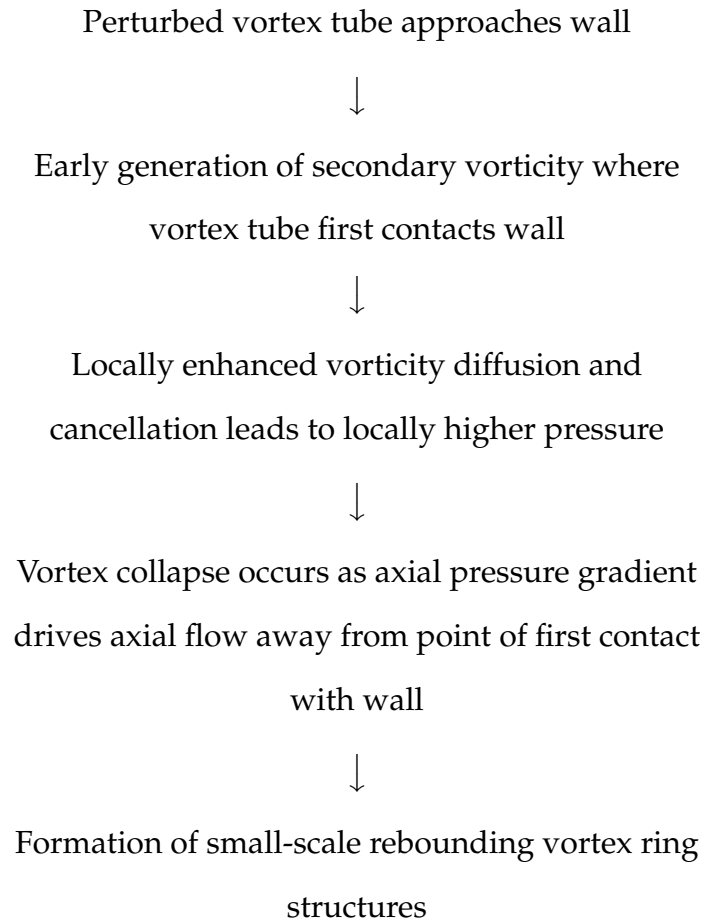
Table 1.1: Summary of principal modes of wall interaction

loss of circulation. Further reduction in circulation is caused by the generation of secondary vorticity in wall effect. This reduction of circulation at the troughs locally leads to a higher pressure compared with the peaks of the vortices, and triggers “vortex collapse” as a result of strong axial flows moving fluid from the troughs toward the peaks. The secondary vortices generated at the peaks are also much farther apart, which inhibits any interaction between them. Instead, the secondary vortices interact with their individual primaries, leading to reconnection and the formation of a series of small, horizontal vortex rings which “rebound” from the wall. There are two small vortex rings in each instability wavelength, quite different from the large Crow vortex rings, one of which is formed per wavelength. As for the first mode, which generates vertical rings, these 3D “rebound effects” of the Horizontal Rings Mode are distinctly different from the 2D rebound observed for straight, unperturbed vortex pairs in wall effect. The results of wall interaction arising from these modes are summarized in table 1.1.

If the vortices are generated above the critical height, the long-wavelength instability causes reconnection to occur at the troughs and a series of vortex rings to be generated. However, because the instability occurs in a plane oriented at 45° to the horizontal, the rings are nonplanar. The “Large Rings Mode” then refers to the interaction of these deformed rings with a boundary. Because they are nonplanar and also change their orientation continuously following re-

connection, the behavior of the rings in wall effect is dependent on the precise height at which they are generated. In many cases, the rings expand upon impinging with the ground plane, as would be expected for axisymmetric rings. In other cases, phenomena evolve which resemble the Horizontal Rings Mode.

The physical mechanisms which are causing these vortex structures to evolve, breaking up spanwise coherence of the original vortex pairs, may be summarized below.



We recognize that there is a significant difference in Reynolds number between this laboratory-scale flow and real flows that exist in the atmosphere. Despite this difference, other studies, such as Leweke & Williamson (2011) have

shown striking similarities in the vortex structures produced across this span of Reynolds numbers. That said, it is unknown whether the structures observed in this study are also produced at higher Reynolds numbers. This does not detract, however, from this flow's relevance to other situations where vortices exist approximately parallel to a surface.

Some studies of aircraft wake vortices, such as Stephan *et al.* (2013) show circulation decay ($\Gamma(t)$) within nondimensional times ($t^* \approx 8 - 10$) which are shorter than some of those observed here. It appears that the time required for the circulation to decay (e.g., to 40% of its initial value) is dependent not only on the configuration of the vortices but also on the Reynolds number. For example, with two-dimensional vortices (figure 1.10), the primary vorticity decays to 40% of its starting value by $t^* = 20$, while, for the Crow instability in wall effect (figure 1.24b), this level of decay is reached by $t^* = 10$. A further example is shown in figure 1.24(a), in which the peaks of the vortices decay to 40% of their initial value by $t^* = 16$, while troughs have already decayed to this level at $t^* = 8$.

The phenomena observed in these experiments are not limited to perturbed vortex pairs. Remarkably similar phenomena are found where vortex rings impinge obliquely with a wall, as discussed in Lim (1989) and Verzicco & Orlandi (1994). The changes in topology of the vorticity, the initiation of axial flow, and the creation of rebounding 3D vortex rings appear to be generic phenomena for flows where perturbed vortices are roughly parallel with a surface. Simulations of these and other flows would illuminate and clarify additional features of the vortex dynamics.

This work was supported by the Office of Naval Research Award No.

N00014-12-421-0712, monitored by Dr. Ron Joslin. The authors would also like to acknowledge the support of the NASA Aeronautics Scholarship Program.

This work previously appeared in print as Asselin & Williamson (2017), © 2017 Cambridge University Press, reprinted with permission.

REFERENCES

- ASSELIN, D.J. & WILLIAMSON, C.H.K. 2017 Influence of a wall on the three-dimensional dynamics of a vortex pair. *J. Fluid Mech.* **817**, 339–373.
- BAKER, G.R., SAFFMAN, P.G. & SHEFFIELD, J.S. 1976 Structure of a linear array of hollow vortices of finite cross-section. *J. Fluid Mech.* **74**, 469–476.
- BAYLY, B.J. 1986 Three-dimensional instability of elliptical flow. *Phys. Rev. Lett.* **57**, 2160–2163.
- CANTWELL, B.J. 1981 Organized motion in turbulent flow. *Annu. Rev. Fluid Mech.* **13**, 457–515.
- CHU, C.C. & FALCO, R.E. 1988 Vortex ring/viscous wall layer interaction model of the turbulence production process near walls. *Exp. in Fluids* **6**, 305–315.
- CROUCH, J.D. 1997 Instability and transient growth for two trailing-vortex pairs. *J. Fluid Mech.* **350**, 311–330.
- CROUCH, J. 2005 Airplane trailing vortices and their control. *Comptes Rendus Physique* **6**, 487–499.
- CROW, S.C. 1970 Stability theory for a pair of trailing vortices. *AIAA J.* **8** (12), 2172–2179.
- DEE, F.W. & NICHOLAS, O.P. 1968 Flight measurements of wing-tip vortex motion near the ground. *Tech. Rep.* 1065. British Aeronautical Research Council.
- DUPONCHEEL, M., COTTIN, C., DAENINCK, G., LEWEKE, T. & WINCKELMANS, G. 2007 Experimental and numerical study of counter-rotating vortex pair dynamics in ground effect. In *18ème Congrès Français de Mécanique*.
- FABRE, D. & JACQUIN, L. 2000 Stability of a four-vortex aircraft wake model. *Phys. Fluids* **12** (10), 2438–2443.
- GEORGES, L., GEUZAIN, P., DUPONCHEEL, M., BRICTEUX, L., LONFILS, T. & WINCKELMANS, G. 2006 Les of two-vortex system in ground effect (longitudinally uniform wakes). *Tech. Rep.* AST4-CT-2005-012238. 6th FAR Wake – Framework Programme for Research and Technological Development.
- GUPTA, G. 2003 Generation and evolution of a viscous vortex pair. Master’s thesis, Cornell University.
- HARRIS, D.M. & WILLIAMSON, C.H.K. 2012 Instability of secondary vortices generated by a vortex pair in ground effect. *J. Fluid Mech.* **700**, 148–186.

- HARVEY, J.K. & PERRY, F.J. 1971 Flowfield produced by trailing vortices in the vicinity of the ground. *AIAA J.* **9** (8), 1659–1660.
- KIDA, S. & TAKAOKA, M. 1994 Vortex reconnection. *Annu. Rev. Fluid Mech.* **26**, 169–189.
- KLEIN, R., MAJDA, A.J. & DAMODARAN, K. 1995 Simplified equations for the interaction of nearly parallel vortex filaments. *J. Fluid Mech.* **288**, 201–248.
- KRAMER, W., CLERCX, H.J.H. & VAN HEIJST, G.J.F. 2007 Vorticity dynamics of a dipole colliding with a no-slip wall. *Phys. Fluids* **19**, 126603.
- LAMB, H. 1932 *Hydrodynamics*, 6th edn. Cambridge University Press.
- LEWEKE, T., LEDIZÈS, S. & WILLIAMSON, C.H.K. 2016 Dynamics and instabilities of vortex pairs. *Annu. Rev. Fluid Mech.* **48**, 1–35.
- LEWEKE, T. & WILLIAMSON, C.H.K. 1998 Cooperative elliptic instability of a vortex pair. *J. Fluid Mech.* **360**, 85–119.
- LEWEKE, T. & WILLIAMSON, C.H.K. 2011 Experiments on long-wavelength instability and reconnection of a vortex pair. *Phys. Fluids* **23**, 024101.
- LIM, T.T. 1989 An experimental study of a vortex ring interacting with an inclined wall. *Exp. in Fluids* **7**, 453–463.
- LUTON, J.A. & RAGAB, S.A. 1997 The three-dimensional interaction of a vortex pair with a wall. *Phys. Fluids* **9** (10), 2967–2980.
- MELANDER, M.V. 1988 Close interactions of 3d vortex tubes. *Tech. Rep.*. Center for Turbulence Research.
- MELANDER, M.V. & HUSSAIN, F. 1988 Cut-and-connect of two antiparallel vortex tubes. In *Center for Turbulence Research Proceedings of the Summer Program*, pp. 257–286.
- MOET, H. 2003 Simulation numérique du comportement des tourbillons de sillage dans l’atmosphère. PhD thesis, Institut National Polytechnique de Toulouse.
- MOET, H., LAPORTE, F., CHEVALIER, G. & POINSOT, T. 2005 Wave propagation in vortices and vortex bursting. *Phys. Fluids* **17**, 054109.
- ORLANDI, P. 1990 Vortex dipole rebound from a wall. *Phys. Fluids* **2** (8), 1429–1436.
- ORTEGA, J.M., BRISTOL, R.L. & SAVAŞ, Ö. 2003 Experimental study of the instability of unequal-strength counter-rotating vortex pairs. *J. Fluid Mech.* **474**, 35–84.

- PANTON, R.L. 2001 Overview of the self-sustaining mechanisms of wall turbulence. *Prog. Aero. Sci.* **37**, 341–383.
- PEACE, A.J. & RILEY, N. 1983 A viscous vortex pair in ground effect. *J. Fluid Mech.* **129**, 409–426.
- PIERREHUMBERT, R.T. 1986 Universal short-wave instability of two-dimensional eddies in an inviscid fluid. *Phys. Rev. Lett.* **57** (17), 2157–2159.
- QUACKENBUSH, T.R., BILANIN, A.J. & MCKILLIP, R.M. 1996 Vortex wake control via smart structures technology. In *Proc. SPIE 2721, Smart Structures and Materials 1996: Industrial and Commercial Applications of Smart Structures Technologies* (ed. C. Robert Crowe), pp. 78–92.
- RENNICH, S.C. & LELE, S.K. 1999 Method for accelerating the destruction of aircraft wake vortices. *J. Aircraft* **36** (2), 398–404.
- ROBINSON, S.K. 1991 Coherent motions in the turbulent boundary layer. *Annu. Rev. Fluid Mech.* **23**, 601–639.
- SAFFMAN, P.G. 1989 A model of vortex reconnection. *J. Fluid Mech.* **212**, 395–402.
- SAFFMAN, P.G. 1992 *Vortex Dynamics*. Cambridge University Press.
- SHELLEY, M.J., MEIRON, D.I. & ORSZAG, S.A. 1993 Dynamical aspects of vortex reconnection of perturbed anti-parallel vortex tubes. *J. Fluid Mech.* **246**, 613–652.
- SPALART, P.R. 1998 Airplane trailing vortices. *Annu. Rev. Fluid Mech.* **30**, 107–138.
- STEPHAN, A., HOLZÄPFEL, F. & MISAKA, T. 2013 Aircraft wake-vortex decay in ground proximity: physical mechanisms and artificial enhancement. *J. Aircraft* **50** (4), 1250–1260.
- SWEARINGEN, J.D., CROUCH, J.D. & HANDLER, R.A. 1995 Dynamics and stability of a vortex ring impacting a solid boundary. *J. Fluid Mech.* **297**, 1–28.
- THIELICKE, W. 2014 The flapping flight of birds - analysis and application. PhD thesis, Rijksuniversiteit Groningen.
- THIELICKE, W. & STAMHUIS, E.J. 2014a Pivlab – towards user-friendly, affordable and accurate digital particle image velocimetry in matlab. *J. Open Research Software* **2** (1).
- THIELICKE, W. & STAMHUIS, E.J. 2014b Pivlab - time-resolved digital particle image velocimetry tool for matlab (version: 1.40).

- VERZICCO, R. & ORLANDI, P. 1994 Normal and oblique collisions of a vortex ring with a wall. *Meccanica* **29**, 383–391.
- WALEFFE, F. 1990 On the three-dimensional instability of strained vortices. *Phys. Fluids A* **2** (1), 76–80.
- WALKER, J.D.A., SMITH, C.R., CERRA, A.W. & DOLIGALSKI, T.L. 1987 The impact of a vortex ring on a wall. *J. Fluid Mech.* **181**, 99–140.
- WIDNALL, S.E., BLISS, D.B. & TSAI, C.-Y. 1974 The instability of short waves on a vortex ring. *J. Fluid Mech.* **66**, 35–47.
- WILLIAMSON, C.H.K., LEWEKE, T., ASSELIN, D.J. & HARRIS, D.M. 2014 Phenomena, dynamics and instabilities of vortex pairs. *Fluid Dyn. Res.* **46**, 061425.

CHAPTER 2
ADDITION OF PASSIVE DYNAMICS TO A HEAVING AIRFOIL TO
IMPROVE PERFORMANCE

Abstract

In this work, we are interested in the performance of a pitching and heaving airfoil in which the pitching motion is controlled passively by a torsion spring. Flapping airfoils have been studied extensively for application to small aerial and underwater vehicles that could be used for reconnaissance, search and rescue, and environmental monitoring. However, despite advances in power storage and electronic miniaturization, these devices often are still subject to significant constraints on the mass and energy allocable to their propulsive subsystems. Many studies have shown the benefits to propulsive performance provided by oscillating the airfoil in both pitch and heave. Traditionally, two actuators would be required for these two degrees of freedom. The performance of the system could potentially be improved significantly if one of these actuators could be removed and replaced by passive dynamics.

We simulate an airfoil which is forced in the heave direction but whose pitching motion is subject to a control by a torsion spring using a cyber-physical force-feedback technique. The use of force feedback allows us to specify the location of the pivot point and the spring stiffness virtually in software. When the airfoil is controlled in this manner, we observe distinct resonance peaks in the thrust coefficient, which allow the airfoil to produce up to an order of magnitude more thrust as when actuated in heave alone. In addition, the point about which the airfoil pivots strongly influences its performance. For pivot locations located

forward of the airfoil's center of mass, thrust is generated. Conversely, for pivots downstream of the center of mass, there is a negative resonance, and the airfoil produces large amounts of drag. This behavior is also related to the phase difference between the pitching and heaving motions. Pitching leads heaving when the airfoil produces thrust, and heaving leads pitching when drag is generated. The overall performance of the airfoil as a propulsor is comparable to one in which both axes are actively controlled. Consequently, if the airfoil's operation is properly tuned, it is possible to derive excellent thrust performance without the added expense, mass, and power requirements of a second actuator.

2.1 Introduction

Interest in vehicles which propel themselves through the use of flapping wings has increased markedly in recent years, as shrinking electronics and power sources enable the construction of small, potentially autonomous, aerial and underwater craft. Such vehicles could have a broad range of applications, including surveillance and reconnaissance and search and rescue missions. The remarkable maneuverability of many flying and swimming animals which employ flapping wings has inspired research into the use of such motions for lift generation and propulsion (Jones *et al.*, 2005). Unfortunately, such small vehicles often suffer from constraints on the amount of energy storage they have available or the mass they can carry. In this work, we present a technique using passive dynamics that significantly improves the performance of the airfoil as a propulsor while not adding significant weight to the system.

There is an extensive body of research concerned with biomimetic motions, such as those used by various types of fish. The principal types and their characteristics are reviewed in Sfakiotakis *et al.* (1999). Other studies, including the present one, use more traditionally shaped aerodynamic foils, such as the NACA 0012 airfoil. In the context of flapping airfoils, two motions are typically examined. The first motion, heaving or plunging, is defined as translation transverse to the airfoil chord, as shown in figure 2.1(a). The second motion, pitch, is a pure rotation about a designated pivot point on the airfoil, shown in figure 2.1(b). Many studies of oscillating flat plates and airfoils are reviewed in McCroskey (1982), Rozhdestvensky & Ryzhov (2003), and Platzer *et al.* (2008).

Knoller (1909) and Betz (1912) were the first to describe how changes in the

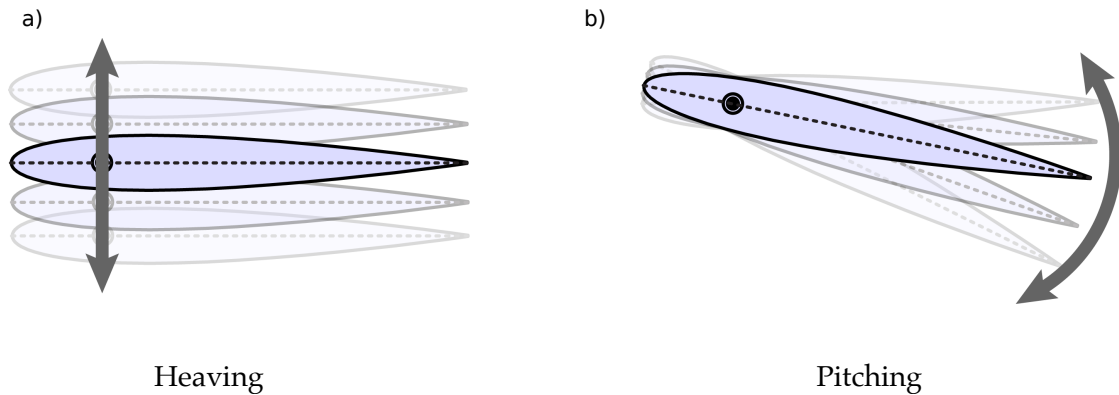


Figure 2.1: (a) Heaving is motion transverse to the airfoil chord. (b) Pitching is a pure rotation about a given pivot point.

angle of attack seen by a heaving airfoil can rotate the lift vector into the direction of motion and produce thrust. These results were later confirmed experimentally by Katzmayr (1922).

More recently, purely heaving airfoils have been studied both experimentally and computationally. Tuncer & Platzer (1996) have shown using a Navier-Stokes solver that efficiencies can be as high as 70% at a Reynolds number of three million. At the lower Reynolds numbers at which birds and small micro-aerial vehicles operate, however, efficiencies are typically smaller, around 30%, as observed experimentally by Heathcote & Gursul (2007) and through computations by Ashraf *et al.* (2012).

In contrast to heaving airfoils, a pitching airfoil has no steady mechanism through which thrust can be generated. Instead, thrust is produced purely by unsteady aerodynamic processes. Efficiencies are typically much lower than those observed from a purely heaving airfoil, as shown by Buchholz & Smits (2008) and Mackowski & Williamson (2015). In both cases, propulsive efficiencies do not exceed about 20%.

In an effort to achieve higher propulsive efficiency, other recent studies have examined combined pitching and heaving motions. Anderson *et al.* (1998) describe such an experiment using a NACA 0012 airfoil pivoted about its one-third-chord location. These experiments showed that it is possible to achieve very high values of efficiency, up to 87% at a Reynolds number of 40,000, by carefully controlling the amplitudes of pitch and heave and consequently the maximum instantaneous angle of attack reached by the airfoil during a cycle. Specifically, it is desirable to have a large heaving amplitude and a moderate maximum angle of attack (between 15° and 25°). They also explored the role of the wake configuration on the performance of the airfoil, concluding that an inverse von Kármán vortex street produces the highest efficiency. The formation of the optimal wake was also dependent on the phase angle between the pitching and heaving motions and the presence of a leading edge vortex. Maximum efficiency occurred for a phase angle of 75° . When the phase angle was less than about 90° , the leading edge vortex suction provided a force contributing to thrust and enhancing efficiency. Conversely, the leading edge vortex contributed to drag for phase angles greater than about 90° , causing a corresponding reduction in efficiency.

The importance of the leading edge vortex (LEV) has also been confirmed through numerical simulations by Young & Lai (2007) in the context of a heaving airfoil. Overall, the effect of flow separation at the leading edge is to reduce efficiency. This effect is minimized as Strouhal number is increased, leaving less time available for the LEV to form and to change the pressure distribution in a way that is detrimental to thrust production. Changes in the wake geometry at high Strouhal numbers also lead to reduced efficiency; the combination of these effects is responsible for an efficiency peak near Strouhal numbers of 0.2-0.4.

Most biological systems also operate in this range (Triantafyllou *et al.*, 1993).

Read *et al.* (2003) used a towing tank facility to perform parameter sweeps across a range of Strouhal numbers and maximum instantaneous angles of attack for a pitching and heaving airfoil. The resulting contour plots of thrust coefficient and propulsive efficiency show that there are broad regions where efficiency is high, over 70%, and where useful thrust is still available. As in many other studies, however, operation at higher Strouhal numbers produces an increase in net thrust but also requires operating at lower efficiency. The phase angle between pitch and heave producing maximum thrust was found to be 90° , with pitch leading heave. Optimal efficiency occurred for Strouhal numbers ranging from 0.1 to 0.4, which is consistent with most biological examples of flapping propulsion.

Furthermore, as explored in Read *et al.* (2003) and in greater detail in Hover *et al.* (2004), the use of a sinusoidal profile for the instantaneous angle of attack produces the best overall performance. With sinusoidal pitching and heaving motion profiles, the angle of attack profile increasingly deviates from harmonic as the oscillation frequency is increased. Multiple maxima and minima appear in each cycle. These multiple peaks cause additional vortex shedding, leading to the breakdown of the organized, inverse von Kármán street that is characteristic of good performance. These deficits can be corrected by adjusting the pitching motion profile to return the angle of attack profile to that of a cosine function. Efficiency and thrust are both increased. Other advantages may also be derived from modifying the standard harmonic oscillation profiles, as explored in Israelevitz & Triantafyllou (2014). They show that more exotic motions can be designed to optimize a propulsor for thrust or lift production, depending on

vehicle requirements.

Beyond experiments and computations, analytical studies of oscillating airfoils date back many decades and include early analysis to understand the phenomenon of aerodynamic flutter. Theodorsen (1935) developed a linearized aerodynamic theory that could be used to predict the lift and moment produced by a pitching and heaving plate, and Garrick (1936) later extended Theodorsen's theory to develop an analytical model for thrust. Recent work by Fernandez-Feria (2016) further extended Theodorsen's theory to compute thrust using the full vorticity distribution around the airfoil. These models are inviscid, assume small amplitudes of motion, and restrict the wake to a two-dimensional configuration, located at the centerline of the motion. Consequently, they are unable to capture viscous effects such as the formation of leading edge vorticity and early flow separation along the airfoil chord. Despite these limitations, there are situations in which the linearized theory performs reasonably well (Anderson *et al.*, 1998; Mackowski & Williamson, 2015), at least in capturing the qualitative behavior of the airfoil performance, specifically its thrust and propulsive efficiency.

As combined pitching and heaving motions clearly show the most promise for building an effective propulsor, it is desirable to build vehicles which employ motion in both of these directions. Unfortunately, the relatively inexpensive, small-scale vehicles under consideration for many applications have significant constraints on weight and power storage and may not be able to support the use of two flapping actuators. Consequently, it would be advantageous to produce both heaving and pitching motions using a single actuator. One approach to this problem is to use a mechanical linkage between the two axes, so that

motion in each can be driven by a single motor. Such an approach was adopted by McKinney & DeLaurier (1981) for energy harvesting. This solution has the disadvantage of requiring a more complex mechanical system for mounting the propulsor and may still add unwanted weight.

Many researchers draw inspiration from biological propulsion and add flexibility to the airfoil structure. Flexible wings allow the addition of motion in a second axis without any additional mechanical components. Heathcote & Gursul (2007) found that flexibility can increase propulsive efficiency by about 15% in addition to increasing the thrust coefficient. The pitching motion enabled by making the wing flexible reduced the maximum angle of attack reached during a cycle, thereby reducing the strength of the leading edge vorticity. As discussed in Lewin & Haj-Hariri (2003), the behavior of this leading edge vortex is critical to achieving high efficiency. Strong leading edge vortices which separate early tend to alter the distribution of forces over the airfoil and perturb the downstream wake in a manner that is detrimental to thrust production and increases input power requirements.

Other studies that have examined flexible airfoils have noted the importance of the resonance condition, the point at which the applied forcing frequency for the heaving motion nearly matches the natural frequency of the system. Michelin & Llewellyn-Smith (2009) used a potential flow model to evaluate the performance of a flexible sheet subject to a heaving motion at the leading edge. Both thrust coefficient and propulsive efficiency increased as the sheet was made more flexible, and the condition producing peak thrust corresponded to the point at which resonance between the applied heaving frequency and the natural frequency of the system occurred. As flexibility was further increased,

thereby moving the system away from its resonance point, performance was found to degrade significantly, ultimately transitioning to increased drag.

A simpler alternative to flexibility for the implementation of passive dynamics is the use of rigid foil attached to a spring. Mackowski & Williamson (2017) examined the case of an airfoil which was attached to a linear spring at its pivot point. Commanded to pitch according to a sinusoidal input function, the airfoil was allowed to heave passively under the influence of the spring. They found that the addition of the passive dynamics could double the thrust produced while maintaining the same propulsive efficiency. Even larger thrust coefficients were possible if the system were operated near its resonance condition. They also illuminated the importance of the pivot location, finding that pivoting at or up to one chord-length downstream of the airfoil's trailing edge produced the highest thrust and efficiency.

This study serves as the complement to Mackowski & Williamson (2017), in which an airfoil subject to controlled pitching motions is allowed to heave passively. Here, we examine the opposite situation, in which the airfoil is forced in heave but allowed to pitch passively under the control of a torsion spring, as shown in figure 2.2. Aspects of this configuration have previously been investigated experimentally and computationally by Spagnolie *et al.* (2010). In their experimental setup, two elliptical wings connected to torsion springs at their leading edges were heaved vertically in a circular water tank. The wings could also pitch passively under the control of the springs and propelled themselves in a circle in the tank. They found frequency ranges in which the pitching airfoil outperformed a purely heaving airfoil and other ranges in which it underperformed. In some cases, the wings even moved backwards in the tank. Moore

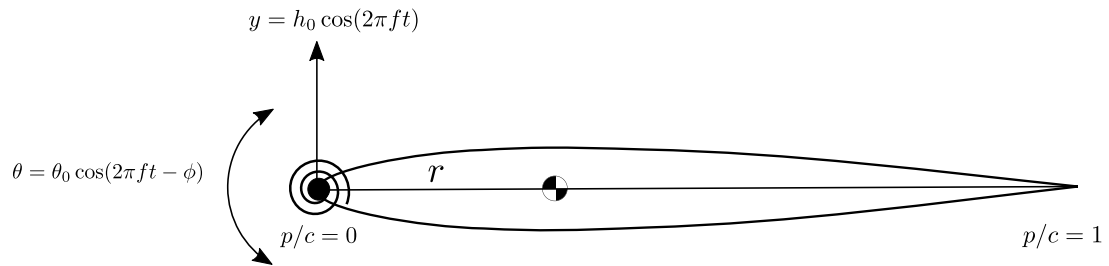


Figure 2.2: Schematic of an actively heaving, passively pitching airfoil. The pivot point (shown as the black dot and defined by the distance r from the airfoil center of mass to the chosen pivot) can be adjusted anywhere along the airfoil chord line or even to positions not physically on the airfoil itself. A torsion spring colocated with the pivot controls the pitching motion. The heaving motion is defined sinusoidally and is applied at the pivot location.

(2014) approached the problem of an actively heaving, passively pitching airfoil analytically in the small amplitude limit, extending the work of Wu (1961). He confirmed in this context that allowing the wing to pitch moderately can produce up to a threefold gain in thrust, particularly when operating near the resonance frequency. Efficiency also improved with added pitching, although no optimum was observed. As driving frequency was increased beyond the point of maximum thrust, performance degraded, and the heaving and pitching oscillations became out-of-phase with each other. As with many other studies, a phase difference between pitching and heaving of 90° produced the best thrust coefficient.

In this experiment, the passive pitching motion is governed by a torsion spring which is positioned at a pivot point along the line defining the airfoil chord. The non-dimensional pivot point p/c is defined to be zero at the leading edge and one at the trailing edge of the airfoil. Motion in the transverse, heaving direction is prescribed by a sinusoidal function with amplitude h_0 and frequency f .

$$y(t) = h_0 \cos(2\pi ft) \quad (2.1)$$

The pitching motion that occurs as a result of the passive dynamics is well-represented by a sinusoidal function with an amplitude θ_0 and phase shift ϕ relative to the heaving motion.

$$\theta(t) = \theta_0 \cos(2\pi ft - \phi) \quad (2.2)$$

Here, we are interested in the thrust and efficiency that can be achieved under a variety of operating conditions and particularly around the resonance point, when the forcing frequency of heave f approaches the natural frequency of the torsion spring system f_n . Previous studies have typically examined one pivot point with either actively or passively controlled pitching. Consequently, we would also like to understand changes in performance caused by moving the pivot location to different positions along the airfoil chord, including points which are not physically located on the airfoil itself. Finally, we are also interested in the motion dynamics and wake configurations that determine the performance of the airfoil.

In this paper, experimental methods are presented in §2.2, followed by a discussion of some preliminary studies in which both pitch and heave are actively controlled in §2.3. The thrust and efficiency of an airfoil undergoing active heave and passive pitch are discussed in §2.4, with particular attention given to variations in performance as functions of frequency ratio and normalized pivot location. We find that the pivot location is an important parameter because it is responsible for determining whether the airfoil will produce a thrust in the de-

sired direction of motion or a drag force in the opposite direction. Comparisons to the performance of fully actively controlled systems as well as the analytical methods of Theodorsen (1935), Garrick (1936), and Fernandez-Feria (2016) are also discussed. Further discussion of the motion dynamics of the passively pitching airfoil follows in §2.5. Here, we employ “trajectory diagrams” to synchronize the position of the airfoil with parameters such as maximum instantaneous angle of attack and the forces produced. The phase angle between the pitching and heaving motions is found to be a critical parameter in determining whether a particular operating point will produce thrust or drag. Furthermore, there are several suboptimal yet interesting operating conditions which should be avoided in the construction of a practical propulsive device. In §2.6, we examine the vortex wake configuration responsible for producing both thrust and drag as the airfoil is operated in various modes. Finally, conclusions follow in §2.7.

2.2 Experimental Methods

Experiments are conducted at the Cornell University Fluid Dynamics Research Laboratories using our hybrid X - Y - θ water channel. This facility consists of an Eidetics model 1520 free-surface, closed-loop water channel with a test section of width 38 cm, length 150 cm, and depth 46 cm. A rigid NACA 0012 airfoil section of chord 10 cm and submerged depth 24 cm is attached vertically to a carriage capable of motion in the streamwise (x), transverse (y), and rotational (about the vertical axis) (θ) directions. The airfoil penetrates the free surface at the top of the channel, and at the bottom, an endplate is used to reduce three-dimensional effects. Forces are measured using 6-axis force/torque

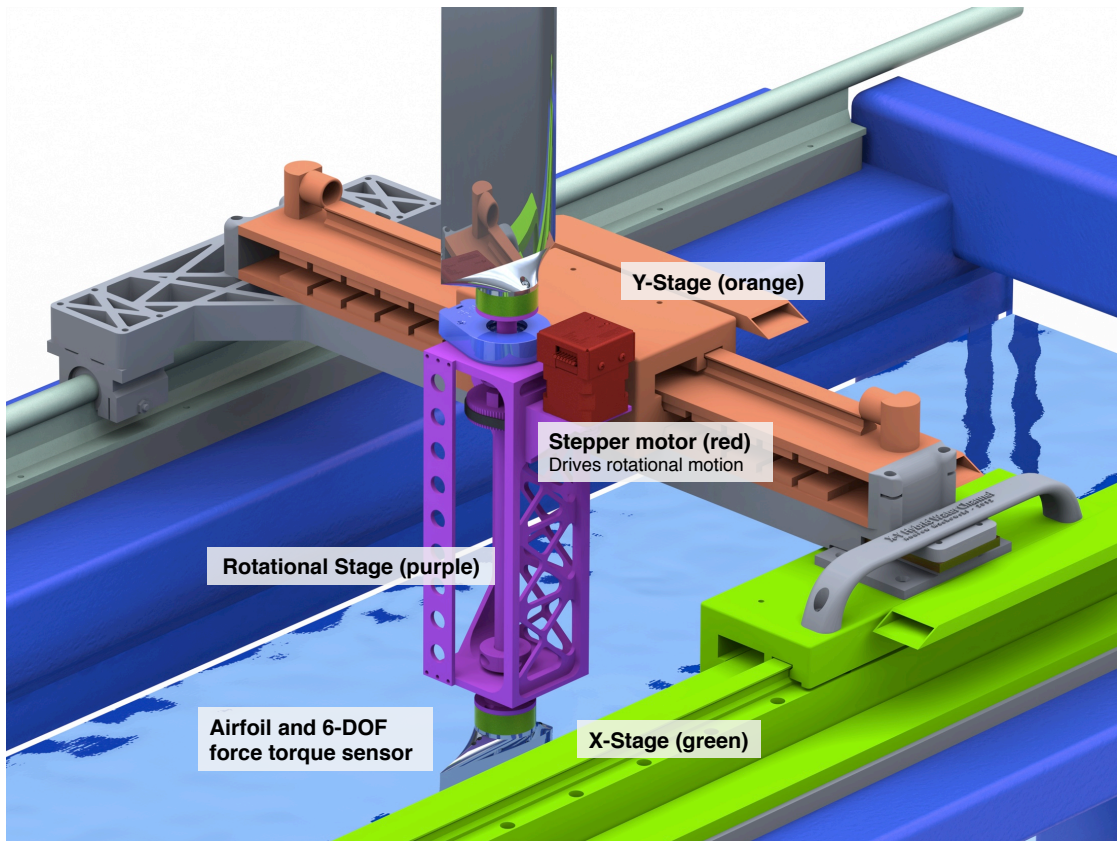


Figure 2.3: Schematic showing the X-Y- θ hybrid water channel. The streamwise (x) linear stage is shown in light green, and the transverse (y) linear stage is in orange. Rotation is provided by a stepper motor, shown in red, which drives the rotational stage (purple). Each airfoil is attached to a 6-axis force/torque sensor, shown in dark green.

sensors from ATI Industrial Automation. A schematic showing the major components of this facility is shown in figure 2.3.

All three degrees of freedom are controlled by a computer system equipped with force feedback. This system allows the specification of virtual forces and moments in addition to the measured fluid forces and also allows us to change the dynamical properties of the airfoil, such as its mass and moment of inertia, completely in software. Two airfoils are employed: one in the air and one in the water. The airfoil in the air measures the inertial forces produced by accelerating

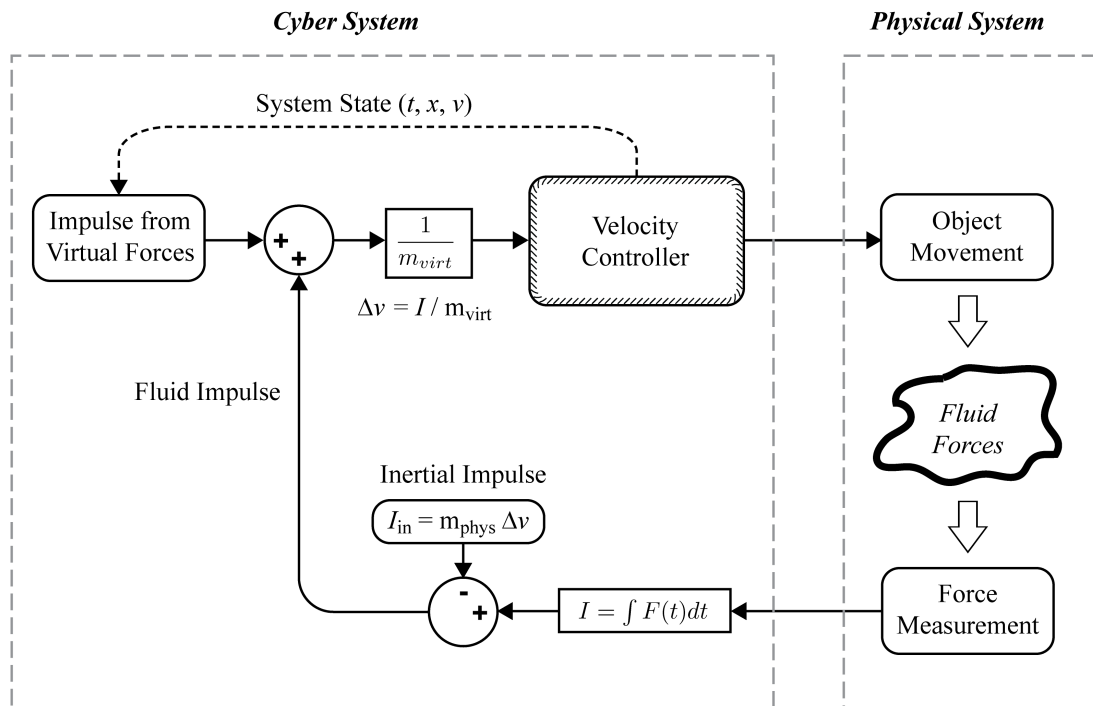


Figure 2.4: Schematic showing operation of the Cyber-Physical Fluid Dynamics (CPFD) control system (Mackowski & Williamson, 2011; Mackowski, 2014). The measured fluid impulse is combined with the virtual impulse calculated from forces specified in software. The resulting total impulse is then used to compute velocity commands which move the test object through the water.

the airfoil, which permits them to be subtracted from the forces measured by the airfoil in the water, allowing us to measure the fluid forces independently. We call this technique “Cyber-Physical Fluid Dynamics” (CPFD), and a flow chart illustrating its principles of operation is shown in figure 2.4.

With CPFD, the fluid impulse I , defined as the integral of the force over a timestep, measured by the force/torque sensors is computed and combined with the impulse of any virtual forces that are specified by equations in software, as shown in figure 2.4. Division by the arbitrary virtual mass of the airfoil gives the velocity increments for each axis at a given time step. Corresponding velocity commands are then sent to the three motors controlling the airfoil in the

x , y , and θ directions, which make it move as if it were subject to both the fluid and virtual forces together. The system is also capable of independently controlling the speed of the water channel pump, using a laser doppler velocimeter to measure the flow speed in the test section. This approach allows the experiment to be almost fully automated. Scripts can be created that run batches of experiments for days at a time without any manual intervention. Further details on the operation of CPFDF are available in Mackowski & Williamson (2011) and Mackowski (2014). It should also be noted that the application of a force-feedback control system to fluid dynamics problems was first explored by Hover *et al.* (1998) for one degree of freedom. Our facility expands this technique to multiple degrees of freedom and incorporates a water channel to enable experiments of indefinite duration.

The CPFDF technique has been validated by comparison with purely physical experiments for which solutions are already known. For example, the decay of a mass-spring-damper system is shown in figure 2.5(a). This experiment was conducted with both airfoils oscillating in air so that no fluid damping forces were present. Another comparison to a physical experiment is shown in figure 2.5(b). This vortex-induced vibration experiment involving a circular cylinder was originally performed by Govardhan & Williamson (2000). The amplitude of the VIV response derived from the CPFDF technique agrees remarkably well with the physical experiment.

Using the mass-spring-damper system, a timestep refinement study was also conducted to verify that the speed at which the force-feedback loop runs is sufficient to produce reliable results. Degradation of the damped harmonic oscillator response was observed beginning at a loop rate of 20kHz. All experiments were

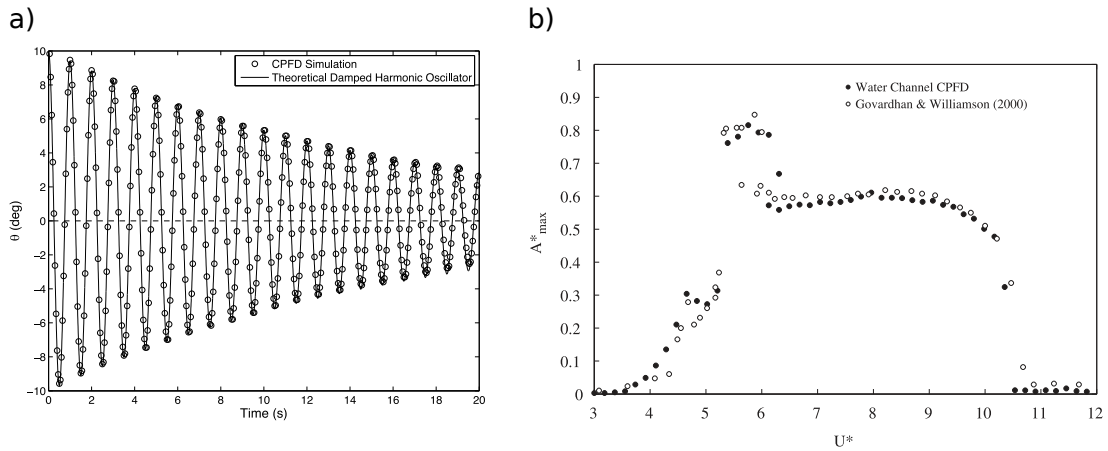


Figure 2.5: (a) Damped harmonic oscillator response from a CPFD simulation compared with the theoretical response of such a system. In the tested system, the damping ratio is 0.01, and the natural frequency is 1 Hz. (b) Amplitude of VIV response for a circular cylinder from both a cyber-physical experiment and a purely physical experiment (Mackowski & Williamson, 2011; Govardhan & Williamson, 2000) (reprinted with permission from Elsevier).

consequently run with this loop execution rate set to 80kHz.

In our present experiment, we simulate an airfoil undergoing active heave and passive pitch. Pitching is controlled by a torsion spring at the pivot location, which produces a moment given by $-\kappa\theta$, where κ is the spring stiffness and θ is the angular position of the airfoil. This equation is implemented virtually in software, which enables the use of an infinite range of springs with no need to change the physical hardware in the experiment.

There are important differences between actively and passively controlled systems with regard to the parameters that need to be set for each experiment. These are summarized in table 2.1. The key difference is that for an actively controlled pitching system, the pitching amplitude and phase are determined before the experiment is run. For a system with passive pitch, these parameters are chosen by the dynamics of the system and must be measured after the exper-

[Active Heave]-[Active Pitch]		[Active Heave]-[Passive Pitch]	
Parameter	Definition	Parameter	Definition
ρ	Fluid density	ρ	Fluid density
μ	Fluid viscosity	μ	Fluid viscosity
c	Chord length	c	Chord length
p	Pivot location	p	Pivot location
U_∞	Freestream velocity	U_∞	Freestream velocity
f_h	Heaving frequency	f_h	Heaving frequency
$f_p = f_h$	Pitching frequency	$f_p = f_h$	Pitching frequency
h_0	Heaving amplitude	h_0	Heaving amplitude
A_{TE}	Trailing edge displacement	A_{TE}	Trailing edge displacement
θ_0	Pitching amplitude	θ_0	Pitching amplitude (measured)
ϕ	Pitching phase	ϕ	Pitching phase (measured)
		f_n	Natural frequency

Table 2.1: Parameters defining each cyber-physical experiment for actively and passively pitching systems.

iment is complete. The passive system has an additional parameter, however, in the natural frequency f_n , defined by equation 2.3, in which I is the moment of inertia of the airfoil about its pivot point.

$$f_n = \frac{1}{2\pi} \sqrt{\frac{\kappa}{I}} \quad (2.3)$$

Other important non-dimensional parameters are summarized in table 2.2. In these experiments, the Reynolds number is set to 10,000, and the reduced frequency is 0.50 unless otherwise noted. The heave-to-chord ratio is 0.25, and the non-dimensional pivot location p/c varies from -5 to 5, where $p/c = 0$ at the leading edge and $p/c = 1$ at the trailing edge. The Strouhal number based on the heaving amplitude, which is often discussed in biological contexts, is 0.25, which is in the range in which fish and birds typically operate.

The principal metrics used to evaluate the performance of the airfoil are the thrust coefficient in the x-direction and the propulsive efficiency. The thrust

Parameter	Definition
$Re = \frac{\rho U_\infty c}{\mu}$	Reynolds number
$St = \frac{A_{TE} f}{U_\infty}$	Strouhal number
$k = \frac{f c}{U_\infty}$	Reduced frequency
h_0/c	Heave-to-chord ratio
p/c	Pivot location
f/f_n	Frequency ratio

Table 2.2: Non-dimensional parameters for an active heave, passive pitch system.

coefficient (equation 2.4) employs the average thrust and is normalized in the usual manner for force coefficients.

$$C_T = \frac{\bar{T}}{\frac{1}{2}\rho U_\infty^2 S} \quad (2.4)$$

where \bar{T} is the average thrust in the x-direction produced by the airfoil, ρ is the fluid density, U_∞ is the channel velocity, and S is the planform area of the airfoil.

The input power coefficient is needed to compute the propulsive efficiency and is given by equation 2.5.

$$C_P = \frac{\bar{P}}{\frac{1}{2}\rho U_\infty^3 S} \quad (2.5)$$

where \bar{P} is the average input power to the airfoil, given by

$$\bar{P} = \frac{1}{T} \left(\int_0^T F_{motor}(t) \dot{h}(t) dt \right) \quad (2.6)$$

in which T is the period of one oscillation cycle, F_{motor} is the force produced by the linear motor in the heave direction, and \dot{h} is the heaving velocity of the pivot point.

The propulsive efficiency η is then defined by the ratio of the thrust coefficient to the power coefficient:

$$\eta = \frac{C_T}{C_P} \quad (2.7)$$

In a typical batch of experiments, a pivot location is selected and the frequency ratio is varied over a range of zero to five by changing the spring stiffness and therefore the natural frequency of the system. Each experiment is run for three minutes, and the first 30 seconds of data collected are discarded in order to allow the system to reach steady state. All output variables are phase-averaged using approximately 75 cycles. Experiment parameters are selected so that the resulting motion of the airfoil remains comfortably outside the range where excessive sloshing or wave action occur.

The airfoil is mounted to the rotational stage such that it pivots about its center of mass. However, the pivot location is one of the key parameters that we would like to vary. This can be done easily by combining rotational motion with additional motion in the x - and y -directions. Velocity commands given by the following equations are computed in real time by the computer control system and allow the pivot point to be set arbitrarily, even to points not physically located on the airfoil itself.

$$\dot{x} = r \sin(\theta)\dot{\theta} \quad (2.8)$$

$$\dot{y} = -r \cos(\theta)\dot{\theta} \quad (2.9)$$

where r is the distance from the airfoil's center of mass to the desired pivot location, p/c . Since p is measured from the airfoil's leading edge, $r = p - x_{CoM}$, where x_{CoM} is the chordwise coordinate of the airfoil's center of mass, also measured from the leading edge.

In order to examine the vortical wake structure formed by the airfoil, we use particle image velocimetry (PIV). The particles are Potters' Industries Spheri-
cel 110P8 (mean diameter $10\mu m$ and density $1.10gcm^{-3}$). Illumination is provided by a New Wave Research dual Nd:YAG laser, formed into a 3-mm thick light sheet using a series of hemispherical and cylindrical lenses. Photographs are taken by a JAI CV-M2CL 2-megapixel camera at a rate of 8 Hz, yielding 16 frames per cycle of the airfoil motion. The laser and camera are controlled by the same LabVIEW program that controls the airfoil, enabling precise control over the timing of the images and allowing PIV frames to be phase-averaged. PIVLab running in MATLAB is used to compute the velocity fields (Thielicke & Stamhuis, 2014a,b; Thielicke, 2014) with a final subwindow size of 64×64 pixels and 50% overlap. Typically, three PIV experiments were run for each case, with the airfoil located at three different positions in the test section, one with the airfoil positioned within the camera field of view, and two others with the airfoil located further upstream from the fixed camera position. This method provides images that span a distance downstream from the airfoil equal to the entire test section length and are combined in post-processing to create a single,

continuous view of the wake.

Typical uncertainties in our measured quantities were quantified by running multiple identical experiments. For force measurements, each data point represents the average of approximately 75 identical motion cycles. The bootstrap method is used to estimate the random experimental error associated with each of the measurements of interest. For a pivot location one chord-length upstream of the leading edge, the 95% confidence interval for the thrust coefficient is approximately $\pm 1.26\%$. For the efficiency, the uncertainty is approximately $\pm 1.13\%$. When the pivot is located at the trailing edge, the typical uncertainties are $\pm 1.75\%$ for thrust coefficient and $\pm 1.66\%$ for propulsive efficiency. Consequently, the experiment is quite repeatable.

2.3 Preliminary Studies

Before examining the passively pitching airfoil, it is important to examine the behavior of a fully actively controlled system (Active-Heave, Active-Pitch). Figure 2.6(a) shows contours of thrust coefficient vs. Strouhal number and maximum instantaneous angle of attack from Read *et al.* (2003). The maximum angle of attack is the largest angle of attack reached by the airfoil during a full motion cycle and is a result of both pitching and heaving. It can differ substantially from the pitching angle at any given time. In these experiments, the airfoil is pitching about its one-third-chord position ($p/c = 1/3$) with a heave-to-chord ratio of 0.75 and a Reynolds number equal to 40,000. Both pitching and heaving motions are sinusoidal with the pitching motion leading the heaving motion by 90° . In general, thrust increases with Strouhal number and with maximum an-

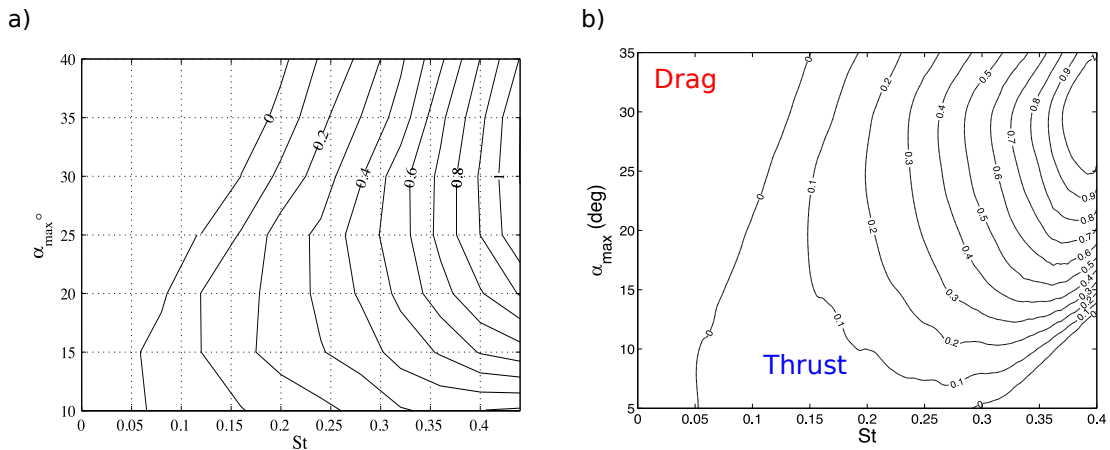


Figure 2.6: Active Heave, Active Pitch (a) Contours of thrust coefficient vs. St and α_{max} , $Re = 40,000$, $p/c = 0.33$, and $h_0/c = 0.75$ (Read *et al.*, 2003) (reprinted with permission from Elsevier). (b) Contours of thrust coefficient vs. St and α_{max} from current experiments. $Re = 15,000$, $p/c = 0.33$, and $h_0/c = 0.25$.

gle of attack up to about 30° . However, performance begins to degrade as the angle of attack is increased further. This is particularly evident in the position of the zero contour, which indicates the transition between motions which produce thrust and those that produce drag. At high values of α_{max} , a larger value of Strouhal number is needed to produce thrust. While our facility does not match the heave-to-chord ratio and Reynolds number used in the MIT experiments, the contours of thrust coefficient that we obtain (figure 2.6b) are broadly similar in behavior.

Figure 2.7(a) shows contours of propulsive efficiency for the same experiments (Read *et al.*, 2003). The highest efficiency of 71.5% occurs for a Strouhal number of 0.16 and a maximum angle of attack of 15° . Unfortunately, the thrust coefficient for this operating condition is relatively low at 0.18. Fortunately, however, there is a broad range of Strouhal numbers and angles of attack where the thrust coefficient is relatively high and the efficiency, though not the maximum, is still reasonable. Results from the Cornell CPFDF facility again show

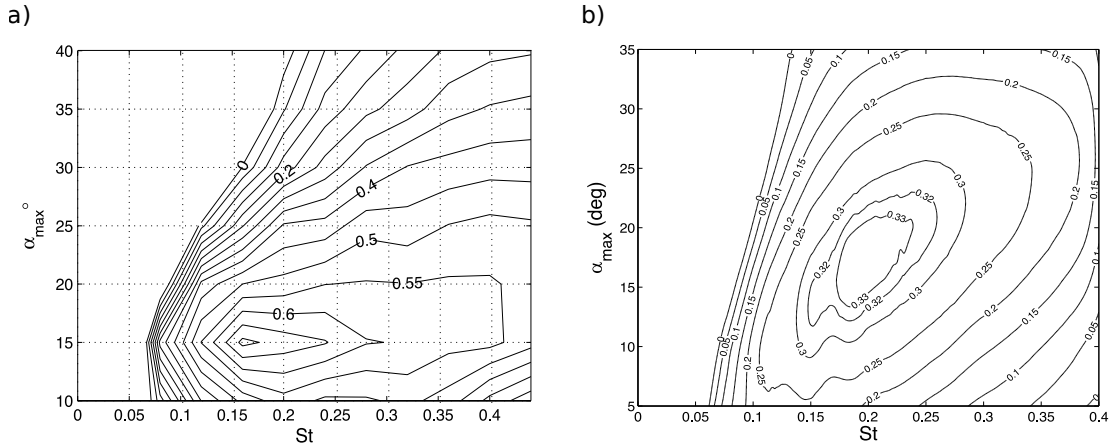


Figure 2.7: (a) Contours of propulsive efficiency vs. St and α_{max} , $Re = 40,000$, $p/c = 0.33$, and $h_0/c = 0.75$ (Read *et al.*, 2003) (reprinted with permission from Elsevier). (b) Contours of propulsive efficiency vs. St and α_{max} from current experiments. $Re = 15,000$, $p/c = 0.33$, and $h_0/c = 0.25$.

broadly similar results (figure 2.7b), although the peak efficiency occurs in a broader region and is lower than the MIT experiments. These differences are attributable to the lower Reynolds number and to the lower heaving amplitude used in our study.

To observe the effect of the heave-to-chord ratio on the thrust coefficient and propulsive efficiency, some experiments were conducted using a NACA 0012 airfoil of 5-cm chord. This smaller airfoil allowed us to achieve larger normalized heaving amplitudes within the confines of our test section. Figure 2.8 shows a comparison between experiments from Read *et al.* (2003) and those conducted in our facility for a Strouhal number of 0.30, representing a vertical slice through the contour plots discussed earlier. In this case, we match the heave-to-chord ratio of 0.75, and the only difference between the experiments is the Reynolds number: 40,000 for the MIT experiments and 14,000 in our facility. For both the thrust coefficient and propulsive efficiency, agreement is good, despite the Reynolds number difference.

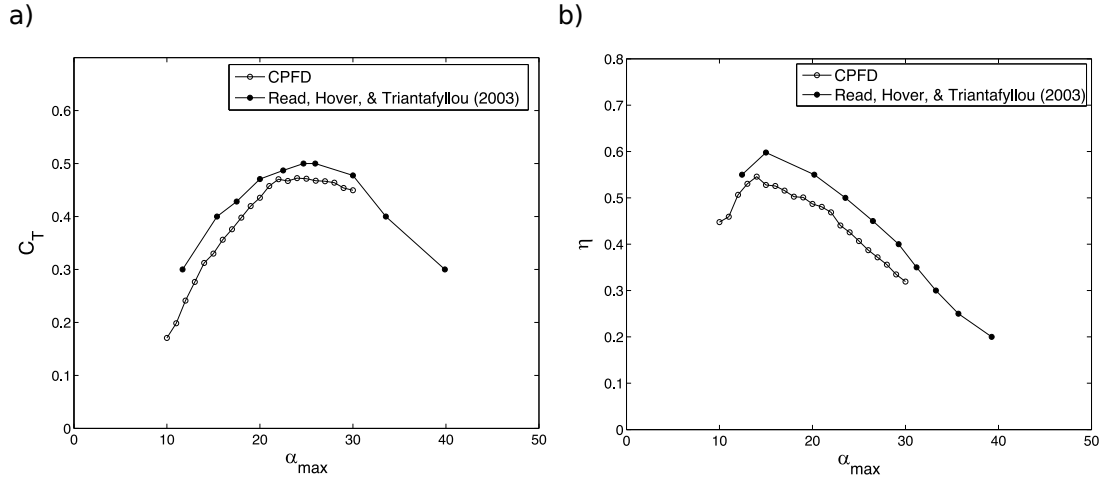


Figure 2.8: Thrust coefficient vs. maximum angle of attack (a) and propulsive efficiency vs. maximum angle of attack (b) from Read *et al.* (2003) and current experiments for $St = 0.30$ and $h_0/c = 0.75$.

2.4 [Active Heave]-[Passive Pitch]: Thrust and Efficiency

The principal aim of this study is to evaluate the performance of an actively heaving, passively pitching airfoil through a cyber-physical fluid dynamics technique. This means that we use our force-feedback system to simulate the presence of a torsion spring at the pivot point on the airfoil, as shown in figure 2.9.

The equation of motion governing the rotation of the airfoil is given by the following:

$$I\ddot{\theta} = M_f - \kappa\theta + F_x r \sin \theta - F_y r \cos \theta - 4\pi^2 f^2 h_0 m r \cos \theta \cos(2\pi f t) \quad (2.10)$$

In this equation, I is the moment of inertia of the airfoil about its pivot location, θ is the angular position of the airfoil, M_f is the fluid moment measured

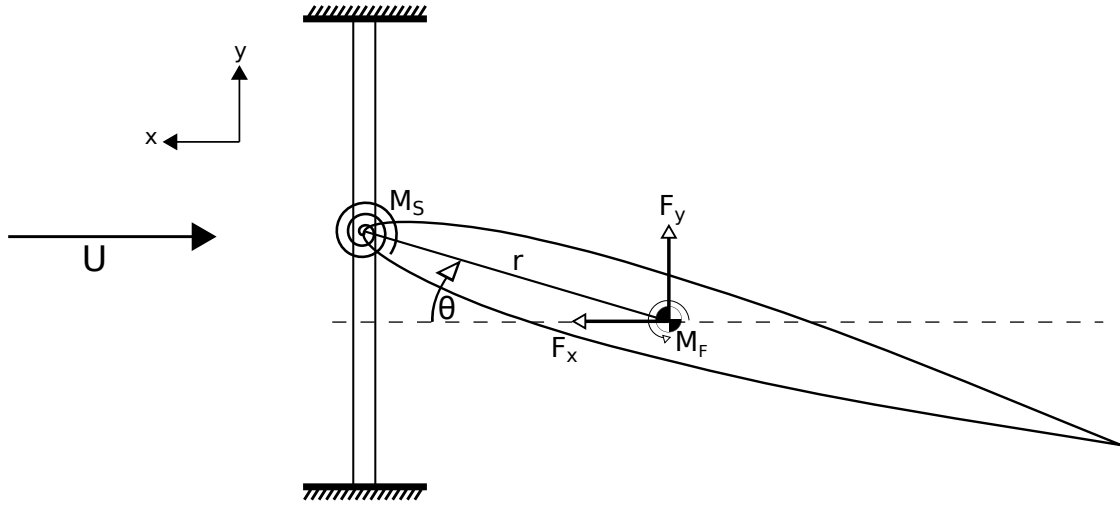


Figure 2.9: Free-body diagram showing the forces and moments acting on the airfoil. In this case, the pivot point is located at the leading edge.

by the force/torque sensor at the center of mass, κ is the spring stiffness, F_x is the force in the streamwise direction, F_y is the force in the transverse direction, f is the heaving frequency, h_0 is the heaving amplitude, m is the virtual airfoil mass, r is the distance from the airfoil center of mass to the pivot point, and t is time.

From left to right on the right-hand side of equation 2.10, the terms represent the fluid moment exerted by the center of mass, the moment from the torsion spring, the moments created at the pivot location by the x - and y -forces, and the inertial moment, which causes the airfoil to rotate whenever its center of mass is not collocated with the pivot point.

In figure 2.10, we show the thrust coefficient as a function of the frequency ratio, f/f_n , for various pivot points along the airfoil chord. The frequency ratio is varied by changing the natural frequency, so that smaller values of f/f_n correspond to a stiffer spring and larger values to a weaker spring. For $f/f_n = 0$, the spring is infinitely stiff, and the system behaves as if it is undergoing a purely

heaving motion. Immediately obvious from this plot is the strong resonance effect that occurs near $f/f_n = 1$, an effect that appears to become more pronounced as the pivot is moved closer to the leading edge. Interestingly, we observe both a positive and a negative resonance. For pivot locations located forward of the airfoil's center of mass, such as at or in front of its leading edge, the airfoil produces increasingly large amounts of thrust as the frequency ratio approaches resonance. For pivots downstream of the center of mass, the airfoil actually acts as a brake, producing a very large amount of drag, especially when pivoted near the trailing edge. If the spring is made very weak, such as for frequency ratios greater than about 1.5, then the airfoil becomes a very ineffective propulsor, producing little thrust.

Figure 2.11(a) shows further pivot locations located upstream of the airfoil leading edge. The highest thrust coefficient that we observed was produced when the airfoil was pivoted about a point two chord-lengths upstream ($p/c = -2.00$). For $f/f_n = 0.85$, the thrust coefficient is 2.40. Furthermore, the region in which high thrust coefficients are obtainable is relatively broad, with comparable performance available for a pivot one chord-length upstream of the leading edge as well ($p/c = -1.00$). Useful thrust is still produced for pivots ranging from $p/c = -5.00$ to $p/c = 0.25$. Figure 2.11 shows in schematic form the shape of the response curve for the best performing pivots. When actuated in heave only, the airfoil produces a thrust coefficient equal to 0.267. Consequently, with the proper selection of pivot point, it is possible to obtain roughly a factor of ten increase in thrust over heaving alone. This “magnification factor” is shown in schematic form in figure 2.11(b).

If we select the resonance peaks for each pivot location, we obtain the plot in

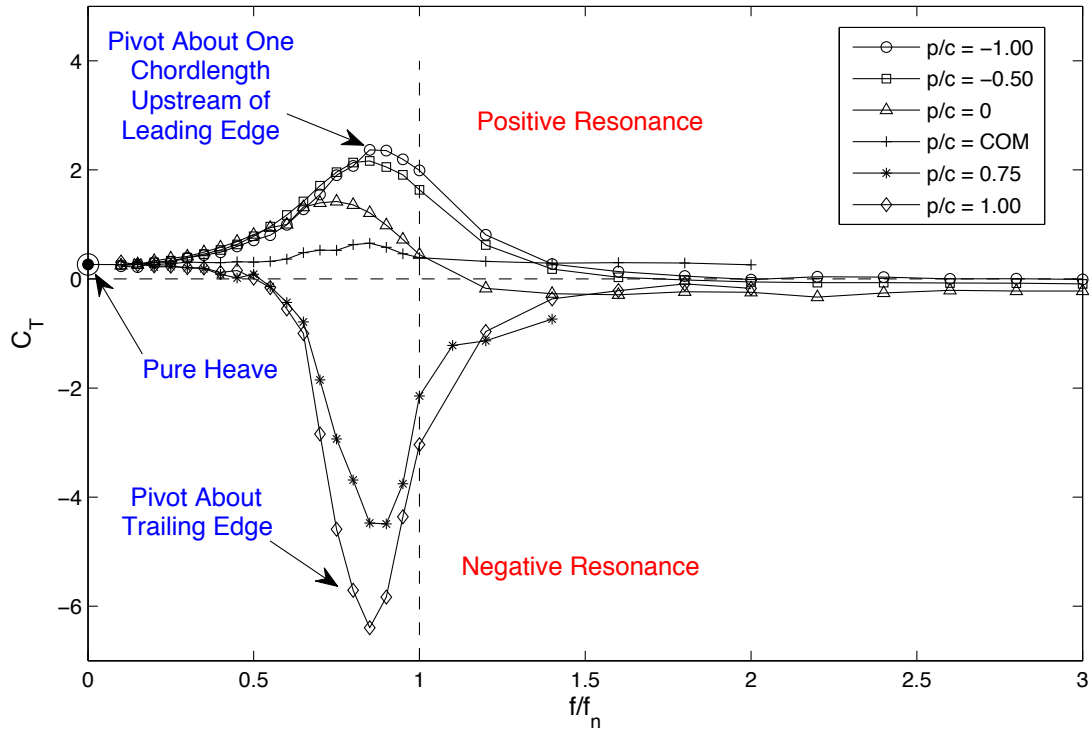


Figure 2.10: Thrust coefficient vs. frequency ratio for various pivot points. When the airfoil is pivoted about a point upstream of its center of mass, the thrust coefficient is magnified as the frequency ratio f/f_n approaches resonance. Conversely, if the pivot location is downstream of the center of mass, a negative, drag-producing resonance occurs.

figure 2.12, showing the peak thrust or drag produced by the airfoil as a function of the pivot location. Upstream of the center of mass, the airfoil produces thrust, and downstream of the center of mass, it produces drag. The best thrust performance is obtained for pivots forward of the leading edge, where there is a large, relatively flat region in which performance remains close to the maximum. As the pivot is located behind the center of mass, the airfoil produces increasing amounts of drag, achieving its maximum braking force for a pivot just downstream of the trailing edge ($p/c = 1.1$). The maximum drag coefficient for this pivot location, $C_D = 6.38$ is approximately twice the drag produced by a stationary NACA 0012 airfoil at an angle of attack of 90° , indicating a substan-

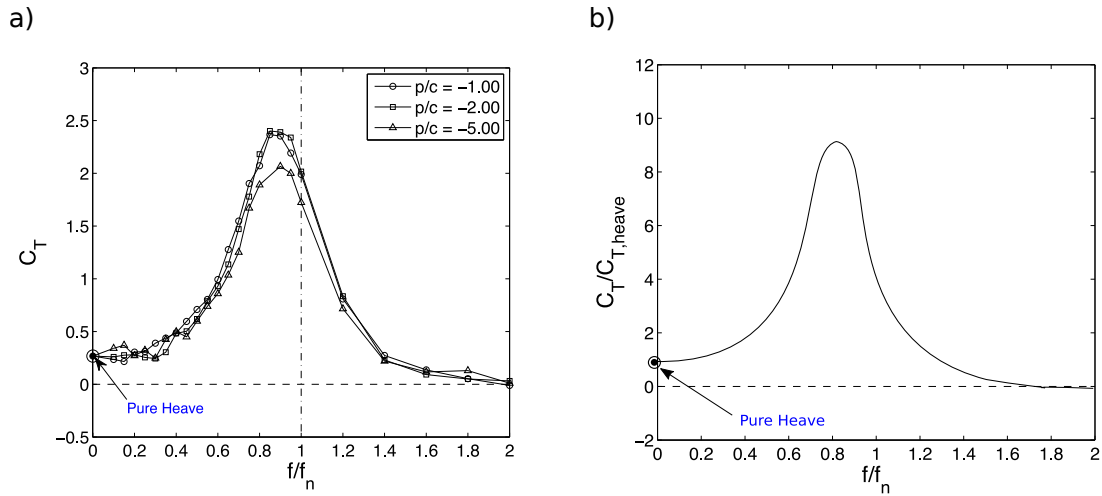


Figure 2.11: (a) Thrust coefficient vs. frequency ratio for pivot locations upstream of the airfoil leading edge. (b) Schematic based on data from $p/c = -1.00$ illustrating the increase in thrust coefficient that can be achieved over pure heaving. The maximum “magnification factor” achieved for this set of parameters is approximately 10. The data presented in this schematic are representative of the airfoil thrust production for pivots ranging from $p/c = -0.50$ to $p/c = -5.00$.

tial drag increase in the dynamic case. Finally, the transition between thrust and drag occurs very abruptly as the pivot moves behind the airfoil’s center of mass.

We have shown that the addition of passive pitching dynamics can achieve remarkable gains in thrust over airfoils which are only allowed to move in the heaving direction. However, the question of how well the airfoil performs compared to a system in which both heave and pitch are actively controlled naturally arises. As discussed in §2.2, a fully active system allows independent control over the amplitudes of both heave and pitch and over the phase difference between those motions. In order to evaluate this question, we conducted a series of experiments in which the pitching amplitude and phase were systematically varied for two pivot locations which produce thrust. The resulting contour plots of thrust coefficient (figure 2.13) show optimal performance is achieved for pitching amplitudes near $20 - 25^\circ$ and phase angles of $200 - 220^\circ$.

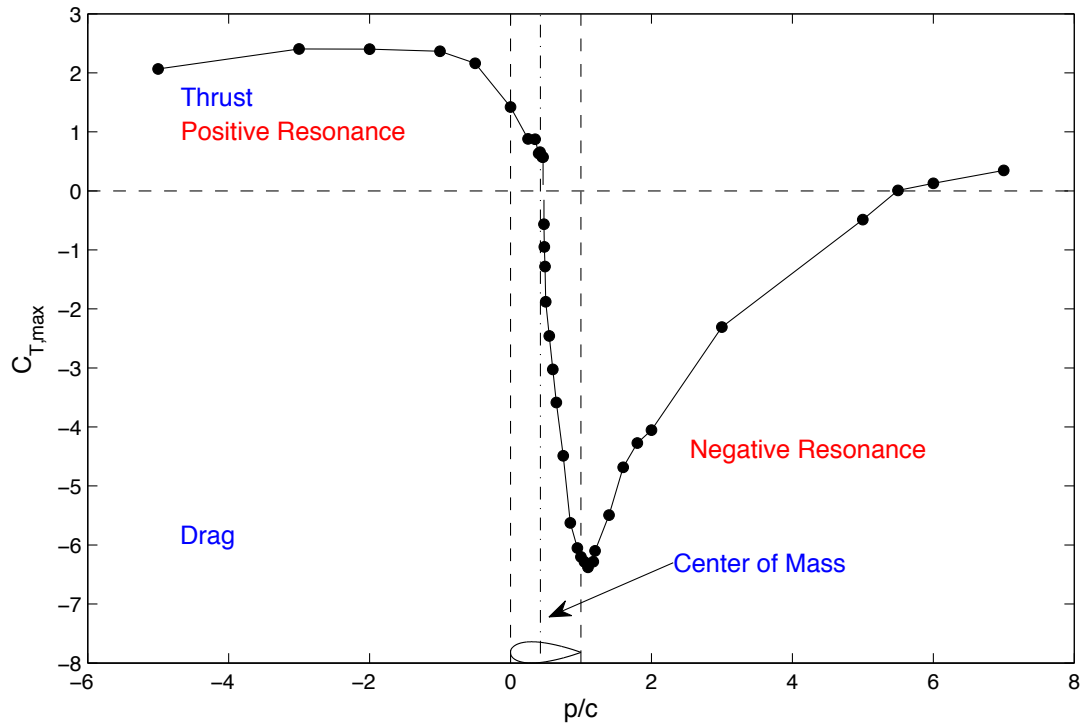


Figure 2.12: Maximum thrust coefficient vs. pivot location. Pivot points located forward of the airfoil's center of mass produce thrust, while those located downstream of the center of mass produce drag.

(Phase angles in this range indicate that the pitching motion is leading the heaving motion by a bit more than 1/4 of a cycle.) The red bull's eyes indicate the pitching amplitude and phase at which the passively pitching airfoil operates when it produces peak performance. In both cases, the passive system operates near the optimum point for thrust production. Consequently, we can take advantage of the performance benefits made possible by using both pitch and heave while only controlling heave with a single actuator.

Many studies (for example, (Read *et al.*, 2003)) have shown that it is not possible to simultaneously operate at peak thrust and at peak efficiency. When operating with the motion parameters that deliver maximum thrust coefficient, the propulsive efficiency is typically lower than that achievable when the thrust

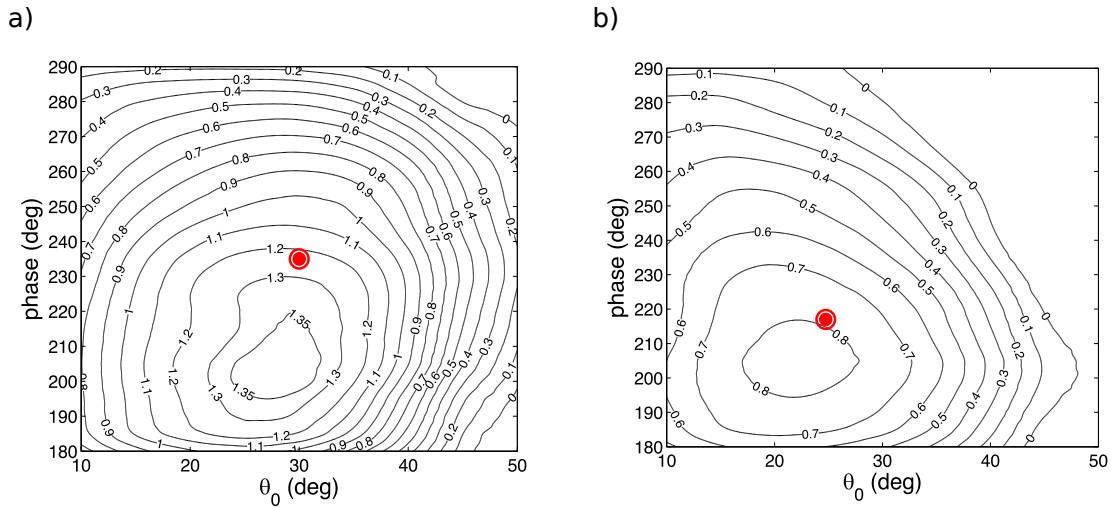


Figure 2.13: (a) Contours of thrust coefficient as a function of the pitching amplitude and pitching phase for the airfoil with a pivot point located at the leading edge ($p/c = 0$). (b) Contours of thrust coefficient as a function of the pitching amplitude and pitching phase for the airfoil with a pivot point located at its quarter-chord ($p/c = 0.25$). In both (a) and (b), the red circle indicates the best performance achieved when pitch is implemented passively.

performance is not optimized. Similarly in these experiments, as shown in figure 2.14, efficiency is best at pivot locations closer to the center of mass, where thrust production is reduced. As the pivot point moves further forward on the airfoil and in front of the leading edge, thrust increases but efficiency declines.

Fortunately, however, operating near the resonance point for a given pivot has very little effect on the propulsive efficiency. Figure 2.14(b) shows the efficiency overlaid with the thrust response curve for $p/c = -1.00$, a point located one chord-length ahead of the leading edge. The efficiency curve is quite flat and changes little even as the thrust coefficient increases dramatically near the resonance condition.

Attempts to model the performance of an oscillating airfoil include the early studies of Theodorsen (1935), who was interested in airfoil oscillations caused

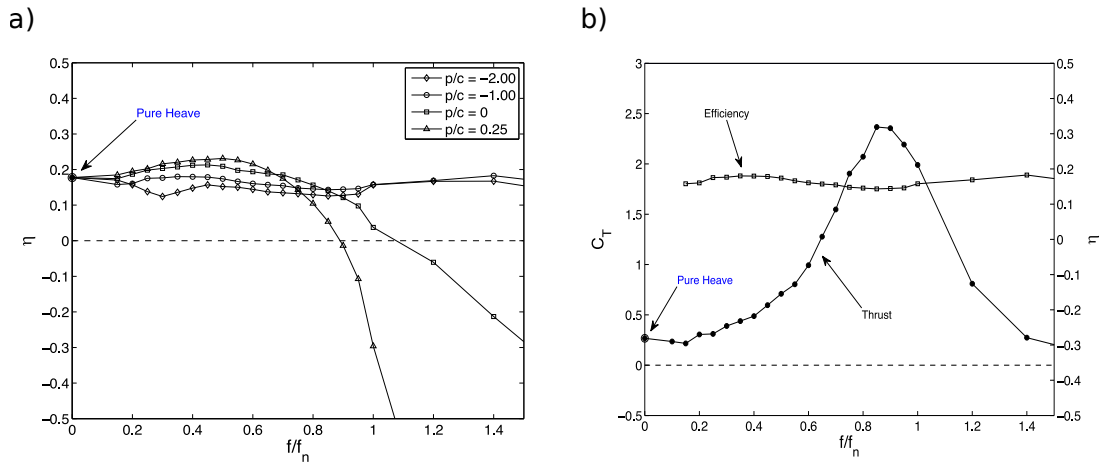


Figure 2.14: (a) Propulsive efficiency vs. frequency ratio for various pivot locations. (b) Propulsive efficiency and thrust coefficient for a pivot point located one chord-length ahead of the leading edge of the airfoil ($p/c = -1.00$), showing that the efficiency does not decrease significantly near the resonance point.

by aerodynamic flutter. His theory provides a completely analytical means of computing the lift force and moment on an airfoil moving in pitch and heave. The expressions he obtained using velocity potentials were also derived separately by von Kármán & Sears (1938) using momentum conservation. Garrick (1936) built on the theory of Theodorsen to compute the thrust force on the airfoil, using the suction force applied at the airfoil's leading edge and the quasi-steady contribution of the lift component in the thrust direction. More recently, Fernandez-Feria (2016) has recomputed the thrust force, but this time based on the entire vorticity distribution. The newly derived expressions correct some non-physical behavior observed with results from Garrick (1936) and also provide better agreement with experiments and computations for pitching airfoils.

The theory requires a complete description of the parameters defining the motion of the airfoil. The input variables include the heaving and pitching amplitudes, the phase difference between heaving and pitching, and the pivot location along the airfoil chord. Outputs available are the thrust and lift forces

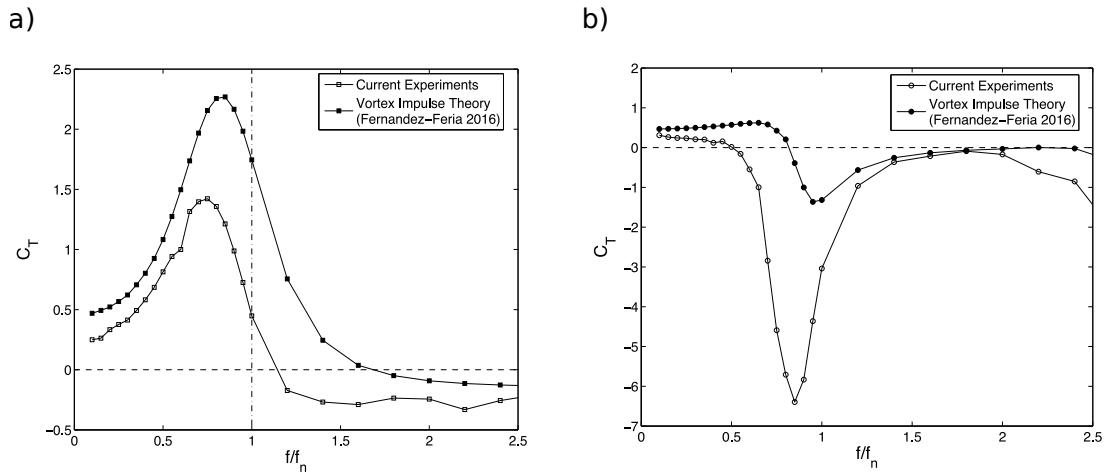


Figure 2.15: Thrust coefficient vs. frequency ratio from current experiments and predicted by the vortex impulse theory of Fernandez-Feria (2016) for (a) $p/c = 0$ and (b) $p/c = 1.00$.

acting on the airfoil along with the pitching moment. In order to evaluate the applicability of the theory to the motions observed in this study, we computed the thrust coefficient predicted by the theory using the pitching amplitude and phase difference measured by our experiments. Figure 2.15 shows the predicted thrust coefficient as a function of frequency ratio for two pivot points: the leading edge in (a), and the trailing edge in (b). Examination of these results shows that the theory does not do particularly well with capturing the quantitative values of the thrust coefficient. This may be expected, given the large amplitudes in both pitch and heave and low Reynolds number in this experiment. However, the theory is qualitatively largely correct. It properly shows thrust production when the airfoil pivots about its leading edge and drag when it is pivoted about its trailing edge.

A significant disadvantage of using the vortex impulse theory to predict performance in this manner is that the pitching amplitude and phase are unknown prior to running an experiment. These inputs are required for the theory to

predict the forces and moments on the airfoil. One way to obtain these parameters is to run an experiment and measure them. Alternatively, we can couple the vortex impulse theory with the equation of motion governing the pitching axis in order to make *a priori* predictions of the airfoil performance. In this way, predictions can be made without running a physical experiment at all.

As written, the equation of motion (equation 2.10) has five unknowns: the pitching amplitude, θ , pitching phase, ϕ , the two fluid forces, F_x and F_y , and the fluid moment, M_f . The other parameters, including the spring stiffness, κ , the heaving amplitude, h_0 , the heaving frequency, f , the mass m , and the pivot location, r , are known. In our solution technique, we sweep over a reasonable parameter space for the pitching amplitude and phase and use the recent theory of Fernandez-Feria (2016) to provide the fluid forces and moments. The pitching amplitude and phase which best satisfy the equation of motion are then taken as the predictions for a given experiment. Figure 2.16 shows experimental data with *a priori* predictions using this method. Quantitatively, the agreement remains poor as expected. However, the qualitative behavior of the predictions correctly shows the presence of the resonance point and its corresponding increase in thrust coefficient. Results from the theory also have other important uses, as discussed in §2.5.

All of the results presented to this point were collected for an airfoil operating with a reduced frequency, $k = fc/U$, equal to 0.50. In order to investigate the effect of the reduced frequency on the thrust coefficient and the propulsive efficiency, the reduced frequency was varied from 0.25 to 0.75. Results from these experiments, conducted with the pivot point at the leading edge, are shown in figure 2.17. As reduced frequency is increased, the thrust coefficient increases

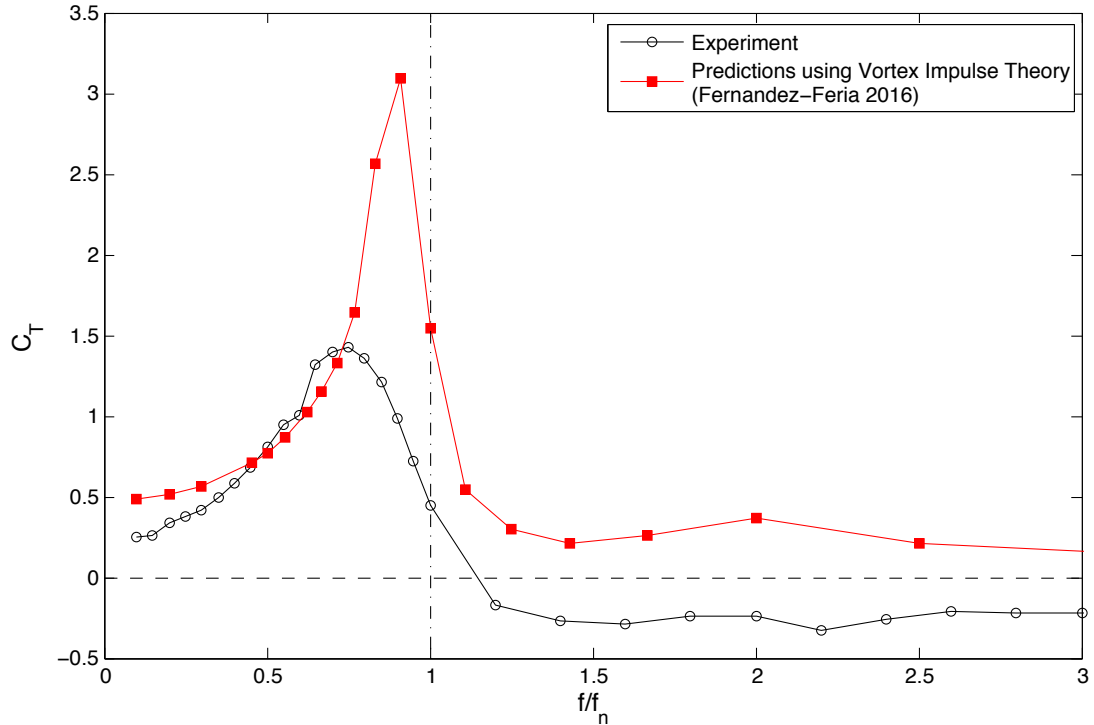


Figure 2.16: Thrust coefficient vs. frequency ratio from current experiments and predicted by the theory of Fernandez-Feria (2016) for $p/c = 0$. In this case, the predictions do not rely on measured values of the pitching amplitude and phase. They are predicted using the pitching equation of motion and the vortex impulse theory.

quite dramatically. Simultaneously, the propulsive efficiency decreases.

2.5 Passive Pitching: Motion Dynamics

We have shown that it is possible to obtain excellent performance from an actively heaving, passively pitching airfoil. In this section we discuss the operational characteristics that are responsible for this performance. In figure 2.18, we show the pitching amplitude selected by the system when it is passively pitching as a function of the frequency ratio. The four plots include curves from different ranges of pivot location. The upper two panels represent motions which

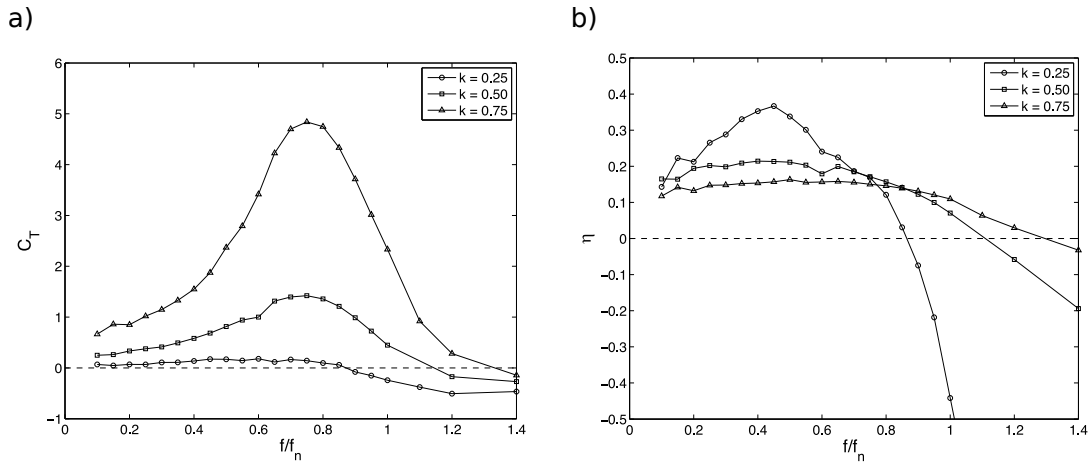


Figure 2.17: (a) Thrust coefficient and (b) propulsive efficiency vs. frequency ratio for a heaving airfoil which is also pitching about its leading edge with various values of reduced frequency. Higher reduced frequencies are associated with greater thrust production but lower efficiency.

produce thrust, and the lower two panels motions which produce drag.

Several features are apparent. First, the pitching amplitude also exhibits a resonance effect, similar to that seen for the thrust coefficient. The frequency ratio at which the maximum pitching amplitude occurs, however, is higher than that for resonance of the thrust coefficient. Typically, the maximum thrust coefficient occurs for a frequency ratio near 0.85 for thrust-producing motions, whereas the point of maximum pitching amplitude follows later, at about $f/f_n = 1$. Secondly, the best thrust performance occurs for moderate amplitudes of pitch. For example, $p/c = -1.00$ and $p/c = -2.00$ produce excellent thrust and have pitching amplitudes near 20° . Motion profiles in which the pitching amplitude is larger do not fare as well, generally producing less thrust. However, it also apparent that having the correct pitching amplitude is insufficient for guaranteeing good thrust performance—pivoting about the airfoil’s center of mass results in approximately the same pitching amplitude as $p/c = -1.00$ but produces relatively little thrust (see figure 2.12).

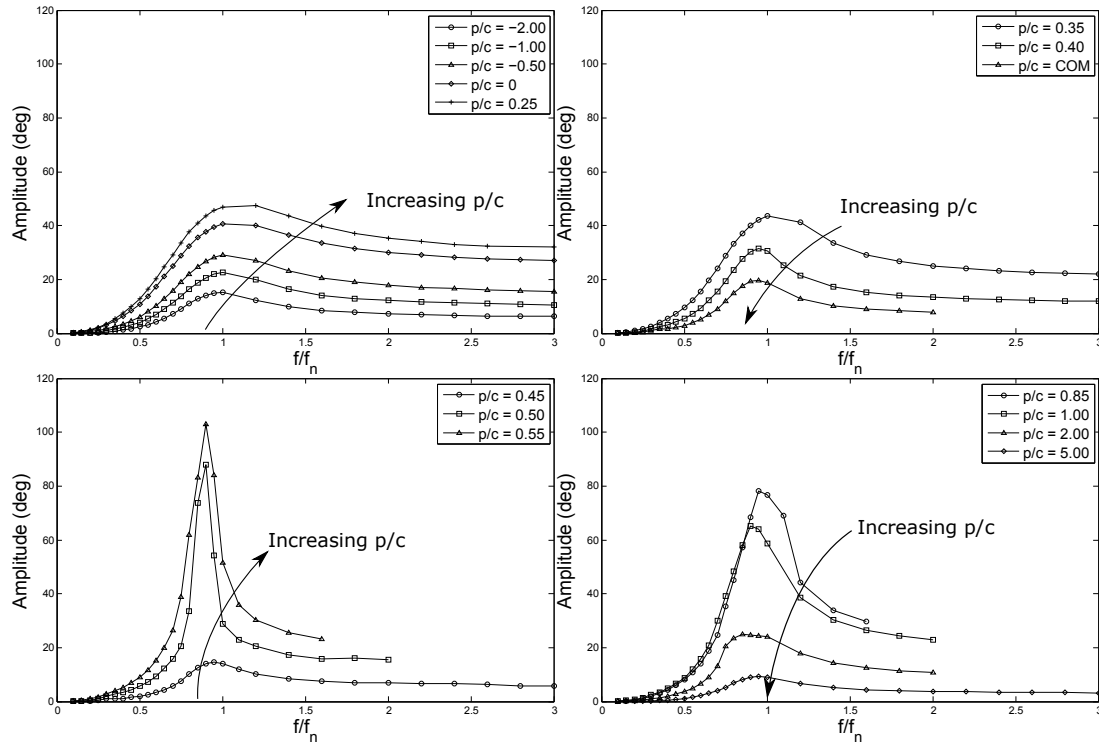


Figure 2.18: Pitching amplitude, θ_0 , as a function of frequency ratio and pivot location for a passively pitching airfoil. Resonance peaks in the pitching amplitude occur as the frequency ratio f/f_n approaches 1.

For the cases which produce significant drag, the pitching amplitude becomes very large, peaking at more than 100° for $p/c = 0.55$. The amplitude gradually decreases for pivots located downstream of that point, even as the amount of drag produced increases. For pivots far downstream, the airfoil transitions from producing drag to producing thrust.

Predictions of the pitching amplitude derived from the vortex impulse theory of Fernandez-Feria (2016) using the method described in §2.4 are shown in figure 2.19. In contrast to its relatively poor quantitative predictions of thrust coefficient, the theory does remarkably well with predictions of the pitching amplitude. In this plot, we restrict the phase between pitching and heaving to $0 - 180^\circ$. Consequently, because $-\theta_0 \cos(2\pi ft - \phi) = \theta_0 \cos(2\pi ft - \phi + \pi)$, we

plot a negative pitch amplitude if the phase angle is greater than 180° . Phases greater than 180° indicate that the pitching motion leads the heaving motion, and phases less than 180° indicate the reverse: the heaving motion leads the pitching motion. One may note that the transition point between these configurations occurs near the airfoil's center of mass, which also corresponds to the transition between thrust- and drag-producing pivot locations. Clearly, then, the phase angle is important for optimizing the thrust produced by the airfoil.

Also apparent from figure 2.19 is the decrease in pitching amplitude θ_0 that occurs as the pivot location moves further from the center of mass in either direction. This can be understood from equation 2.10. As r increases, the moment of inertia I increases with r^2 by the parallel-axis theorem. Similarly, to deliver the same frequency ratio, the spring stiffness scales with I (equation 2.3), therefore also an r^2 relationship. Both of those terms resist the rotation of the airfoil. In contrast, the other terms in the equation, which attempt to rotate the airfoil, all scale with r . Consequently, the terms resisting motion dominate as r increases, and pitching is suppressed.

Figure 2.20 shows the phase angle ϕ as a function of frequency ratio for several pivot locations. The curves at the top of the plot all produce thrust and have phase angles between 180° and 360° , indicating that the pitching motion leads the heaving motion. Peak thrust is produced when the phase angle is approximately 230° . The lower curve shows the phase angle for a pivot located at the trailing edge of the airfoil, which is near the position that produces maximum drag. For high drag, the phase angles are all less than 180° , indicating that the heaving motion leads the pitching motion. Between these extremes, pivot points near the airfoil's center of mass produce a phase angle that causes the

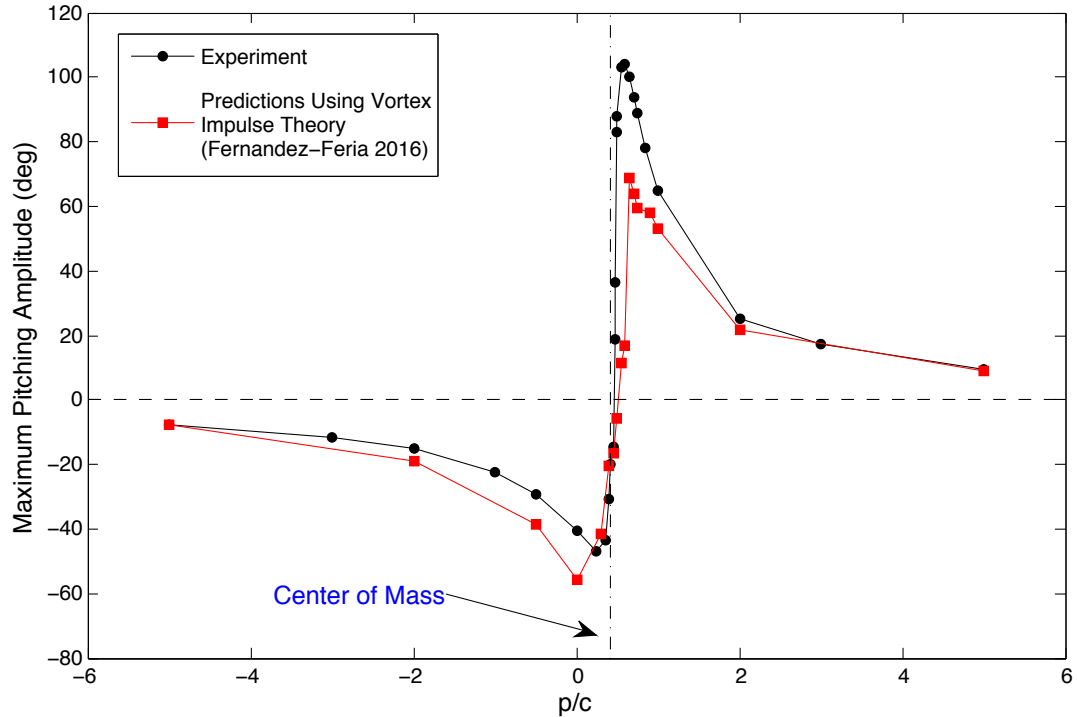


Figure 2.19: Maximum pitching amplitude as a function of pivot location from current experiments and predicted by vortex impulse theory (Fernandez-Feria, 2016). In this plot, the amplitude is plotted as negative if the phase between the pitching and heaving motions is between $180 - 360^\circ$ and positive if it is between $0 - 180^\circ$.

pitching motion to be out-of-phase with the heaving motion and consequently generates little propulsive force.

As the frequency ratio increases, the forces produced by the airfoil drop to near zero regardless of the pivot point (figure 2.10). When this happens, the spring becomes very weak, and the pitching motion becomes either in-phase with the heave (for pivot points located forward of the center of mass) or out-of-phase with the heave (for pivot points located behind the center of mass).

To see how the phase difference influences the behavior of the airfoil, we can examine plots of the airfoil trajectory synchronized with other data. In figure 2.22, we show the “trajectory plot” of the airfoil when pivoting about its leading

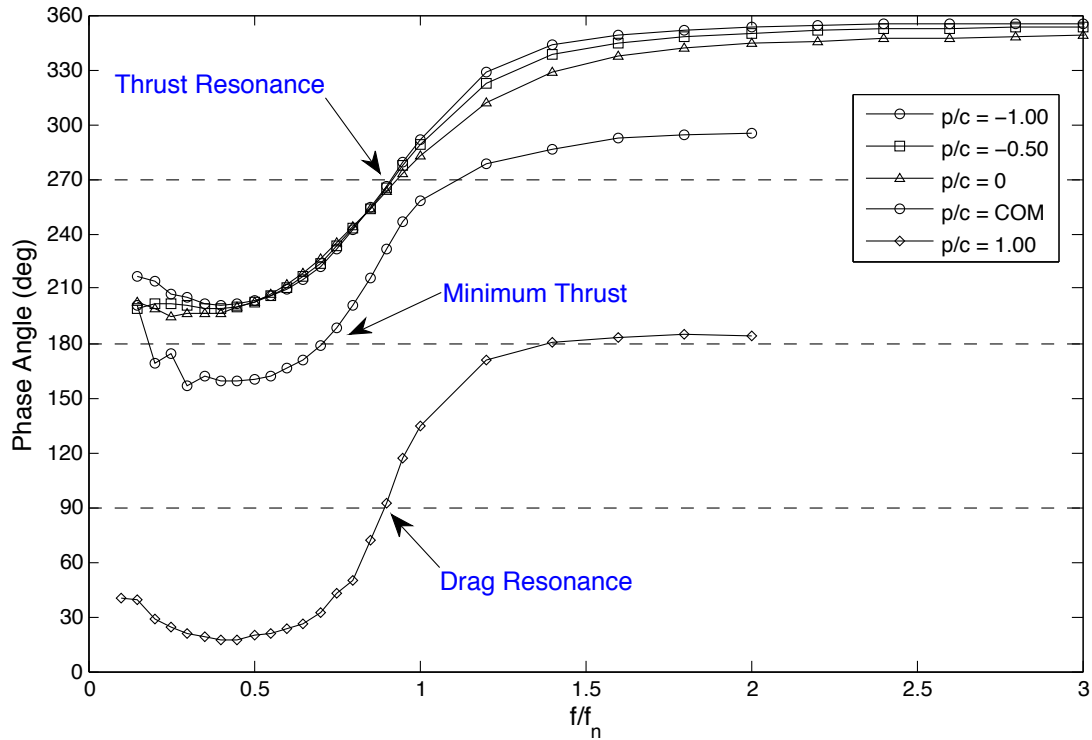


Figure 2.20: Phase angle as a function of frequency ratio for several pivot locations. Motions that produce thrust have phase angles near 270° at resonance, indicating that pitching leads the heaving motion. Motions that produce drag have the opposite relationship, with the heaving motion leading the pitching motion at a phase angle near 90° .

edge in the top panel, the thrust coefficient in the middle panel, and the angle of attack in the bottom panel. For comparison, we show the equivalent data for an airfoil pivoting about its trailing edge in figure 2.23. Such trajectory plots were found to be useful in understanding the vortex dynamics associated with a cylinder undergoing a forced vibration in the transverse direction, as shown by Williamson & Roshko (1988). Following the body as it moves through the surrounding undisturbed fluid is a much more natural and intuitive way to understand its behavior. Note that in these plots, the airfoil is shown at 70% scale relative to its trajectory.

The instantaneous angle of attack of the airfoil is determined by two con-

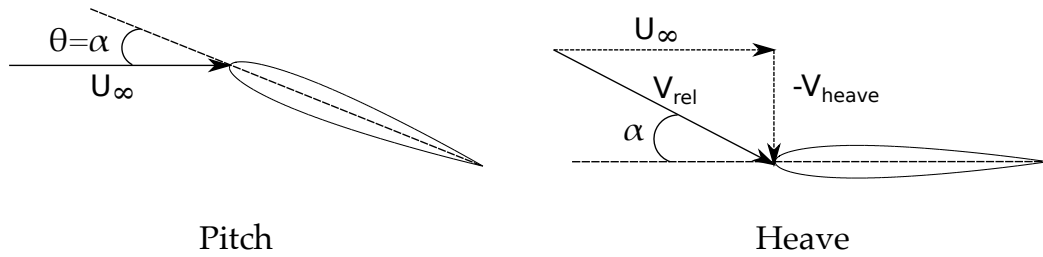


Figure 2.21: Schematic showing the angle of attack produced by pitching and heaving motions. For pure pitching, the angle of attack is equal to the pitching angle. For heaving, the heaving velocity adds vectorially to the incoming flow velocity. Consequently, the relative velocity seen by the airfoil has a nonzero angle of attack.

tributions. The first contribution is simply the angular position of the airfoil, designated by $\theta(t)$. For pure pitching, the pitch angle is equal to the angle of attack. The second contribution is from the heaving motion. The transverse velocity, $V_{heave}(t)$ of the airfoil is summed vectorially with the incoming free-stream flow. This combination has the effect of turning the relative velocity and creating an effective angle of attack. These two contributions are illustrated in figure 2.21.

Consequently, the total angle of attack for a pitching and heaving airfoil is given by equation 2.11.

$$\alpha(t) = \theta(t) + \arctan\left(\frac{-V_{heave}(t)}{U_\infty}\right) \quad (2.11)$$

In figure 2.22, when the airfoil pivots about its leading edge, thrust is produced over most of the cycle, and the instantaneous angle of attack remains moderate, with an amplitude of about 25° . This behavior stands in stark contrast to the very large angles of attack reached when the airfoil pivots about its trailing edge, shown in figure 2.23. In that case, the airfoil produces a very large

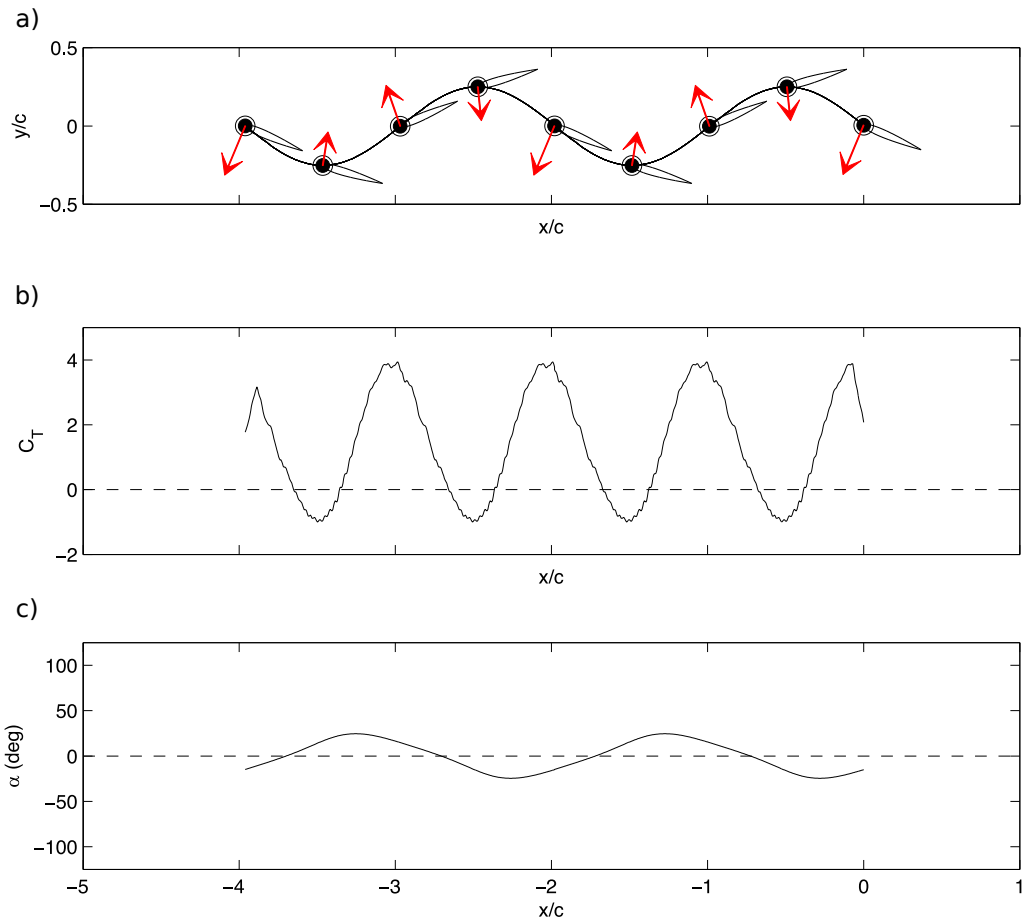


Figure 2.22: (a) Trajectory plot of an airfoil pivoting about its leading edge. Arrows indicate the direction and magnitude of the resultant force on the airfoil. (b) Thrust coefficient synchronized with the trajectory plot. (c) Instantaneous angle of attack, α (deg), synchronized with the trajectory plot.

amount of drag, and the angle of attack oscillates with an amplitude of 95° .

The difference in angle of attack can be explained through two effects. The first difference is simply the magnitude of the pitching amplitude, which is much higher in the case of an airfoil pivoting about its trailing edge. Even more important, however, is the phase relationship between pitching and heaving. Figure 2.24 shows the instantaneous angle of attack computed using a heave-

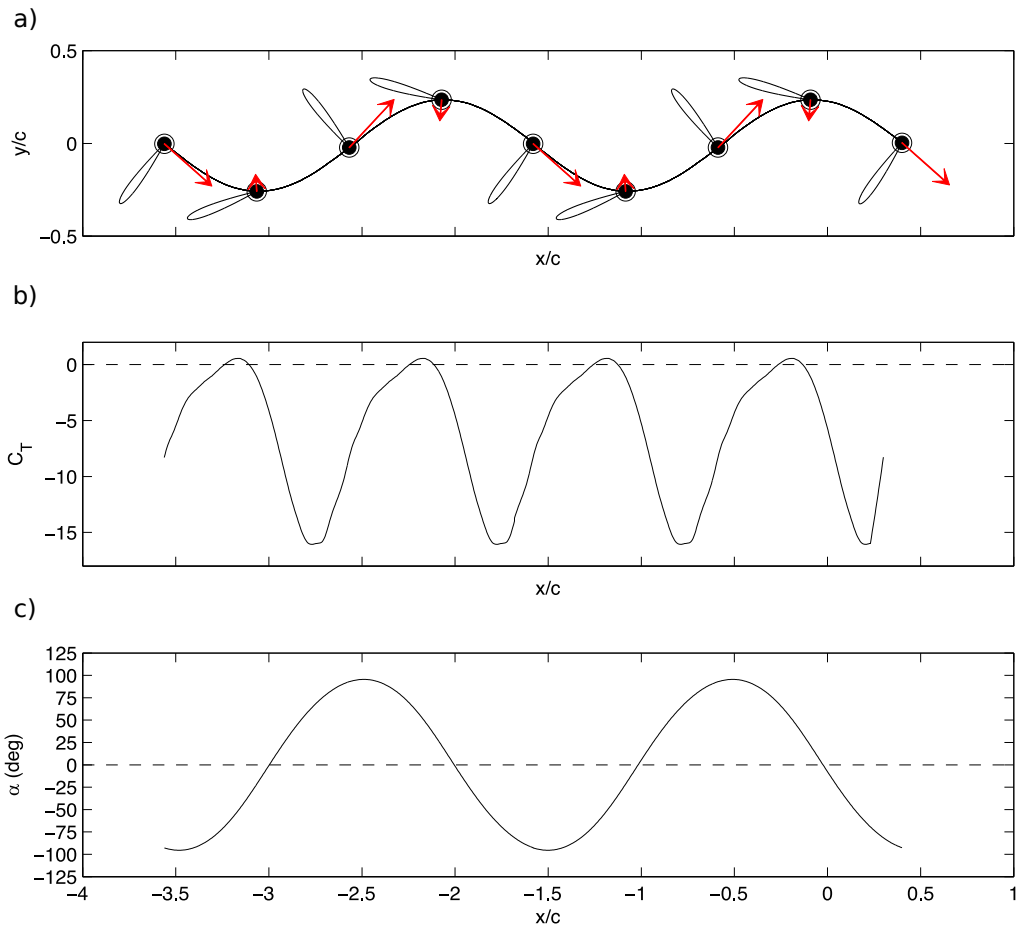


Figure 2.23: (a) Trajectory plot of an airfoil pivoting about its trailing edge. Arrows indicate the direction and magnitude of the resultant force on the airfoil. (b) Thrust coefficient synchronized with the trajectory plot. (c) Instantaneous angle of attack, α (deg), synchronized with the trajectory plot.

to-chord ratio of 0.25, a reduced frequency of 0.50, and a pitching amplitude of 25° . The two curves differ only in the phase angle of the pitching motion. For the black curve, pitching leads heaving by 90° . In contrast, for the red curve, heaving leads pitching by 90° . In the former case, the angle of attack has an amplitude of 13° . In the latter case, the angle of attack reaches values up to 63° , a region that places the airfoil deep into stall where drag forces increase

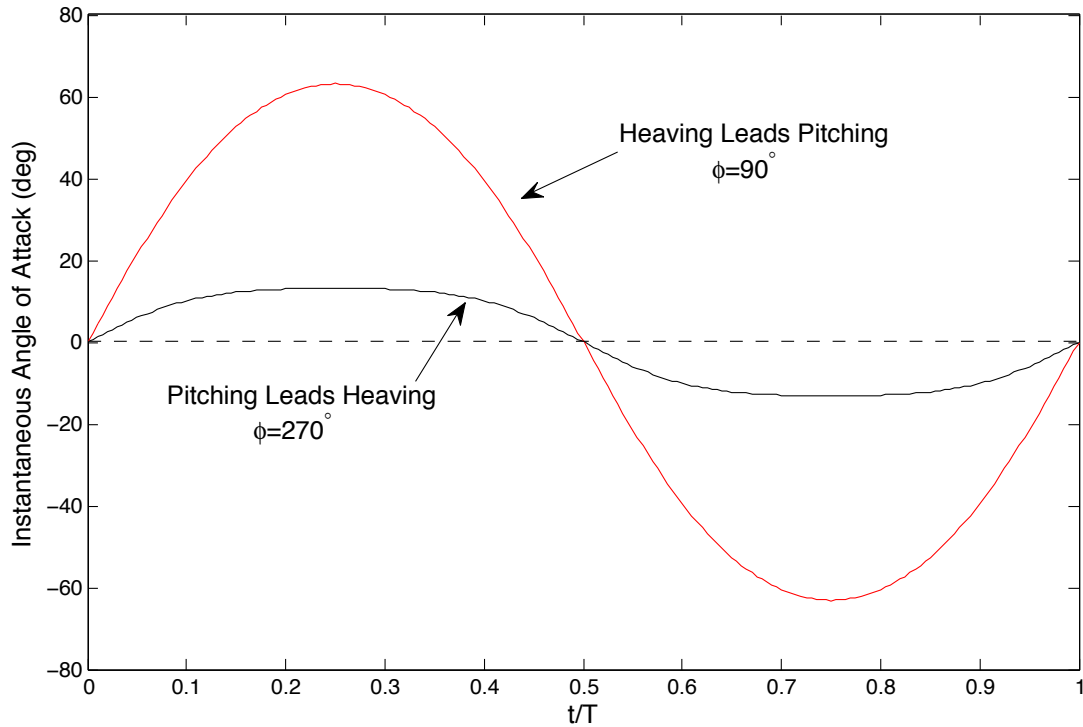


Figure 2.24: Example illustrating that the phase angle plays a critical role in determining the angle of attack. Both angle of attack curves were computed using the same heaving and pitching amplitudes. The only difference between them is the phase angle. When pitching leads the heaving motion ($\phi = 270^\circ$), the angle of attack is small, and thrust is produced. When heaving leads pitching ($\phi = 90^\circ$), the angle of attack is much larger, a condition that corresponds to drag production.

dramatically. Consequently, it is principally the change in phase angle that is responsible for the varying performance characteristics of different pivot locations.

Finally, we show in figure 2.25 two interesting examples of the behavior of the airfoil when the spring is made weak (small spring stiffness κ). In figure 2.25(a), an airfoil pivoting about its trailing edge experiences pitching oscillations which no longer share the same frequency of oscillation as the heaving motion. In this “long-period mode,” the period of the oscillations is much longer,

with the consequence that the airfoil spends a significant amount of time oriented at nearly 90° to the flow, a position in which the moment from the torsion spring is balanced by the drag produced by the incoming flow. Slight oscillations in pitch still occur, and the airfoil periodically changes from one side to the other when the spring manages to overcome the moment produced by the drag. If the spring is made significantly weaker, as in figure 2.25(b), then the airfoil simply turns broadside to the oncoming flow and remains there. Interestingly, the direction in which the airfoil turns can be controlled by the direction in which the airfoil initially heaves. It is therefore possible to bias the system either negatively or positively. It is reasonable to conclude, though, that neither of these special cases is of great practical utility, as they produce significant drag as a result of the amount of time the airfoil spends oriented roughly perpendicular to the flow. There may be some situations in which added drag is desirable, such as during a braking maneuver. In general though, operating in these regimes should be avoided.

The modes described above occur for pivot locations p/c between 1 and 2 and are present for the largest range of frequency ratios f/f_n when the airfoil is pivoted about its trailing edge. For $f/f_n = 2.4 - 3.5$, the long-period mode occurs. As the spring is made weaker, for $f/f_n = 3.5 - 6.4$, the airfoil turns to a position in which the drag produced by the incoming flow is balanced by the spring moment and remains in this position (offset pitching). This position is typically oriented at about 90° to the incoming flow. For $f/f_n > 6.4$, the airfoil turns completely around and oscillates with its trailing edge and pivot point pointing upstream.

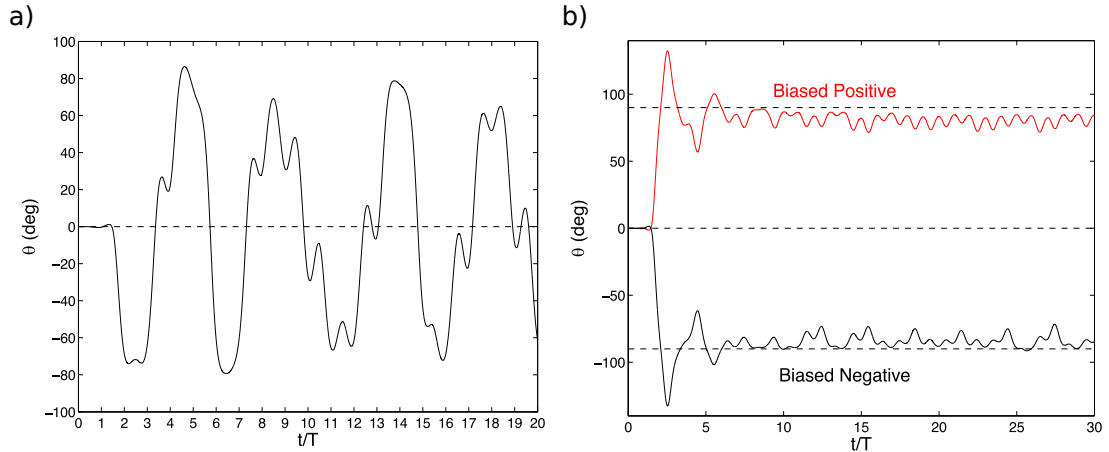


Figure 2.25: (a) Long-period pitching behavior of the airfoil pivoting about its trailing edge for $f/f_n = 2.6$. The period of the pitching oscillation is no longer matched to the heaving frequency. (b) Offset pitching behavior of the airfoil pivoting about its trailing edge for $f/f_n = 4.5$. The airfoil turns to a position such that its chord line is approximately perpendicular to the incoming flow.

2.6 Vortex Dynamics

In order to understand the source of the forces generated by the airfoil in various configurations, particle image velocimetry experiments were conducted, as described in §2.2. Figure 2.26 shows the instantaneous vorticity field and streamlines, and figure 2.27 shows a time-averaged vorticity field, both for the airfoil pivoting about its leading edge and operating at its maximum thrust coefficient ($f/f_n = 0.75$). Immediately obvious here is the classic reverse von Kármán vortex street, which is typical of bodies which produce thrust. The time-averaged PIV frame shows that the streamlines converge behind the airfoil, indicating a region of accelerated flow. This jet, whose presence is confirmed by examining the velocity profile downstream of the airfoil, is responsible for producing the thrust force measured in the experiments.

Perhaps more interesting are the operating conditions in which the airfoil

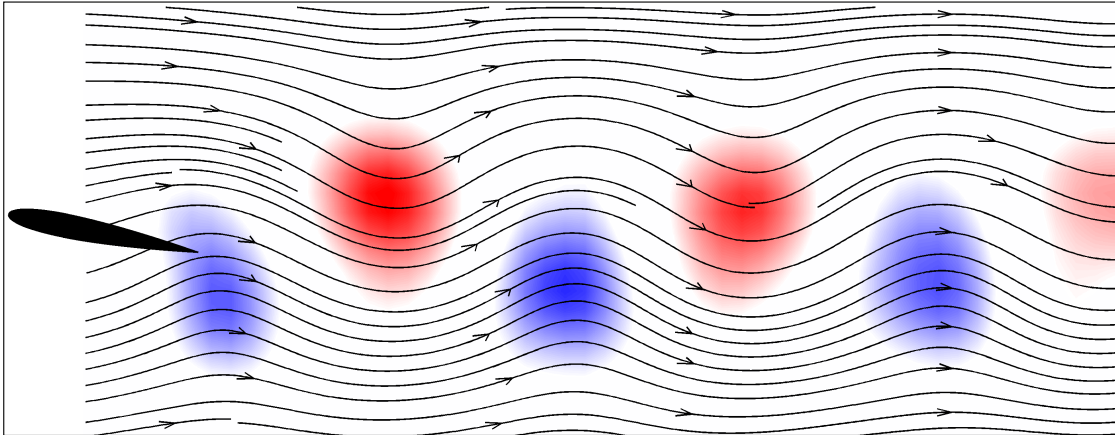


Figure 2.26: Instantaneous vorticity field for an airfoil pivoting about its leading edge ($p/c = 0$), showing the formation of an inverse von Kármán vortex street, which is typically associated with thrust.

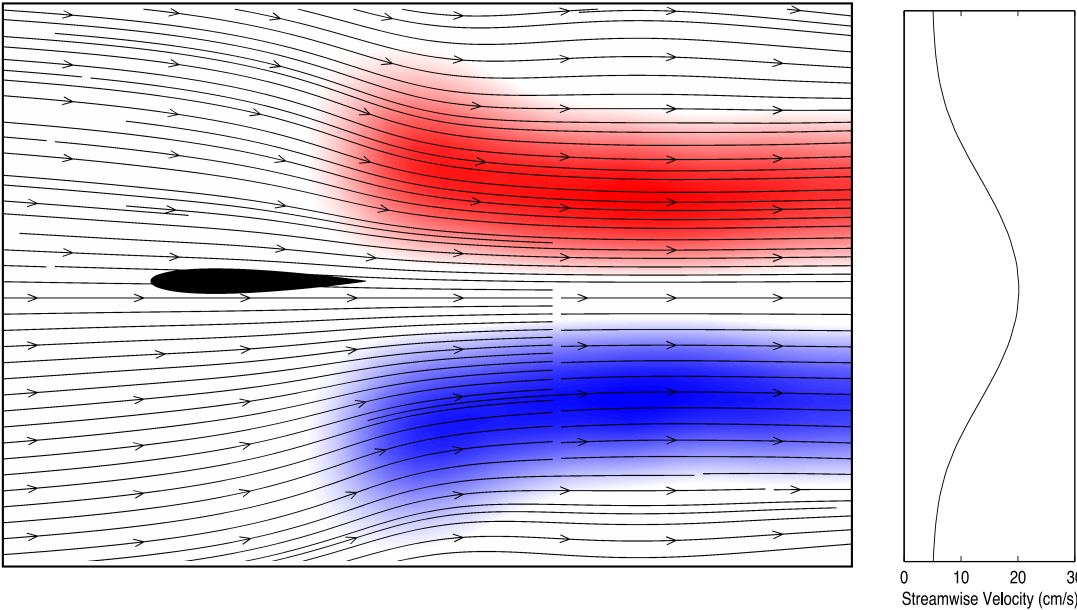


Figure 2.27: Time-averaged vorticity field for an airfoil pivoting about its leading edge ($p/c = 0$) with velocity profile measured one chord-length downstream of the trailing edge. A reverse von Kármán vortex street produces a jet behind the airfoil, shown by the contracting streamlines.

produces a net drag force. One such case is shown in figure 2.28, which shows the instantaneous vorticity field at one instant during the oscillation cycle. The corresponding time-averaged vorticity field is shown in figure 2.29. These contour plots were obtained for an airfoil pivoting about its half-chord point for $f/f_n = 0.85$, but the structures observed are similar across all of the drag-producing operating points. The instantaneous vorticity field is more complex in this case, showing multiple vortical structures being shed from the airfoil as it presents a large frontal area to the incoming flow. When time-averaged over a cycle, however, the flow field is revealed to be quite organized, with a well-defined recirculation region existing downstream of the airfoil. Two large opposite-sign vortices persist on either side of the airfoil and direct some of the flow forward toward the leading edge. The presence of this velocity defect, which is responsible for the large drag generated, is also clearly observed in the velocity profile of figure 2.29, measured a distance of one chord-length downstream of the airfoil's trailing edge.

2.7 Conclusions

In this study, we examine the performance of a NACA 0012 airfoil undergoing simultaneous pitching and heaving oscillations. Such oscillating airfoils have long been proposed as propulsors for small, unmanned aerial or underwater vehicles that might be used for reconnaissance, environmental monitoring, or other applications. Unique to this research, however, is our use of passive dynamics to govern the motion of the pitch axis. We find that leaving the control of the pitching motion to a torsion spring can produce up to an order of magnitude increase in thrust coefficient over a purely pitching airfoil if the system

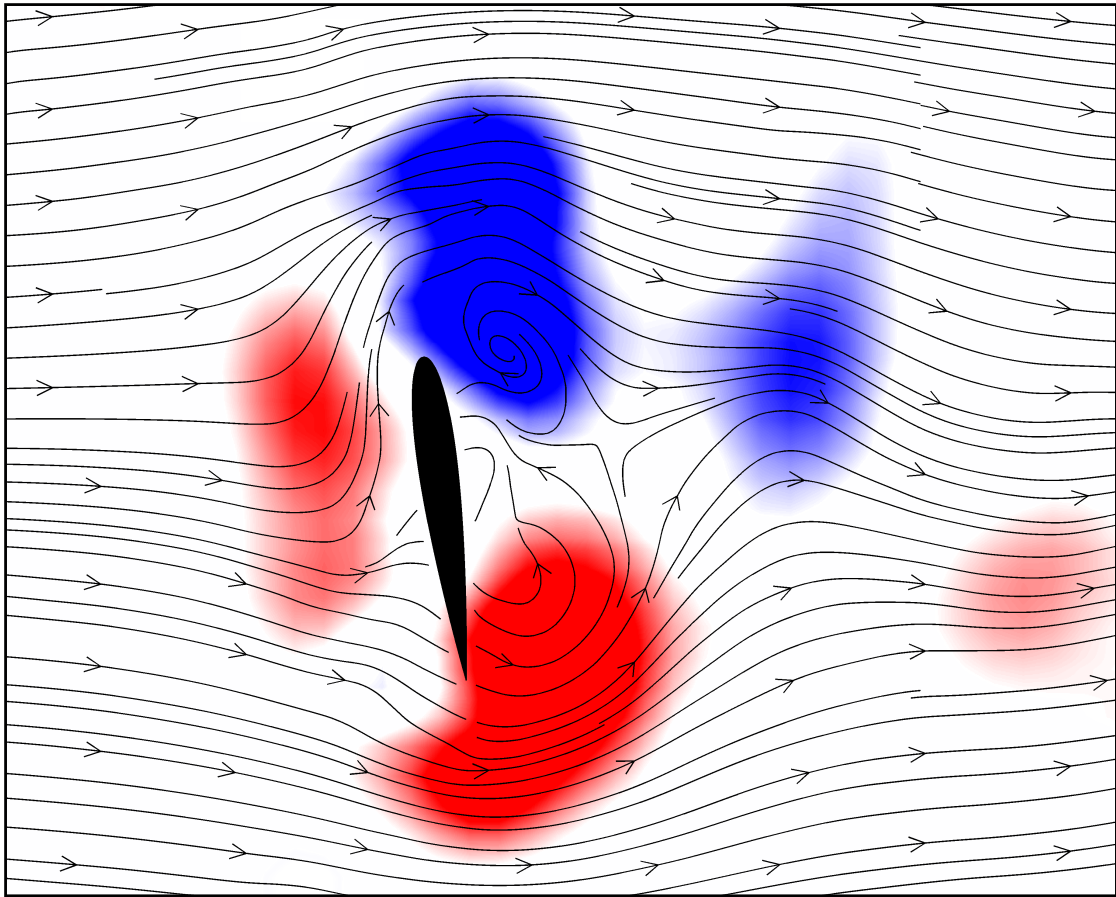


Figure 2.28: Instantaneous vorticity field for the airfoil pivoting about its half-chord point ($p/c = 0.50$), showing the more complex vortex shedding produced when the airfoil reaches large angles of attack.

is properly tuned to take advantage of the resonance condition. This increase in performance is achievable with minimal loss of efficiency and without requiring the addition of a second actuator and corresponding control and power systems. This last benefit can be particularly important for small flying vehicles, which often have constrained mass and energy budgets.

Key to this work is the application of the Cyber-Physical Fluid Dynamics (CPFD) technique, which allows us to combine measured fluid forces with virtual forces specified in software. In this case, the torsion spring exists solely as an equation programmed into our control software. This technique offers many

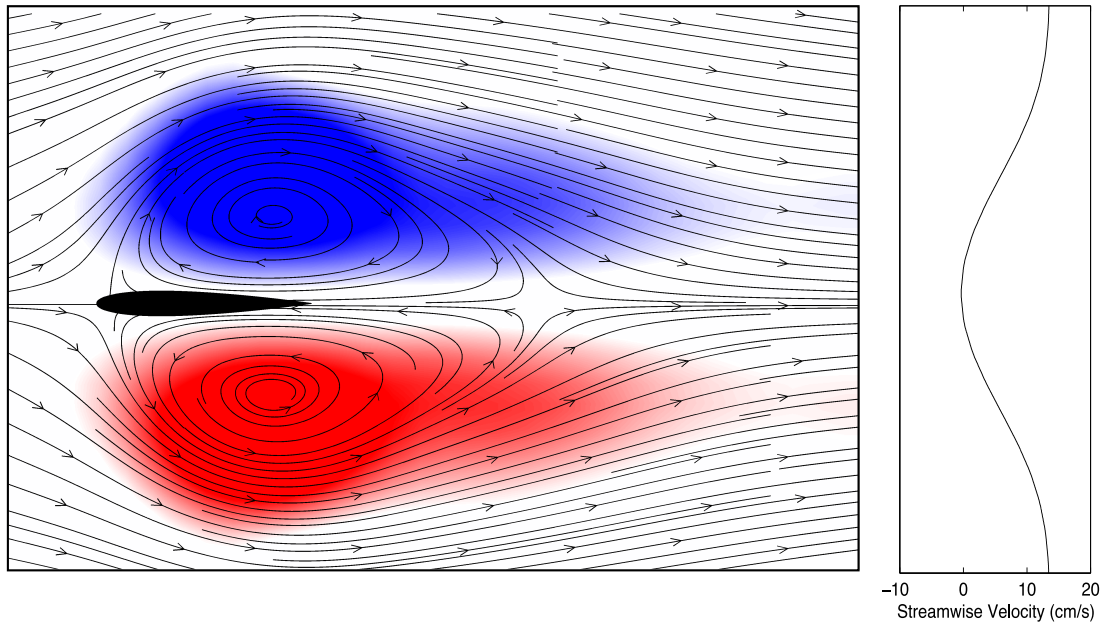


Figure 2.29: Time-averaged vorticity field for an airfoil pivoting about its half-chord point ($p/c = 0.50$), with velocity profile measured one chord-length downstream of the trailing edge. A recirculation region forms around the airfoil, directing some flow forward toward its leading edge and leading to large drag forces.

advantages over both traditional experiments and computational fluid dynamics. The virtual side of CPF_D allows us to change experiment parameters, including the airfoil’s dynamic properties, without making any adjustments to the hardware itself. Experiments covering large parameter spaces can run completely unattended. Simultaneously, we use a real fluid to “solve” the Navier-Stokes equations, thereby obtaining solutions more quickly than can generally be achieved with computational techniques.

Adding passive dynamics to a heaving airfoil allows us to significantly improve the airfoil’s thrust production. The amount of thrust obtained is dependent on the spring stiffness (and hence the natural frequency f_n of the system). We find that pivot points located forward of the airfoil’s center of mass result in

thrust production, while those located aft of the center of mass can cause large drag forces on the system. The best thrust performance occurs for pivots located at or forward of the airfoil's leading edge.

Proper selection of the frequency ratio f/f_n is also critical. Values of the frequency ratio between 0.5 and 1.25 produce reasonable amounts of thrust, with peak thrust at resonance occurring for $f/f_n \approx 0.75$. For drag production, the airfoil is most effective when the pivot point is located near its trailing edge. A negative resonance exists for these conditions, reaching drag coefficients up to twice the value for a static airfoil presenting its planform area to the incoming flow.

Plots of the airfoil trajectory with respect to undisturbed fluid are a simple and effective way to visualize the airfoil motions which produce thrust and drag. These trajectory plots can be synchronized with other variables, such as the instantaneous angle of attack and thrust coefficient. We find that moderate angles of attack are associated with good thrust performance. Such angles of attack keep the airfoil operating in a regime where lift forces are substantial but drag remains relatively small. As the angle of attack is increased further, drag increases significantly, and the airfoil begins to act as a brake rather than a propulsor.

The phase angle between pitching and heaving is critically important in determining the angle of attack and, consequently, whether the airfoil produces thrust or drag. All operating parameters for which the airfoil produces thrust have a phase angle greater than 180° ; that is, the pitching motion leads the heaving motion. Conversely, the heaving motion leads the pitching motion for all cases in which drag is produced. Examination of the effect of phase on the an-

gle of attack shows that, when thrust is produced, the pitching motion reduces the angle of attack generated by heaving the airfoil, moderating its value. With drag production, the pitching contribution to the angle of attack is additive with the heaving contribution, leading to the airfoil becoming oriented broadside to the incoming flow, producing large drag forces.

Oscillating airfoils have been subject to analysis for many decades, and the linearized theories of Theodorsen (1935), Garrick (1936) and Fernandez-Feria (2016) provide a means of predicting the forces and moments on the airfoil as a result of its motion through the fluid. These simplified classical theories are able to qualitatively capture the behavior of the thrust coefficient as a function of the frequency ratio but consistently overpredict the quantitative value of the thrust. This result is perhaps to be expected, given the assumptions about small oscillation amplitudes and a planar wake that underpin the theory. We can also use the theory to make *a priori* predictions of the pitching amplitude and phase by coupling it with the pitch equation of motion. The predictions for these two quantities are surprisingly good and, combined with the observations about pivot location and phase angle described earlier, can determine whether a given airfoil motion will produce thrust or drag.

The vortex dynamics associated with the wakes of oscillating airfoils show that when the airfoil is producing thrust, a jet forms downstream, which is consistent with the presence of a reverse von Kármán vortex street. In the drag mode, when the pivot point is located downstream of the center of mass, a far more complex wake develops as a result of the airfoil's large angle of attack. Viewed in time-averaged form, two counter-rotating vortices develop on either side of the airfoil, directing flow forward and delivering a large braking force.

Oscillating airfoils can be useful propulsive devices, and the results presented in this work illustrate how the use of passive dynamics to govern the pitch oscillation of a heaving airfoil can greatly improve performance over an airfoil operating with heave alone, provided that the natural frequency of the system and the pivot point are carefully selected. This improvement is achievable without the need for the added weight and power requirements of a second actuator for pitch. Depending on the pivot location, both thrust and drag forces can be produced, which may be exploited by small vehicles to improve their maneuverability. In practice, it may be possible to “tune” a passively pitching system by varying the natural frequency f_n of the oscillator. This could allow the system to remain operating at its resonance condition while still allowing the actuation frequency to be adjusted in order to produce the desired thrust coefficient. We hope that this study proves useful for the design of small aerial and underwater vehicles and also spurs further interest in the exploitation of passive unsteady aerodynamics as a propulsive mechanism.

This work was supported by the Air Force Office of Scientific Research Grant No. FA9550-15-1-0243, monitored by Dr. Douglas Smith.

REFERENCES

- ANDERSON, J.M., STREITLIEN, K., BARRETT, D.S. & TRIANTAFYLLOU, M.S. 1998 Oscillating foils of high propulsive efficiency. *J. Fluid Mech.* **360**, 41–72.
- ASHRAF, M.A., YOUNG, J. & LAI, J.C.S. 2012 Oscillation frequency and amplitude effects on plunging airfoil propulsion and flow periodicity. *AIAA J.* **50** (11), 2308–2324.
- BETZ, A. 1912 Ein beitrage zur erklärung des segelfluges. *Zeitschrift für Flugtechnik und Motorluftschiffahrt* **3** (21), 269–272.
- BUCHHOLZ, J.H.J. & SMITS, A.J. 2008 The wake structure and thrust performance of a rigid low-aspect-ratio pitching panel. *J. Fluid Mech.* **603**, 331–365.
- FERNANDEZ-FERIA, R. 2016 Linearized propulsion theory of flapping airfoils revisited. *Phys. Rev. Fluids* **1**, 084502.
- GARRICK, I.E. 1936 Propulsion of a flapping and oscillating airfoil. *Tech. Rep.* 567. National Advisory Committee on Aeronautics.
- GOVARDHAN, R. & WILLIAMSON, C.H.K. 2000 Modes of vortex formation and frequency response of a freely vibrating cylinder. *J. Fluid Mech.* **420**, 85–130.
- HEATHCOTE, S. & GURSUL, I. 2007 Flexible flapping airfoil propulsion at low reynolds numbers. *AIAA J.* **45** (5), 1066–1079.
- HOVER, F.S., HAUGSDAL, Ø. & TRIANTAFYLLOU, M.S. 2004 Effect of angle of attack profiles in flapping foil propulsion. *J. Fluids. Struct.* **19**, 37–47.
- HOVER, F.S., TECHET, A.H. & TRIANTAFYLLOU, M.S. 1998 Forces on oscillating uniform and tapered cylinders in crossflow. *J. Fluid Mech.* **363**, 97–114.
- ISRAELEVITZ, J.S. & TRIANTAFYLLOU, M.S. 2014 Adding in-line motion and model-based optimization offers exceptional force control authority in flapping foils. *J. Fluid Mech.* **742**, 5–34.
- JONES, K.D., BRADSHAW, C.J., PAPADOPOULOS, J. & PLATZER, M.F. 2005 Bio-inspired design of flapping-wing micro air vehicles. *Aero. J.* pp. 365–393.
- VON KÁRMÁN, T. & SEARS, W.R. 1938 Airfoil theory for non-uniform motion. *J. Aeronaut. Sci.* **5**, 370.
- KATZMAYR, R. 1922 Effect of periodic changes of angle of attack on behaviour of airfoils. *Tech. Rep.*. National Advisory Committee on Aeronautics.
- KNOLLER, R. 1909 Die gesetze des luftwiderstandes. *Flug und Motortechnik* **3** (21), 1–7.

- LEWIN, G.C. & HAJ-HARIRI, H. 2003 Modelling thrust generation of a two-dimensional heaving airfoil in a viscous flow. *J. Fluid Mech.* **492**, 339–362.
- MACKOWSKI, A.W. 2014 A cyber-physical approach to experimental fluid mechanics. PhD thesis, Cornell University.
- MACKOWSKI, A.W. & WILLIAMSON, C.H.K. 2011 Developing a cyber-physical fluid dynamics facility for fluid-structure interaction studies. *J. Fluids Struct.* **27** (5), 748–757.
- MACKOWSKI, A.W. & WILLIAMSON, C.H.K. 2015 Direct measurement of thrust and efficiency of an airfoil undergoing pure pitching. *J. Fluid Mech.* **765**, 524–543.
- MACKOWSKI, A.W. & WILLIAMSON, C.H.K. 2017 Effect of pivot location and passive heave on propulsion from a pitching airfoil. *Phys. Rev. Fluids* **2**, 013101.
- MCCROSKEY, W.J. 1982 Unsteady airfoils. *Annu. Rev. Fluid Mech.* **14** (1), 285–311.
- MCKINNEY, W. & DELAURIER, J. 1981 Wingmill: An oscillating-wing windmill. *AIAA J. Energy* **5** (102), 109–115.
- MICHELIN, S. & LEWELLYN-SMITH, S. 2009 Resonance and propulsion performance of a heaving flexible wing. *Phys. Fluids* **21**, 071902.
- MOORE, M.N.J. 2014 Analytical results on the role of flexibility in flapping propulsion. *J. Fluid Mech.* **757**, 599–612.
- PLATZER, M.F., JONES, K.D., YOUNG, J., & LAI, J.C.S. 2008 Flapping-wing aerodynamics: Progress and challenges. *AIAA J.* **46** (9), 2136–2149.
- READ, D.A., HOVER, F.S. & TRIANTAFYLLOU, M.S. 2003 Forces on oscillating foils for propulsion and maneuvering. *J. Fluids Struct.* **17**, 163–183.
- ROZHDESTVENSKY, K.V. & RYZHOV, V.A. 2003 Aerohydrodynamics of flapping-wing propulsors. *Prog. Aerosp. Sci.* **39** (8), 585–633.
- SFAKIOTAKIS, M., LANE, D.M. & DAVIES, J.B.C. 1999 Review of fish swimming modes for aquatic locomotion. *IEEE J. Oceanic Eng.* **24** (2), 237–252.
- SPAGNOLIE, S.E., MORET, L., SHELLEY, M.J. & ZHANG, J. 2010 Surprising behaviors in flapping locomotion with passive pitching. *Phys. Fluids* **22**, 041903.
- THEODORSEN, T. 1935 General theory of aerodynamic instability and the mechanism of flutter. *Tech. Rep.* 496. National Advisory Committee on Aeronautics.
- THIELICKE, W. 2014 The flapping flight of birds - analysis and application. PhD thesis, Rijksuniversiteit Groningen.

- THIELICKE, W. & STAMHUIS, E.J. 2014a Pivlab – towards user-friendly, affordable and accurate digital particle image velocimetry in matlab. *J. Open Research Software* **2** (1).
- THIELICKE, W. & STAMHUIS, E.J. 2014b Pivlab - time-resolved digital particle image velocimetry tool for matlab (version: 1.40).
- TRANTAFYLLOU, G.S., TRIANTAFYLLOU, M.S. & GROSENBAUGH, M.A. 1993 Optimal thrust development in oscillating foils with application to fish propulsion. *J. Fluids Struct.* **7** (2), 205–224.
- TUNCER, I.H. & PLATZER, M.F. 1996 Thrust generation due to airfoil flapping. *AIAA J.* **34** (2), 324–331.
- WILLIAMSON, C.H.K. & ROSHKO, A. 1988 Vortex formation in the wake of an oscillating cylinder. *J. Fluids Struct.* **2**, 355–381.
- WU, T.Y. 1961 Swimming of a waving plate. *J. Fluid Mech.* **10** (3), 321–344.
- YOUNG, J. & LAI, J.C.S. 2007 Mechanisms influencing the efficiency of oscillating airfoil propulsion. *AIAA J.* **45** (7), 1695–1702.

CHAPTER 3

SELF-PROPULSION OF A PITCHING AND HEAVING AIRFOIL

Abstract

We are interested in the self-propelling performance of a flapping airfoil which employs both pitching and heaving motions. In contrast to many other studies that have examined this type of propulsive mechanism, we employ a force-feedback technique and computer-controlled water channel to simulate true self-propulsion. This means that the vehicle travels at a speed at which the drag it generates equals the thrust produced by the airfoil. In this way, the incoming flow velocity is coupled to the airfoil motion and not set arbitrarily.

We vary both the normalized heave amplitude and the pitching amplitude over a large parameter space and present variables of interest in contour plots as functions of these motion amplitudes. Such variables include the cruising velocity, the propulsive economy, the transverse impulse, which is a measure of the transverse force on the airfoil, and the maximum angle of attack that the airfoil reaches during a cycle. In this way, we can overlay several contours and draw conclusions about the airfoil operating parameters which produce the most efficient propulsion.

In general, we find that the cruising speed achieved by the airfoil is more sensitive to the heave amplitude than to the pitch amplitude. However, pitch plays a crucial role in controlling the angle of attack, in effect moderating it and reducing flow separation. We show that reducing flow separation and the formation of a leading edge vortex (LEV) corresponds to increased propulsive

economy. In fact, the most efficient operating point for the angle of attack is the one just before significant flow separation occurs. The airfoil operates at a maximum angle of attack of about 18° , just before significant stall effects develop. This most efficient operating point also produces the minimum amount of transverse force on the airfoil and generates the least amount of circulation in the wake. Our experiments demonstrate that the additional circulation generated by suboptimal motions is principally contained in a leading edge vortex, providing further evidence that flow separation is detrimental to the performance of the airfoil as a propulsor. This additional shed circulation can also be viewed as wasted energy that is not used to propel the vehicle forward and instead contributes significantly to oscillating the airfoil in a direction perpendicular to the desired travel direction. In fact, the point at which the airfoil is most efficient as a propulsive device corresponds to a set of motions which produce a leading edge vortex of minimum strength.

3.1 Introduction

Flapping airfoils are of interest as propulsion mechanisms for small, micro-aerial or underwater vehicles. There has been a recent proliferation of such devices to be used for applications such as reconnaissance, search and rescue, and environmental monitoring as a result of improvements in power storage density and sensor miniaturization. Typically, these vehicles have employed traditional screw-type propellers to generate lift and propulsive forces. However, the obvious maneuverability advantages of flying and swimming animals which use flapping motions has spurred research into how flapping airfoils might be optimized for these purposes (Jones *et al.*, 2005) in addition to the fundamental desire to understand the physics of biological flight.

The majority of studies performed to date have examined the performance of pitching and heaving airfoils by decoupling their kinematics from the speed of the incoming fluid flow. That is, the airfoils are either towed at a constant speed in a towing tank or tethered in position in a water channel with a fixed freestream. The behavior of the airfoil as a propulsor under these conditions may not be representative of its true free-swimming or free-flying performance. This study seeks to contribute to our understanding of flapping airfoils by allowing the airfoil to move under its own power and to reach a steady-state velocity that corresponds to the condition of thrust equaling the drag on the body. We would like to understand which motions produce the optimal efficiency for a given forward velocity, and, more specifically, how the dynamics of the shed vortex wake are connected to efficient operation. This information is particularly important to maximize the range or endurance for small vehicles which may have significant power storage constraints.

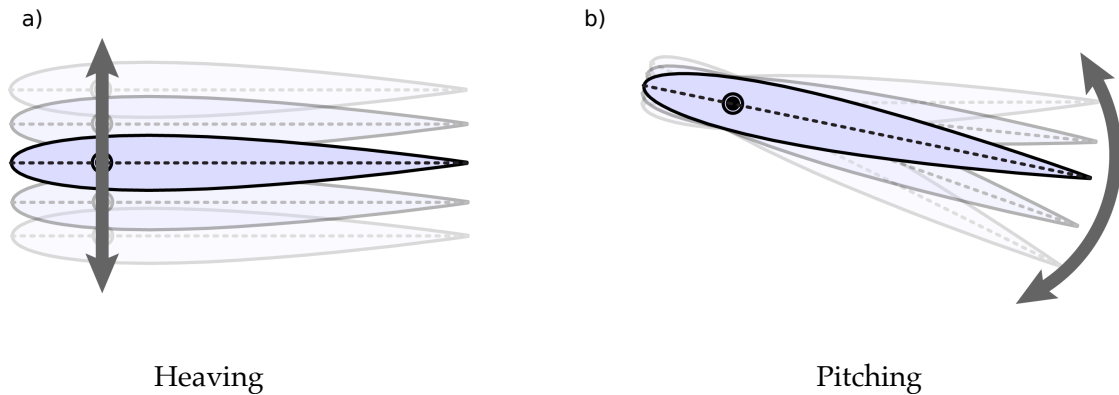


Figure 3.1: (a) Heaving is motion transverse to the airfoil chord. (b) Pitching is a pure rotation about a given pivot point.

Many studies have examined the performance of flapping airfoils and typically define flapping as a combination of two oscillatory motions: heaving, which is a motion transverse to the chord line of the airfoil, and pitching, which is a pure rotation about a designated point. These motions are illustrated in figure 3.1. Investigations of airfoils employing these motions in isolation or together are reviewed in McCroskey (1982), Rozhdestvensky & Ryzhov (2003), and Platzer *et al.* (2008).

Heaving motions are able to produce thrust through the Knoller-Betz effect, first described by Knoller (1909) and Betz (1912) and confirmed experimentally by Katzmayr (1922), which refers to the rotation of the lift vector into the direction of motion. This rotation is a product of the vector addition of the heaving velocity and the forward velocity of the vehicle. On the other hand, pitching motions have no such steady-state mechanism through which they can generate thrust. Rather, thrust is generated through unsteady vortex shedding. The efficiency of pitching is typically lower than that for pure heave (Buchholz & Smits, 2008; Mackowski & Williamson, 2015), but pitching does allow finer control over the instantaneous angle of attack reached by an airfoil during its oscil-

latory cycle.

Combinations of pitching and heaving motions typically provide the best performance, and such configurations have been extensively studied. For example, Anderson *et al.* (1998) demonstrated that a pitching and heaving NACA 0012 airfoil could achieve propulsive efficiencies of up to 87%. In their seminal work, they demonstrated the importance of controlling the maximum angle of attack that the airfoil reaches during a cycle. Moderate angles of attack allow for the best performance. The phase angle between pitching and heaving is also critical in that it has a strong influence on the angle of attack seen by the airfoil. Typically, phase differences of around 90° , with pitching leading the heaving motion, provide excellent thrust and efficiency (Anderson *et al.*, 1998; Read *et al.*, 2003). Instead of using two actuators to produce the pitching and heaving motions, the performance of a heaving airfoil can be improved by the addition of flexibility (Heathcote & Gursul, 2007) or by allowing the airfoil to pitch passively using a torsion spring (Asselin *et al.*, 2018).

The presence or absence of a leading edge vortex (LEV) can strongly influence the performance of an airfoil. Young & Lai (2007) found that the timing of its generation determines whether it will enhance thrust and efficiency or hinder them. In general, though, they find that the presence of an LEV is harmful to the performance of an airfoil as a propulsor. Other studies, such as Heathcote & Gursul (2007) and Lewin & Haj-Hariri (2003) have shown that the addition of pitching can moderate the angle of attack and weaken the leading edge vortex, thereby improving performance.

Existing studies of self-propelled flapping vehicles typically fall into two broad categories: those which are based on mimicking the motion profiles of

real fish, such as Lauder *et al.* (2007) and Wen *et al.* (2012), and more fundamental studies that involve pitching and heaving airfoils, many of which are reviewed by Wang *et al.* (2016). We take the latter approach in this study and will briefly review some of the recent work in this area.

Vandenberghé *et al.* (2004) has examined the operating conditions under which a heaving wing will propel itself. In their experimental work, a wing was oscillated vertically in a circular tank and allowed to rotate as it generated thrust. They found that there is a critical Reynolds number, based on heaving frequency, below which the wake structures generated by the wing are symmetrically distributed and consequently do not produce any thrust. Above this critical Reynolds number, the symmetry of the wake is broken and the system is able to self-propel, achieving a steady-state velocity which is proportional to the heaving frequency. In this case, the wake takes on the familiar inverse von Kármán street configuration, indicative of a jet behind the airfoil. In later work (Vandenberghé *et al.*, 2006), they examined the effects of heaving amplitude and airfoil thickness, finding that larger amplitudes increase the self-propelled velocity and that thinner airfoils perform better as propulsive devices.

Alben & Shelley (2005) numerically confirmed the existence of the critical transition Reynolds number and also observed that the symmetry-breaking phenomenon seen in experiments may be related to the instability of the von Kármán vortex wake behind bluff bodies. The transition Reynolds number also depends on the geometry of the body, with thinner airfoils able to transition to propulsion at lower Reynolds numbers (Zhang *et al.*, 2009).

Others have examined the benefits of adding flexibility to self-propelling airfoils. Thiria & Godoy-Diana (2010) conducted experiments using a rotating

“merry-go-round” system with a heaving flexible airfoil. They found that the addition of flexibility could reduce the power consumption by up to 60% while also increasing the thrust produced. Alben *et al.* (2012) simulated the behavior of a thin flexible foil heaved at its leading edge and found that the steady-state swimming velocity exhibits resonance peaks as the bending rigidity is varied. The benefits of flexibility for a pitching and heaving airfoil have also been examined using numerical simulation by Kim *et al.* (2016). They found that different bending stiffnesses are required to optimize a heaving airfoil for swimming speed and for efficiency but that flexibility generally improves both. Swimming speed was optimized for a phase difference between pitching and heaving of 90° . Kim *et al.* (2016) also found that the addition of a pitching actuation can also improve efficiency, but only if the pitching amplitude is carefully selected.

Olivier & Dumas (2016) further demonstrated the importance of tuning the airfoil characteristics to the actuation method in their computational study of a two-dimensional flexible flat plate oscillating in pitch and heave. The ratio of pressure forces to inertia forces, determined in part by the airfoil’s density, can be a significant parameter. They discovered that both the airfoil’s self-propelled velocity and efficiency were maximized for a specific value of this ratio, which depends on the specific parameters of the problem. Flexibility can also further improve the efficiency of the system.

There are many geometrical parameters that can affect the behavior of the airfoil. Yeh & Alexeev (2016) varied the aspect ratio of a heaving flexible plate and found that plates with smaller aspect ratio performed better, measured in terms of both swimming velocity and efficiency, than those of large aspect ratio. Consequently, three-dimensional effects are significant. Specifically, they

found that minimizing the strength of “side-edge vortices,” which form along the edges of the foil, led to improved efficiency. These vortices did not contribute any thrust but instead merely dissipated energy. As low-aspect-ratio foils are much wider than those of high aspect ratio, the amount of energy dissipated per unit width is minimized in the former case.

As an alternative to flexible airfoils, many of the same benefits can be obtained by mounting the airfoil on a torsion spring that allows it to pitch passively. One such experiment was conducted by Spagnolie *et al.* (2010) in which a pair of elliptical airfoils attached to torsion springs were actuated in the heave direction and allowed to self-propel in a circular tank. They found that there are frequency ranges in which the passively pitching airfoil outperformed the purely heaving airfoil, similar to the effect of adding chordwise flexibility. Experiments by Asselin *et al.* (2018) used a force-feedback control system to investigate a heaving airfoil with a torsion spring and found that there are distinct resonance peaks in the thrust coefficient that occur as the heaving frequency approaches the natural frequency of the system. The pivot point is also an important variable; pivots located forward of the airfoil center of mass produce thrust, while those aft of the center of mass produce drag.

In this study, we are interested in a comprehensive examination of the performance of an actively pitching and heaving airfoil in a self-propelling configuration. In contrast to the traditional approach to flapping airfoil studies, we allow the airfoil to choose its own incoming flow velocity, which corresponds to the point at which the thrust produced is equal to the drag. We examine a large range of heaving and pitching amplitudes and determine the characteristics that are essential to efficient propulsion, with particular attention given to

the vortex configuration shed by the airfoil.

In this paper, experimental methods are discussed in §3.2. We discuss the propulsive performance of a pitching and heaving airfoil which is allowed to propel itself through a fluid in §3.3, including the pitching and heaving amplitudes which produce the most efficient propulsion. Further detail on specific cases is provided in §3.4, with a focus on three specific operating points for the airfoil that all deliver the same forward velocity: one that produces the maximum efficiency and two others which are suboptimal. In §3.5, we discuss the vortex dynamics that are responsible for determining the energy consumption for a specific airfoil motion. §3.6 discusses some interesting aspects of the flow associated with operating the airfoil at a high pitch amplitude. Conclusions follow in §3.7.

3.2 Experimental Methods

Experiments are conducted at the Cornell University Fluid Dynamics Research Laboratories using a hybrid X - Y - θ water channel. The water channel is an Eidetics model 1520 free-surface, closed-loop water channel with a test section of width 38 cm, length 150 cm, and depth 46 cm. A schematic showing the major components of this facility is shown in figure 3.2. The test object for these experiments is a NACA 0012 airfoil of chord 7.5 cm and submerged depth 24 cm. The airfoil is attached to a carriage which is capable of motion in the streamwise (x), transverse (y), and rotational (θ) directions. The airfoil pierces the free surface at the top of the channel. At the lower end of the span, the airfoil is positioned above an endplate in order to ensure the flow is as two-dimensional as possible.

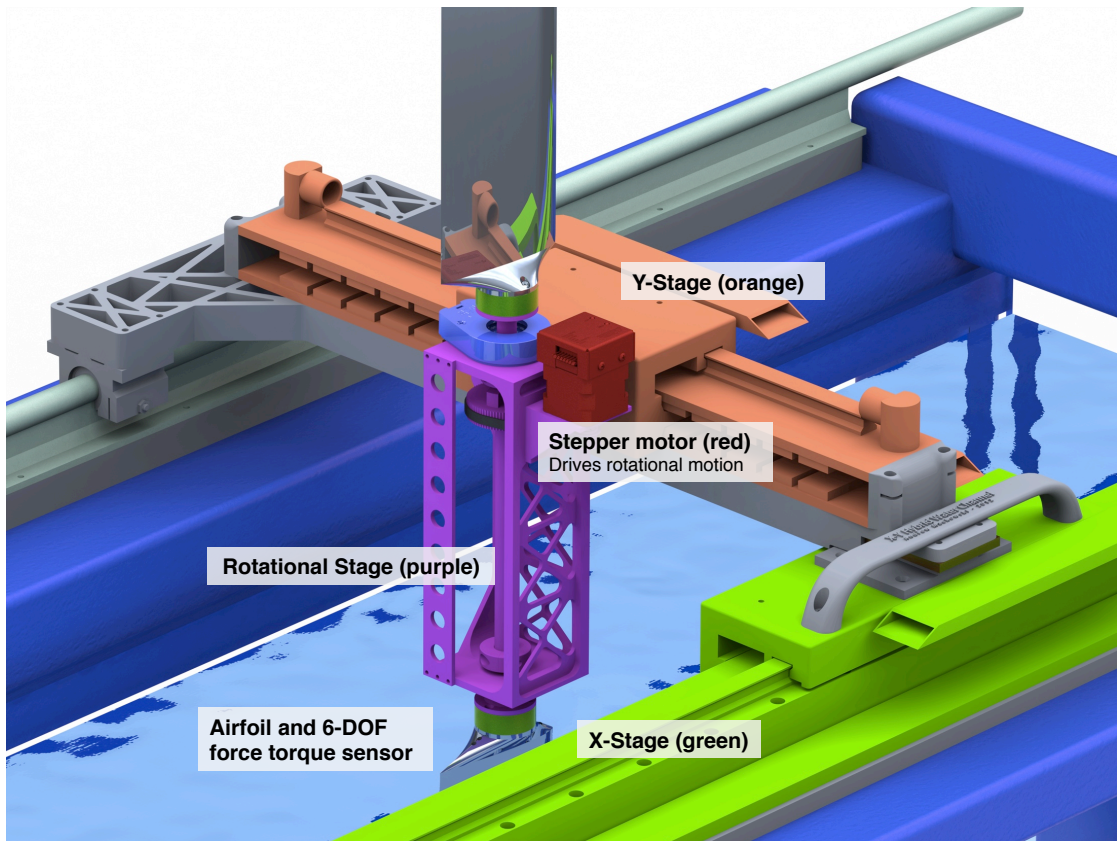


Figure 3.2: Schematic showing the X-Y- θ hybrid water channel. The streamwise (x) linear stage is shown in light green, and the transverse (y) linear stage is in orange. Rotation is provided by a stepper motor, shown in red, which drives the rotational stage (purple). Each airfoil is attached to a 6-axis force/torque sensor, shown in dark green.

Forces and moments are measured using 6-axis force/torque sensors from ATI Industrial Automation.

The three motion axes are controlled by a computer-controlled force-feedback system. In a technique that we call Cyber-Physical Fluid Dynamics (CPFD), the force-feedback system allows virtual forces to be specified in software. These virtual forces, which may represent physical objects such as linear or torsion springs, are combined with the measured fluid forces, and velocity commands are then sent to the motors controlling the airfoil to make it move as

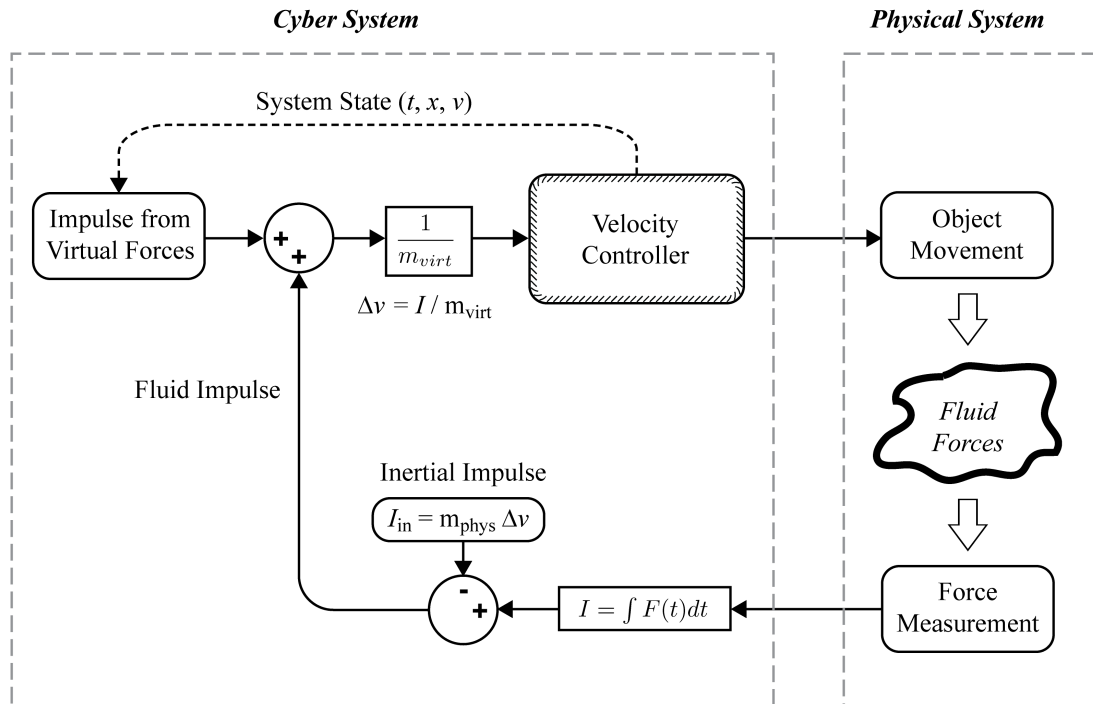


Figure 3.3: Schematic showing operation of the CPFD control system (Mackowski & Williamson, 2011; Mackowski, 2014).

if it were subject to all of these forces combined. Furthermore, we also employ a second airfoil which moves in the air only. The forces and moments experienced by this airfoil represent inertial effects only, and measuring them directly allows us to separate the inertia of the airfoil in the water from the fluid forces acting on it. The inertial properties of the airfoil, such as its mass and moment of inertia, then become parameters which can be arbitrarily set. Further details on the CPFD technique can be found in Mackowski & Williamson (2011) and Mackowski (2014), and a flow chart illustrating the operation of the control system is shown in figure 3.3.

In these experiments, we wish to use CPFD to simulate an airfoil propelling itself through the water using heaving and pitching motions. The heaving motion is determined by a sinusoidal function with amplitude h_0 and frequency

f .

$$y(t) = h_0 \cos(2\pi ft) \quad (3.1)$$

In addition to heaving, the airfoil also pitches about its leading edge according to equation 3.2.

$$\theta(t) = \theta_0 \cos(2\pi ft - \phi) \quad (3.2)$$

where θ_0 is the pitching amplitude, and ϕ is the phase difference of the pitching motion relative to the heaving motion. In all experiments discussed here, ϕ is set to 90° , so that the pitching motion leads the heaving motion by a quarter cycle. This choice of phase angle has been shown to provide excellent efficiency in other studies (Anderson *et al.*, 1998).

As the airfoil oscillates in pitch and heave, it generates a thrust that is measured by the force/torque sensors. The CPFDD control system then uses the measured force to move the airfoil forward in the test section with an acceleration determined by Newton's Second Law of Motion. The test section has a limited length, however. In order to allow experiments to run for long periods of time, CPFDD also integrates with the water channel pump and a laser doppler velocimeter that can be used to measure the channel flow speed. Consequently, as the airfoil accelerates, the channel pump speed is adjusted so that the channel flow speed matches the velocity of the airfoil. Because the channel pump cannot respond instantly to changes in the airfoil velocity, the difference is corrected by moving the airfoil through the fluid with the streamwise (x) stage. Once the system is operating at steady-state, the airfoil remains stationary in the channel,

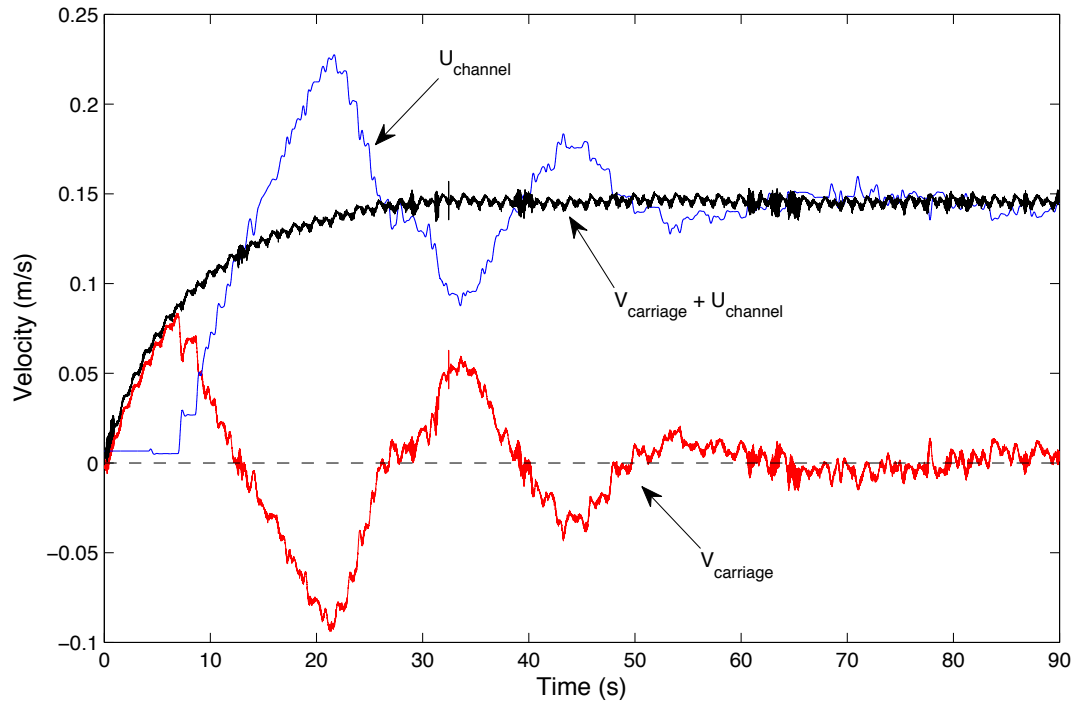


Figure 3.4: The CPFDF control system maintains the proper incident velocity on the airfoil (black) using a combination of channel flow velocity (blue) and carriage motion (red). The use of a PID controller for the water channel pump causes overshooting and undershooting of the desired velocity during the transient phase. The motion of the carriage is used to compensate for these deviations, thereby always maintaining the correct velocity as seen by the airfoil.

and the experiment can run indefinitely.

Control of the water channel pump is accomplished through a simple PID controller, which is underdamped in order to achieve reasonable convergence times. Underdamped controllers typically exhibit overshooting and undershooting behavior; however, it is possible to compensate for this effect by adjusting the speed of the streamwise (x) stage of the carriage. At all times, the velocity incident on the airfoil remains correct, as shown in figure 3.4.

Our experiment configuration offers many advantages over other approaches to studying self-propelled vehicles. The use of a water channel al-

lows us to conduct experiments of indefinite duration. Furthermore, because our force/torque sensors are attached to the airfoil and therefore only measure forces acting on it directly, the added mass and drag of the experiment support hardware has no effect on the motion of the airfoil through the water. The velocity seen by the airfoil, delivered by a combination of carriage and channel flow velocities, is a true representation of the speed at which a real vehicle would be driven. The force-feedback control system also permits us to study all aspects of the self-propulsion problem, including the transient phase as the airfoil accelerates to its steady-state speed.

Because our water channel has a limited range of achievable flow speeds, we must select the motion parameters of the airfoil carefully so as to remain within this range. Steady-state operation is achieved when the drag force on the airfoil is equal to the thrust that it produces. In order to explore a broad range of airfoil motions and for a more realistic simulation of self-propelling vehicles, we have the option to add an additional virtual body drag force using the CPFDF control system. The drag law is given by equation 3.3 and is proportional to U^2 .

$$D = \frac{1}{2}\rho U^2 S_w C_D \quad (3.3)$$

where ρ is the fluid density, U is flow speed incident on the airfoil, S_w is the total wetted area of the propulsor and virtual body, and C_D is the drag coefficient of the virtual body that is being propelled by the airfoil.

Many other studies, including Moored & Quinn (2017), also define the virtual body drag in terms of the Lighthill number, Li , defined in equation 3.4.

$$Li = C_D S_{wp} \quad (3.4)$$

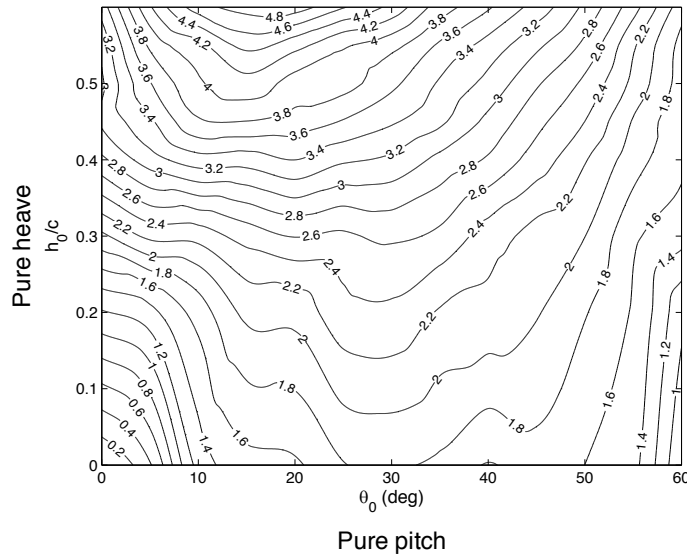
where $S_{wp} = S_w/S_p$ is the ratio of the wetted surface area of the entire vehicle (virtual body and airfoil propulsor), S_w , to the planform area of the airfoil propulsor, S_p . Since $S_w = S_{wp}S_p$, equation 3.3 can be rewritten as

$$D = \frac{1}{2}\rho U^2 S_{wp} S_p C_D \quad (3.5)$$

Substituting the definition of the Lighthill number yields an equation for the drag in terms of Li and the planform area of the airfoil S_p :

$$D = \frac{1}{2}\rho U^2 S_p Li \quad (3.6)$$

The Lighthill number, first introduced in a slightly different form by Eloy (2012), makes it easy to compare vehicles of differing geometries and drag coefficients. For a given thrust from the propulsor, vehicles with a large Lighthill number will have a small self-propelled velocity, and vehicles with a small Lighthill number will have a large self-propelled velocity. Biological systems typically operate with $0.01 < Li < 1$ (Eloy, 2012), which encompasses the Lighthill number examined here. For most of the experiments discussed in this work, we chose $Li = 0.35$ because it is both in the range of Lighthill numbers that are characteristic of biological systems and also provides steady-state cruising velocities that are well matched to the range of velocities that can be achieved with our water channel. Further experiments conducted at $Li = 0.08$ and $Li = 1.00$ produce very similar results for efficiency and wake vortex dynamics to those we will discuss for $Li = 0.35$.



The heave-pitch diagram can be populated by contours of:

- Reduced velocity, U^*
- Propulsive economy, $\frac{\bar{U}}{\bar{p}}$
- Maximum angle of attack, α_{max}
- Transverse impulse, I_y

Among other data sets

Figure 3.5: Heave-pitch diagram: results are generally presented as contours which are functions of pitching amplitude and heaving amplitude. In this “heave-pitch diagram,” the horizontal axis represents purely pitching motion, and the vertical axis represents purely heaving motion. Here, contours of reduced velocity are shown for $Li = 0.35$.

In these experiments, we examine the performance of the airfoil as a propulsor over a wide range of motion parameters, including cases involving pure pitch and pure heave. In general, we display results in contour plots as functions of pitching amplitude and heaving amplitude, as shown in figure 3.5. Heaving amplitude is normalized by the airfoil chord. These contour plots are powerful tools that allow the relationships between variables important to the problem to be discovered and explored.

Typical performance metrics include the self-propelled velocity, expressed in non-dimensional form by equation 3.7. This reduced velocity represents the distance traveled by the airfoil, expressed in terms of chord lengths, for each oscillation cycle.

$$U^* = \frac{\bar{U}}{fc} = \frac{UT}{c} = \frac{\text{Distance traveled}}{\text{Chord length}} \quad (3.7)$$

where T is the period of one oscillation of the airfoil.

In order to evaluate the efficiency of the self-propelled vehicle, several metrics may be employed. The classic propulsive efficiency, defined as the ratio of the thrust coefficient to the power coefficient, is not useful for self-propulsion experiments because the net force becomes equal to zero at steady-state. Instead, a more useful and potentially more intuitive metric is the propulsive economy, defined by equation 3.8.

$$PE = \frac{\bar{U}}{\bar{P}} \quad (3.8)$$

where \bar{U} is the mean self-propelled velocity achieved by the airfoil, and \bar{P} is the mean input power needed to produce the pitching and heaving motions. This mean input power is defined as follows:

$$\bar{P} = \frac{1}{T} \left(\int_0^T [F_y(t)\dot{h}(t) + M_z(t)\dot{\theta}(t)] dt \right) \quad (3.9)$$

where T is the period of one oscillation cycle, F_y is the force in the heaving direction, \dot{h} is the heaving velocity, M_z is the moment acting about the pitching axis, and $\dot{\theta}$ is the pitching velocity.

The propulsive economy has units of distance traveled per energy consumed, making it analogous to a fuel economy measurement, which is particularly useful in the case of a vehicle that propels itself using onboard sources of energy.

In addition to the velocity and efficiency measurements described above, we also examine the wake generated by the airfoil using particle image velocimetry. The particles used are Potters' Industries Sphericel 110P8 (mean diameter $10\mu\text{m}$ and density 1.10gcm^{-3}). An approximately 3-mm thick light sheet is generated using a New Wave Research dual Nd:YAG laser and a series of hemispherical and cylindrical lenses. The flow is imaged by a JAI CV-M2CL 2-megapixel camera at a rate of 8 Hz, yielding 16 frames per cycle of the airfoil motion. All of the components of the PIV system, including the laser and camera, are controlled by the same CPF D LabVIEW program that runs the experiment in the water channel. This capability enables all of the activities to be synchronized so that accurate phase averaging is possible. The velocity fields are computed using PIVLab running in MATLAB (Thielicke & Stamhuis, 2014*a,b*; Thielicke, 2014). We use a final window size of 64×64 pixels with 50% overlap. In order to see the complete vorticity field on each side of the airfoil, we run each PIV experiment at least twice, with opposite sides of the airfoil illuminated in each. In post-processing, the two velocity fields are combined in order to eliminate areas in each individual field where the shadow cast by the airfoil makes it impossible to collect velocity data.

In the specific case of the self-propelling airfoil, the airfoil tends to drift slightly forward and back in the channel as the control system compensates for small changes in the channel flow velocity and the natural acceleration of the airfoil. As this would make phase-averaging difficult in the case of PIV, we instead run PIV experiments in a tethered mode. The average forward and aft motion of the airfoil, which is a real phenomenon due to the unsteady nature of the propulsive force, is measured from an untethered, self-propulsion experiment. The velocity data derived from this experiment is then used to drive the

streamwise motion of the airfoil during tethered PIV experiments. This technique ensures that the motion of the airfoil is predictable and repeatable, essential qualities for capturing accurate velocity fields.

Estimates of the uncertainty in measured quantities are made using the bootstrap method. For reduced velocity, the 95% confidence interval for pure heave is approximately $\pm 0.52\%$. For operating conditions delivering optimum propulsive economy, the uncertainty is $\pm 0.50\%$. At higher pitching amplitudes, the uncertainty is $\pm 0.21\%$. For the propulsive economy, the 95% confidence intervals for these three operating conditions are $\pm 0.39\%$, $\pm 0.60\%$, and $\pm 0.48\%$, respectively. Finally, measurements of the circulation in the wake shed by the airfoil have a confidence interval given by $\pm 1.2\%$, based on approximately 30 averaged PIV frames.

3.3 Propulsive Performance

Figure 3.5 shows contours of reduced velocity for $Li = 0.35$. Examination of the vertical axis of the contour plot shows the behavior for a purely heaving motion. As the heave-to-chord ratio increases, the velocity at which the airfoil can propel itself increases significantly. Along the horizontal axis, the airfoil is executing a purely pitching motion. Pitch alone is not as effective at propelling the airfoil compared to heave, leading to lower speeds in general and a slower increase in forward speed as pitch amplitude is increased. Furthermore, there appears to be a point at which further increases in pitching amplitude are counter-productive, leading to a reduction in self-propelled velocity.

As described in §3.1, several other studies have found that a combination of

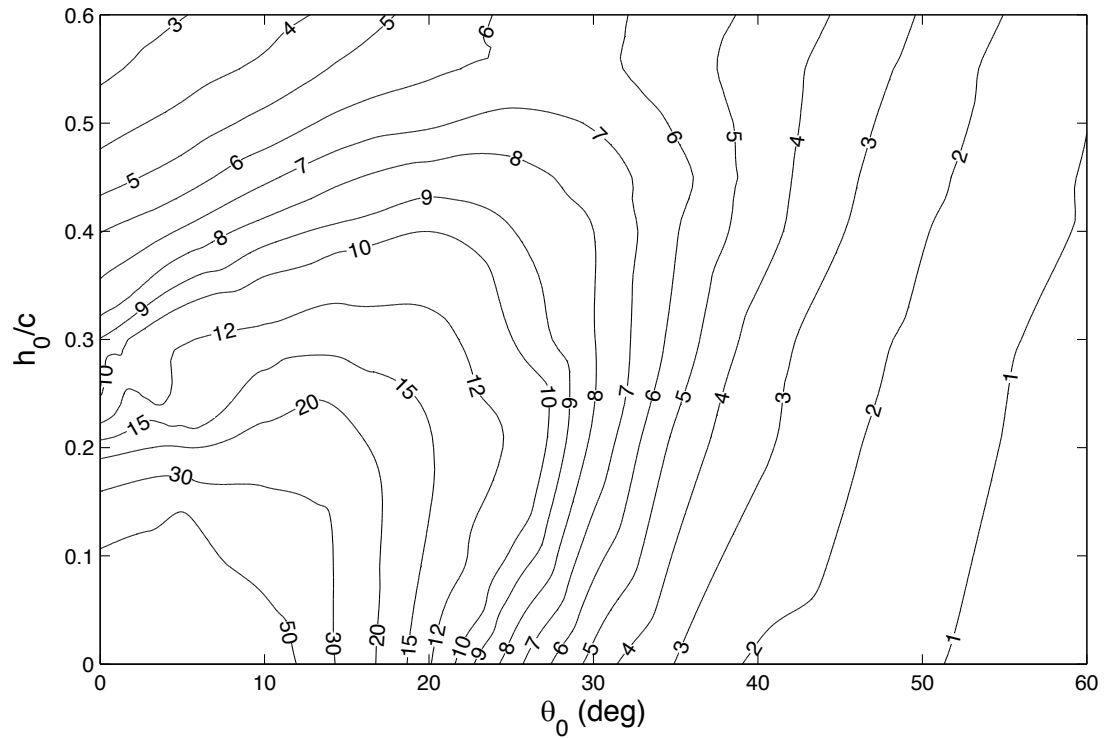


Figure 3.6: Contours of propulsive economy (m/J) as a function of heave-to-chord ratio and pitching amplitude for an oscillating airfoil with $Li = 0.35$, displayed in the heave-pitch diagram.

pitching and heaving motions leads to the best performance for an oscillating airfoil. From figure 3.5, we see that allowing the airfoil to pitch allows the same forward speed to be achieved with a smaller heaving amplitude. In order to evaluate whether this is actually a more efficient motion for propulsion, we need to examine the propulsive economy, which is shown in figure 3.6.

As one moves from left to right along a single velocity contour in the heave-pitch diagram, such as those shown in figure 3.5, the pitching amplitude increases. The pitch amplitude drives significant changes in the performance of the airfoil, including its propulsive economy. Figure 3.7 shows the propulsive economy as a function of pitching amplitude for three reduced velocities. Each of these curves has a reasonably distinct peak at which the propulsive economy

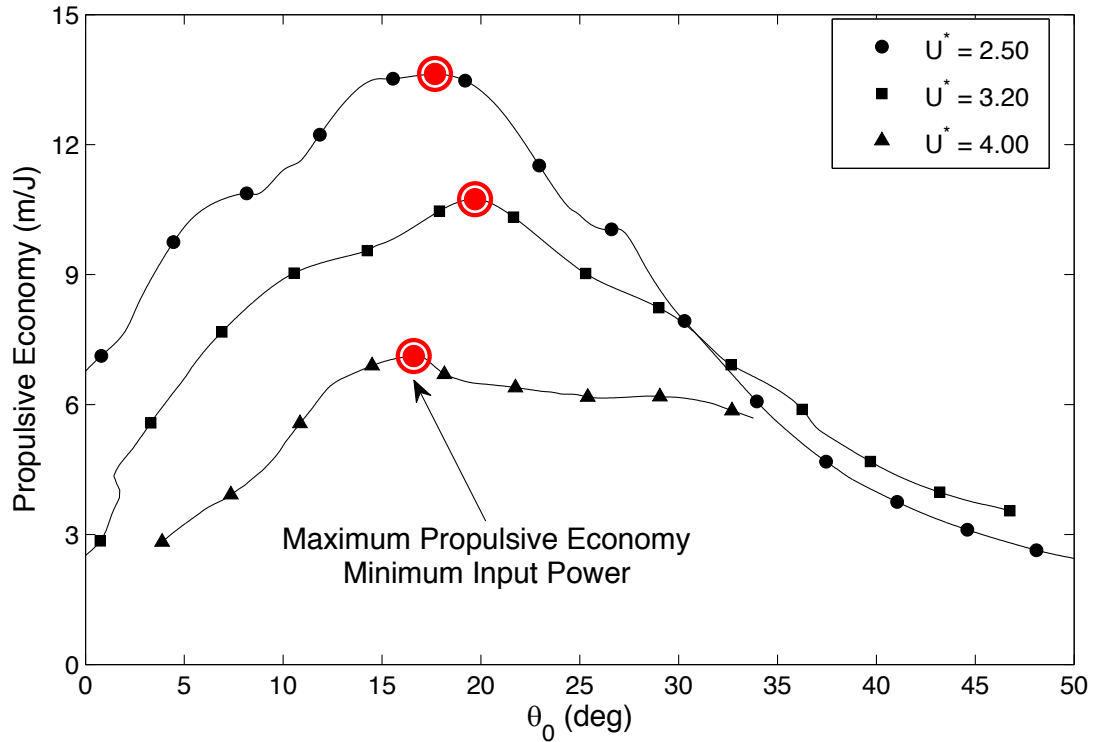


Figure 3.7: Propulsive economy vs. pitching amplitude, θ_0 , for three reduced velocities. Each curve has a peak value, indicating the pitching amplitude at which the airfoil is operating most efficiently.

is maximized, meaning that the airfoil can travel the furthest distance with a given amount of energy.

Central to computing the propulsive economy is the input power needed to oscillate the airfoil, defined by equation 3.9. This equation shows two contributions to the input power. The first term represents the power needed to heave the airfoil, and the second the power needed to pitch the airfoil. To see how these power inputs affect the propulsive economy, we show in figure 3.8 the power contributions from pitch and heave as functions of pitching amplitude θ_0 for $U^* = 3.20$. For small pitching amplitudes, the input power is dominated by the heaving motion, as expected. However, as the pitch amplitude is increased, the amount of power needed to heave the airfoil decreases dramatically, leading

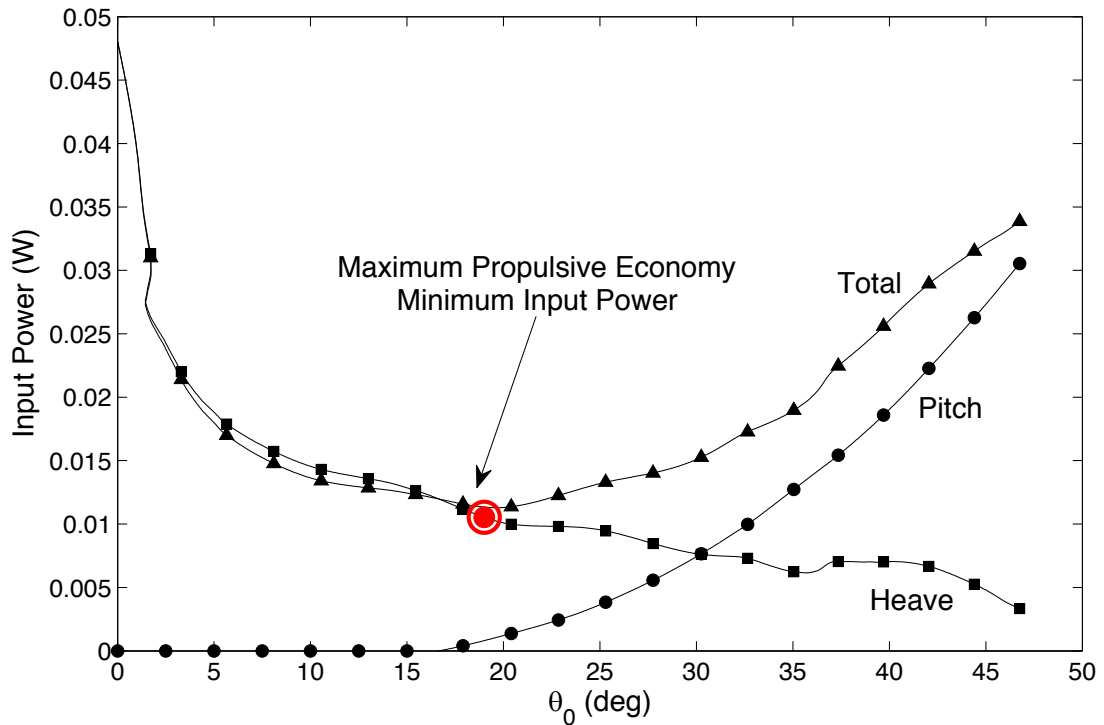


Figure 3.8: Input power from pitching and heaving motions for $U^* = 3.20$. At low pitching amplitudes, most of the input power is a result of the heaving motion. The addition of moderate pitching reduces the amount of power needed to drive the airfoil. A pitch amplitude that is too large, however, also increases the total power required.

to a minimum total input power (and maximum propulsive economy) around $\theta_0 = 20^\circ$. For pitching amplitudes beyond the optimum, the heave input power continues to decline, but any advantage gained is quickly overwhelmed by the increasing power needed to produce the large pitching motions.

The airfoil motion parameters which deliver the most efficient propulsion for a given velocity can also be understood by using contours plotted in the heave-pitch diagram. In order to determine which combination of pitch and heave yields the best economy, we can overlay the velocity and economy contours, as illustrated by the schematic in figure 3.9.

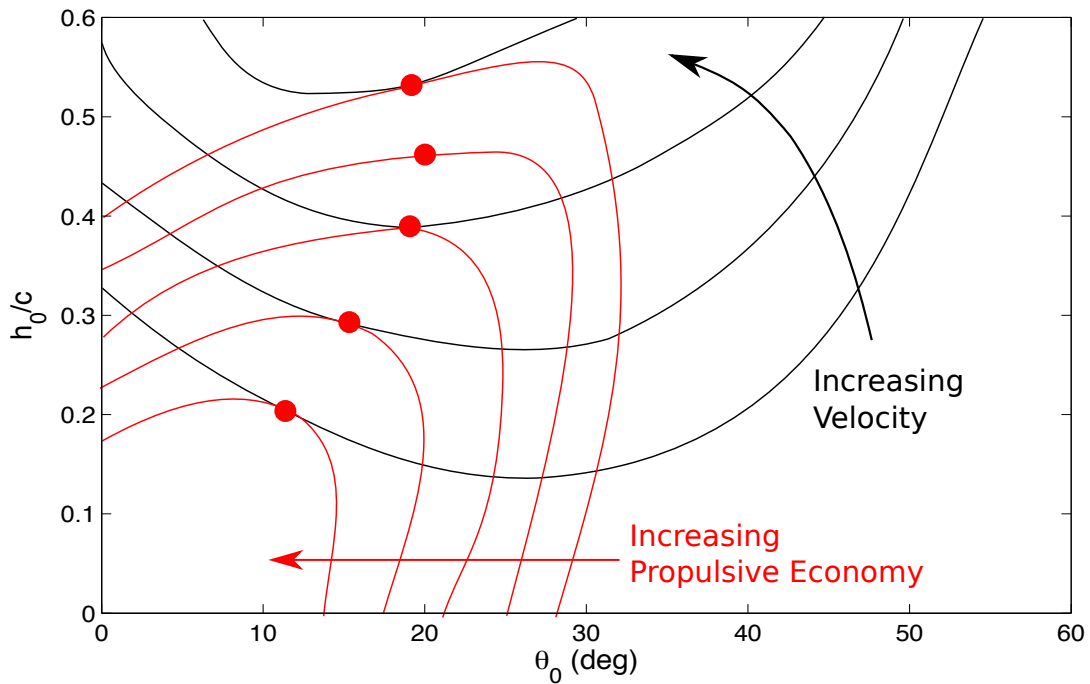


Figure 3.9: Schematic illustrating overlaid contours of reduced velocity (black) and propulsive economy (red) in the heave-pitch diagram. The red dots indicate the maximum propulsive economy contour that is intersected by a given velocity contour.

Since the propulsive economy generally increases as the heaving and pitching amplitudes are minimized, the motion parameters that provide peak efficiency are those that roughly correspond to the point on the velocity contour which is closest to the origin of the heave-pitch diagram. These points, denoted by the red dots in figure 3.9 are shown for the experimental data in figure 3.10. Maximum efficiency occurs with the addition of moderate pitching to the heaving motion.

In order to understand why these configurations of pitch and heave deliver the most efficient means of propulsion, we can begin examining other variables of interest, beginning with the transverse impulse. If the purpose of a propulsor is to drive a vehicle forward, then the generation of forces oriented perpen-

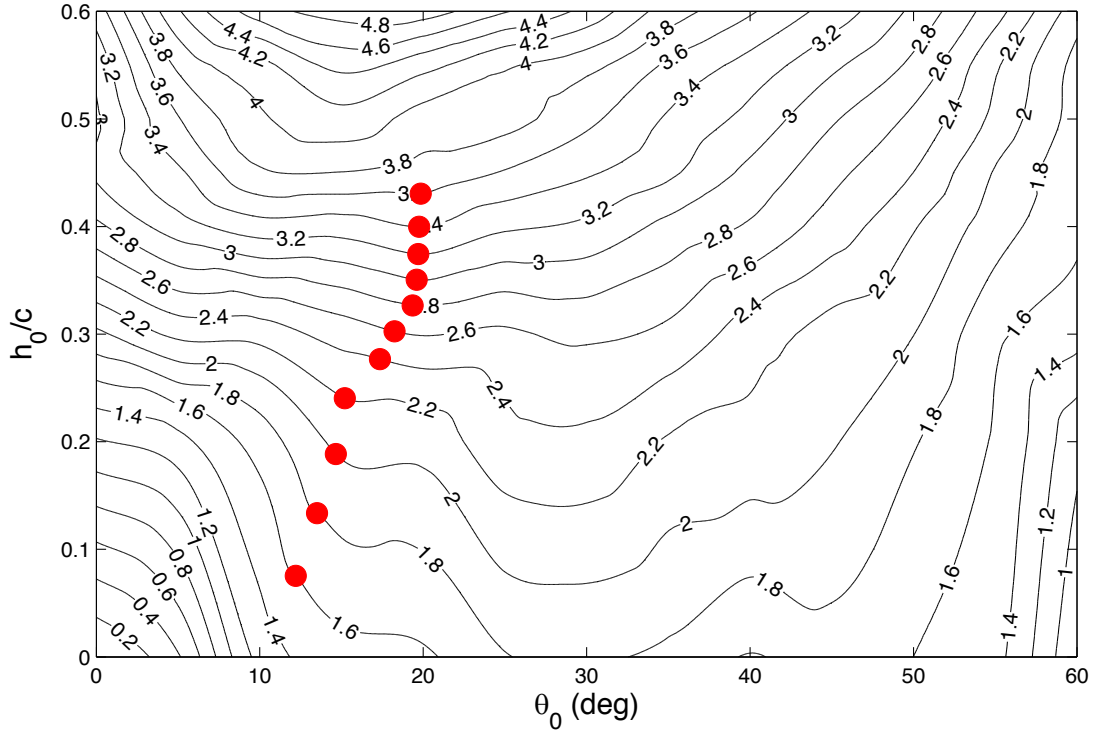


Figure 3.10: Contours of reduced velocity for $Li = 0.35$ with points of maximum propulsive economy labeled (red dots) in the heave-pitch diagram.

dicular to this direction may be considered as a waste of energy. Though the transverse forces are symmetric, resulting in no net lateral motion of the vehicle, the energy used to move the vehicle in this direction does not serve a useful purpose.

In order to quantify the amount of transverse forcing that the airfoil experiences, we define the transverse impulse as in equation 3.10:

$$I_{transverse} = \int_0^T |F_y(t)| dt \quad (3.10)$$

where the absolute value symbol is used to account for all of the transverse forcing, both positive and negative, without regard for its sign. In this way, we

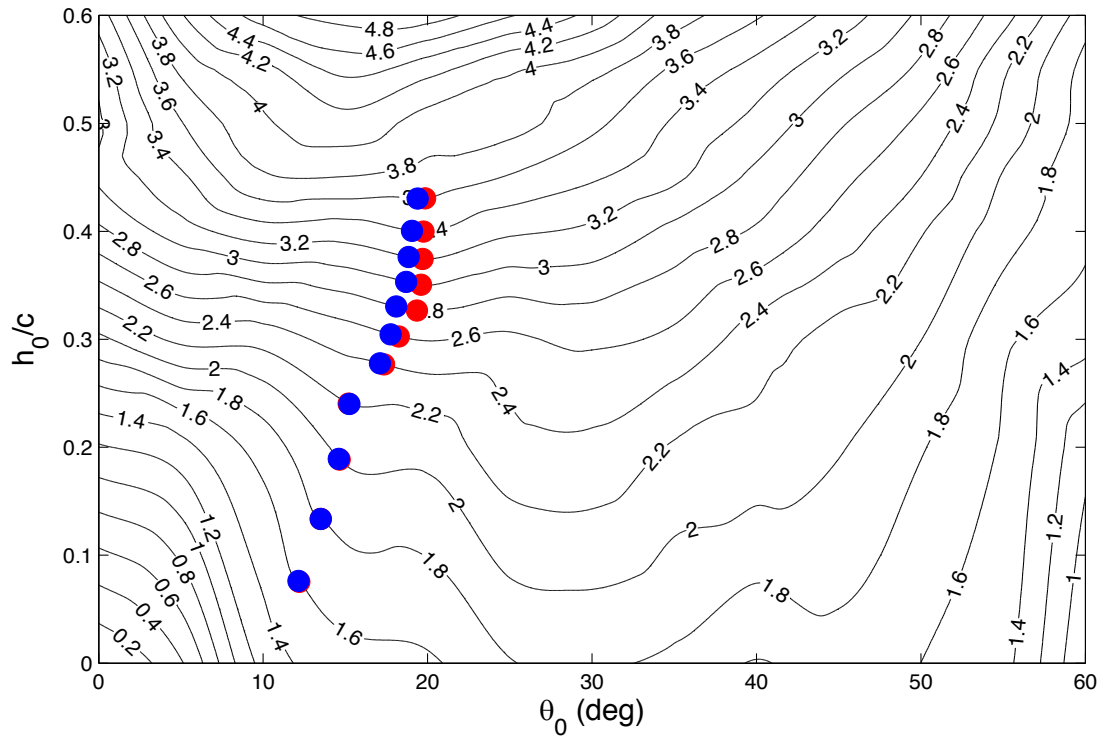


Figure 3.11: Contours of reduced velocity for $Li = 0.35$ in the heave-pitch diagram with points of maximum propulsive economy (red dots) and minimum transverse impulse (blue dots) labeled. There is excellent agreement between the points of maximum propulsive economy and minimum transverse impulse.

get a measure of the total side force generated by the airfoil.

In a manner similar to that used for the propulsive economy, we can find the point along each velocity contour at which the transverse impulse is minimized. These points, indicated by blue dots, are shown along with the points of maximum propulsive economy in figure 3.11.

The agreement between the points at which maximum economy and minimum transverse impulse occur is remarkable and shows that minimizing the generation of forces in directions other than the desired travel direction is important in order to achieve efficient propulsion.

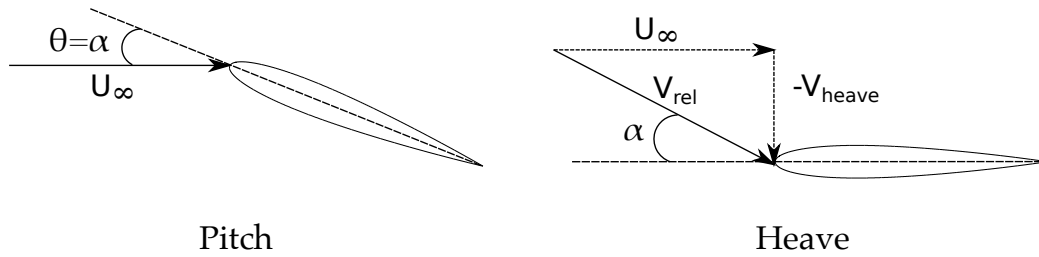


Figure 3.12: Schematic showing the angle of attack produced by pitching and heaving motions. For pure pitching, the angle of attack is equal to the pitching angle. For heaving, the heaving velocity adds vectorially to the incoming flow velocity. Consequently, the relative velocity seen by the airfoil has a nonzero angle of attack.

The angle of attack reached by the airfoil during a cycle is also of interest and is given by equation 3.11.

$$\alpha = -\arctan\left(\frac{\dot{h}(t)}{U(t)}\right) + \theta(t) \quad (3.11)$$

in which $\dot{h}(t)$ is the heaving velocity of the airfoil. This equation includes the contributions to the angle of attack from both the heaving motion (the first term) and the pitching motion (the second term), as shown in figure 3.12. When the airfoil is moved in the heave direction, the heaving velocity adds vectorially to the incoming flow velocity, turning the relative velocity and creating a nonzero angle of attack. The contribution to the angle of attack from pitching is simply the pitching angle. The combination of these effects produces the overall angle of attack seen by the airfoil.

Contours of the maximum angle of attack reached by the airfoil during a complete cycle are presented in figure 3.13. In this figure, the angle of attack is computed at the leading edge of the airfoil. The red dots again indicate the points where propulsive economy is a maximum for the range of velocities

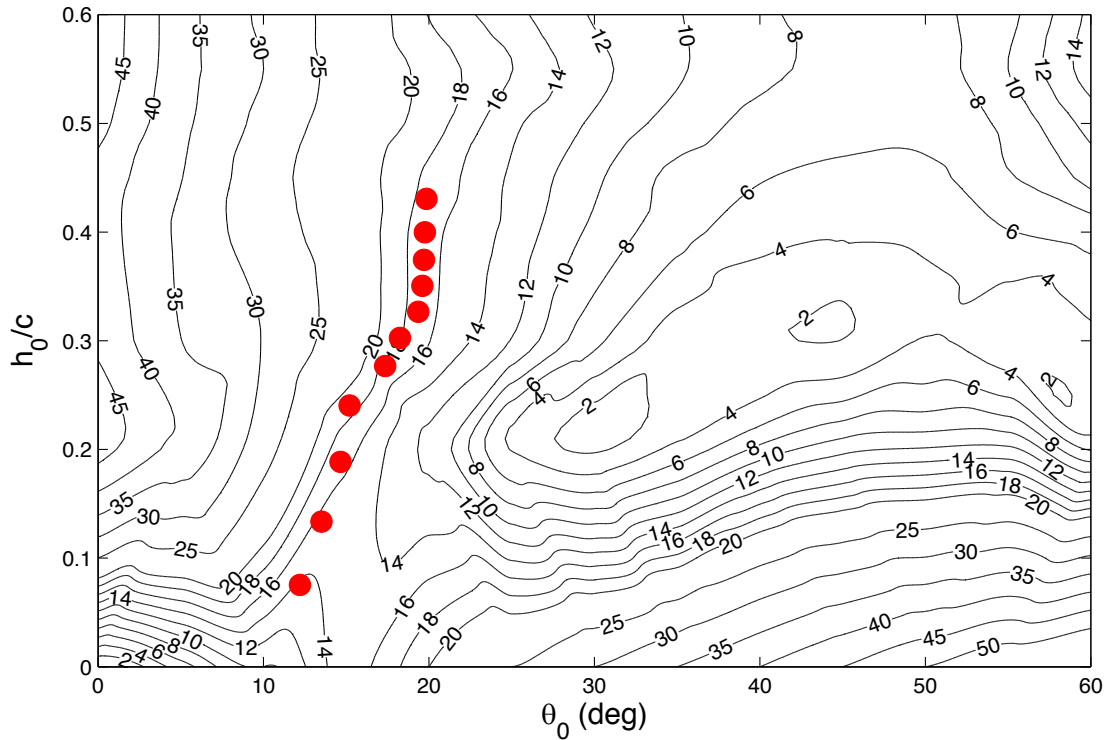


Figure 3.13: Contours of maximum angle of attack for $Li = 0.35$ with points of maximum propulsive economy (red dots) labeled.

shown in figure 3.10.

It is remarkable that the curve representing these optimal maximum angles of attack lies closely along the contours for $\alpha = 18 - 20^\circ$. From Abbott & von Doenhoff (1959), we know that these values are essentially the maximum possible angle of attack that can be reached before stall occurs. The vortex dynamics corresponding to this condition are investigated in §3.5.

3.4 Trajectory Plots

The experiments discussed in §3.3 show that the proper choice of operating parameters is key to the use of an oscillating airfoil as an efficient propulsor. In

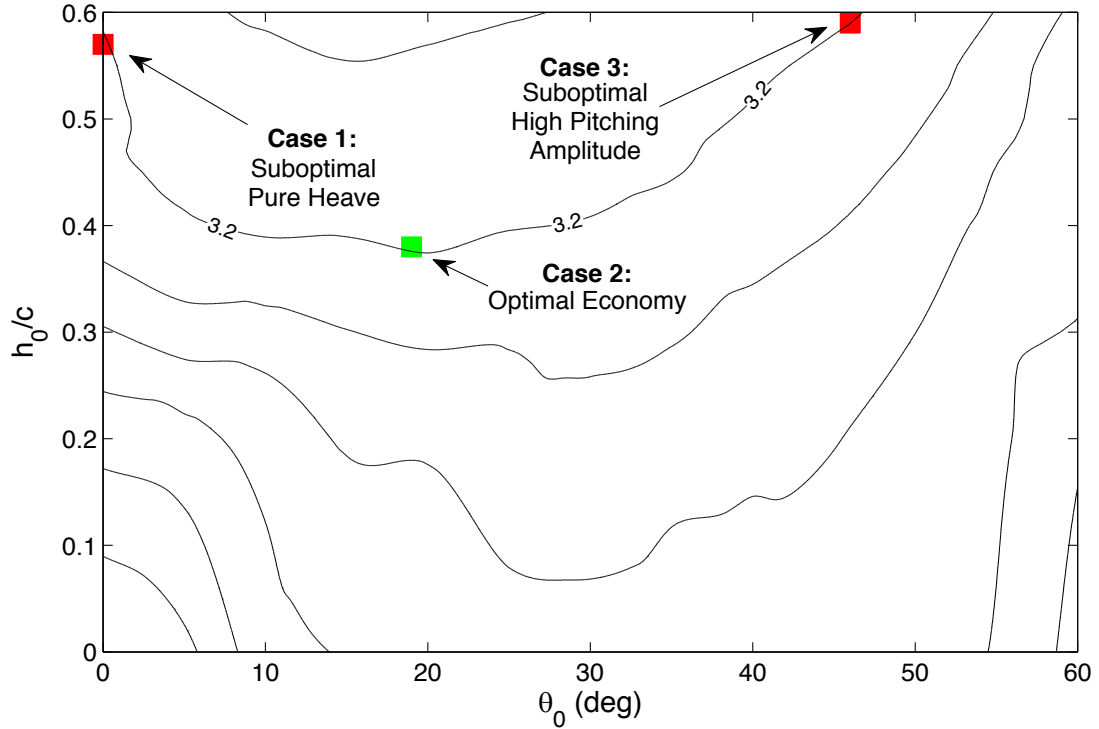


Figure 3.14: Contours of reduced velocity for $Li = 0.35$ with three operating conditions for the same reduced velocity ($U^* = 3.20$) highlighted. The green square represents the case in which the propulsive economy is maximized, and the red squares indicate operating cases for which more energy is required to move the vehicle at this speed.

Case	Normalized Heave Amplitude	Pitch Amplitude
Case 1: Optimal Economy	$h_0/c = 0.37$	$\theta_0 = 19^\circ$
Case 2: Pure Heave	$h_0/c = 0.57$	$\theta_0 = 0^\circ$
Case 3: High Pitch Amplitude	$h_0/c = 0.60$	$\theta_0 = 47^\circ$

Table 3.1: Three operating points along the $U^* = 3.20$ contour.

this section, we examine operating parameters which allow the vehicle to travel at the same reduced velocity but at different propulsive economies. One of the points to be studied represents the optimal case. We also discuss two suboptimal operating points, one for pure heave and another in which we use heave with a reasonably large pitch amplitude. The cases to be presented appear in figure 3.14 as square symbols and in table 3.1.

To travel at a reduced velocity of $U^* = 3.20$, the best economy is achieved for a heave-to-chord ratio of 0.37 and a pitching amplitude of 19 degrees. We use a simple format in a number of figures where we allow the airfoil to move past a stationary observer from right to left. This is quite useful as it can indicate physically the motion of the airfoil along its path and the angle of attack relative to the trajectory. Along with such a “trajectory plot,” we show the transverse force coefficient, C_Y , and the angle of attack, α , all synchronized to the trajectory. Figure 3.15 shows this trajectory plot for the optimal economy case. For optimal propulsion, the transverse force coefficient is relatively small, and the maximum angle of attack reached during a cycle at the airfoil’s leading edge is moderate at about 16 degrees. A NACA 0012 airfoil stalls at approximately 16 degrees (Abbott & von Doenhoff, 1959), so this angle of attack is likely still within the range where we have attached flow.

In contrast to the case of optimal economy, propelling the vehicle at the same speed but using only a heaving motion (Case 2) requires over three times as much energy per unit of distance traveled. That is, the propulsive economy is one third of the value achieved in Case 1. Correspondingly, as shown in figure 3.16(b), the transverse force coefficient is 209% higher than in the optimal case, indicating that much of that energy is devoted to creating ultimately useless lateral oscillations of the vehicle that cannot be used to assist the desired forward motion. The maximum angle of attack that the airfoil reaches is also far higher at 48° than the optimal case ($\alpha = 16^\circ$), which is deep into the region where stall and flow separation would be expected to occur.

As the pitching amplitude θ_0 is further increased (Case 3), the airfoil must consume more energy and execute larger amplitude heaving motions in order

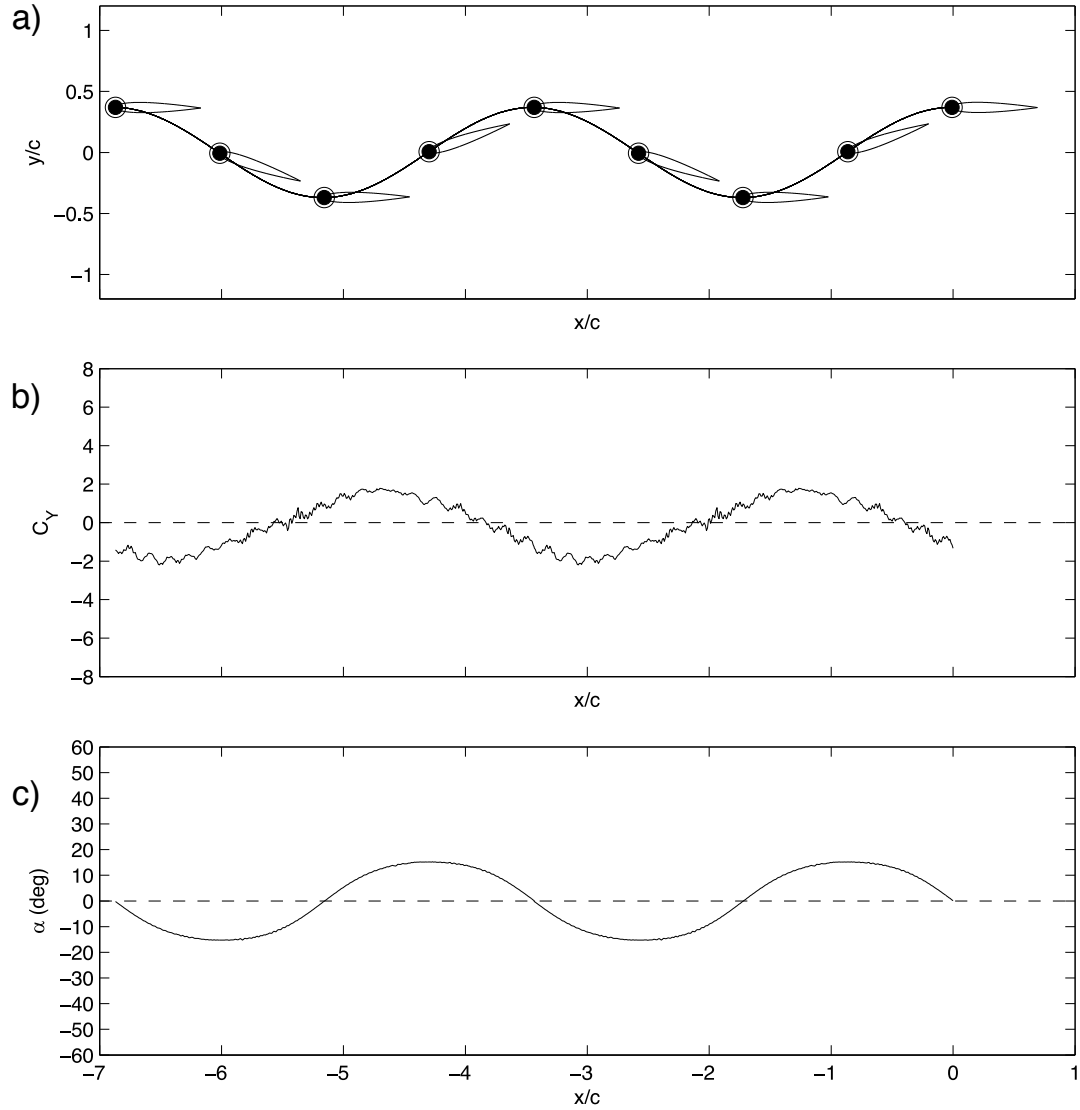


Figure 3.15: “Trajectory plot” for Case 1, Optimal Economy: (a) Airfoil trajectory for $h_0/c = 0.37$, $\theta_0 = 19^\circ$, and $U^* = 3.20$ (b) Transverse force coefficient synchronized with the trajectory. (c) Instantaneous angle of attack, measured at the leading edge, synchronized with the trajectory. Scales on plots are selected to facilitate comparison with later trajectory plots.

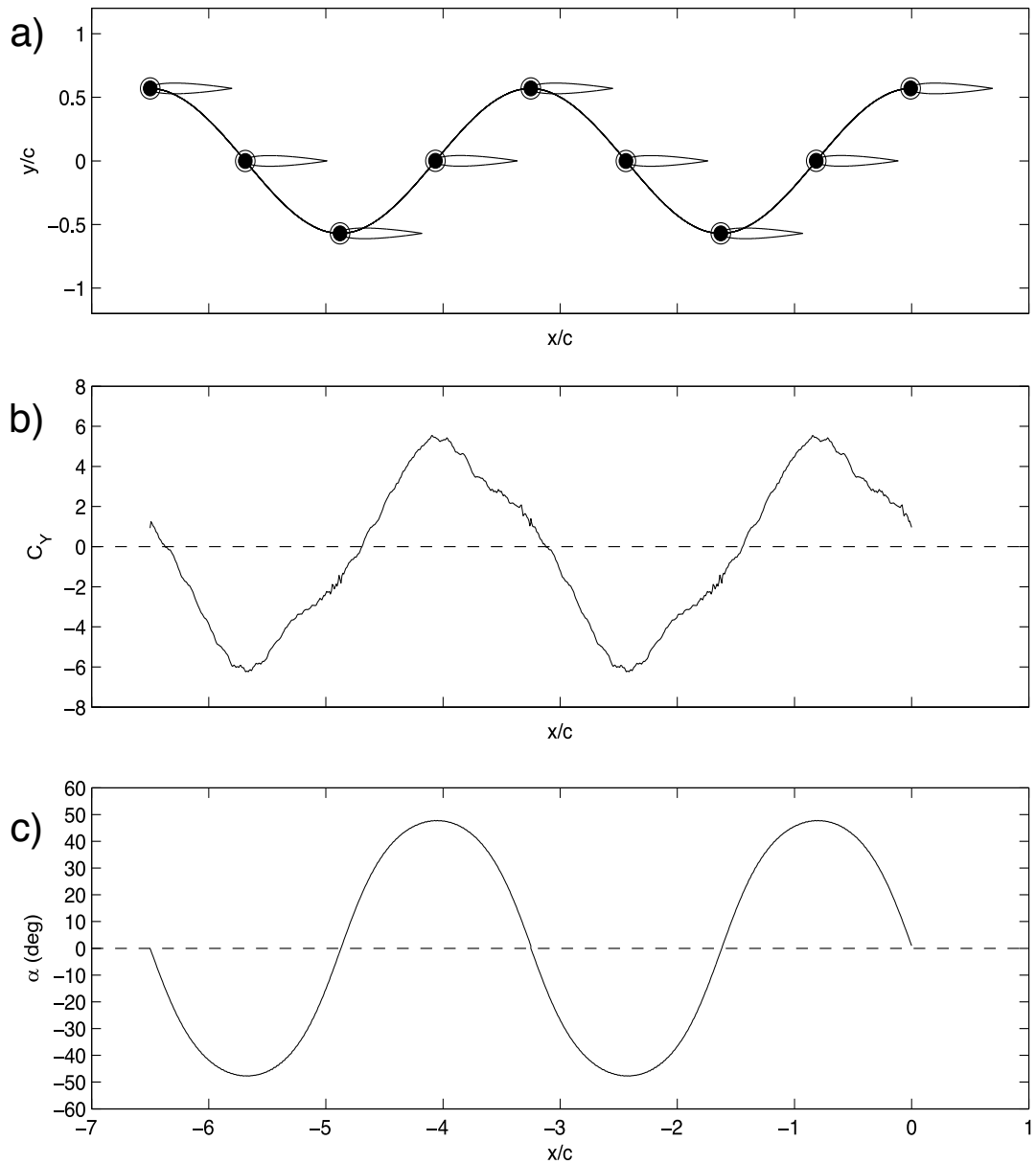


Figure 3.16: “Trajectory plot” for Case 2, Pure Heave: (a) Airfoil trajectory for $h_0/c = 0.57$, $\theta_0 = 0^\circ$, and $U^* = 3.20$ (b) Transverse force coefficient synchronized with the trajectory. (c) Instantaneous angle of attack, measured at the leading edge, synchronized with the trajectory.

to maintain the same cruising velocity. Simultaneously, more of the energy expended is used in the production of large transverse forces, as shown in figure 3.17. In this case, the maximum transverse force coefficient, C_Y , is comparable to that generated by the purely heaving motion previously discussed, and the airfoil again consumes about three times as much energy per unit of distance traveled as it does in the case of optimal economy.

Finally, we also note that operation at high pitch amplitudes, in addition to being inefficient, also produces much larger oscillations in cruising velocity than do airfoil motions using smaller amplitude pitching. Figure 3.18 provides an illustration of this phenomenon, in which we show the velocity of the airfoil in the travel direction for $h_0/c = 0.37$ and $\theta_0 = 19^\circ$, the optimum for $U^* = 3.20$, along with that for $h_0/c = 0.60$ and $\theta_0 = 47^\circ$, the high pitch amplitude case discussed earlier. The amplitude of the velocity fluctuations is 2.8% for the optimum propulsive case but is almost three times larger (8.2%) when the airfoil uses the highest pitch amplitude considered. This effect may be important for vehicle design, as cruising with large streamwise velocity changes might be undesirable for some applications, such as remote sensing.

3.5 Vortex Dynamics

A comparison of the vorticity distributions generated by the airfoil for these three cases also reveals important differences. Figures 3.19 and 3.20 show a sequence of vorticity contours for Case 1, the optimal motion profile (figure 3.19) and Case 2, pure heave (figure 3.20), depicting the development of the wake over a complete flapping cycle. When the airfoil is delivering its maximum

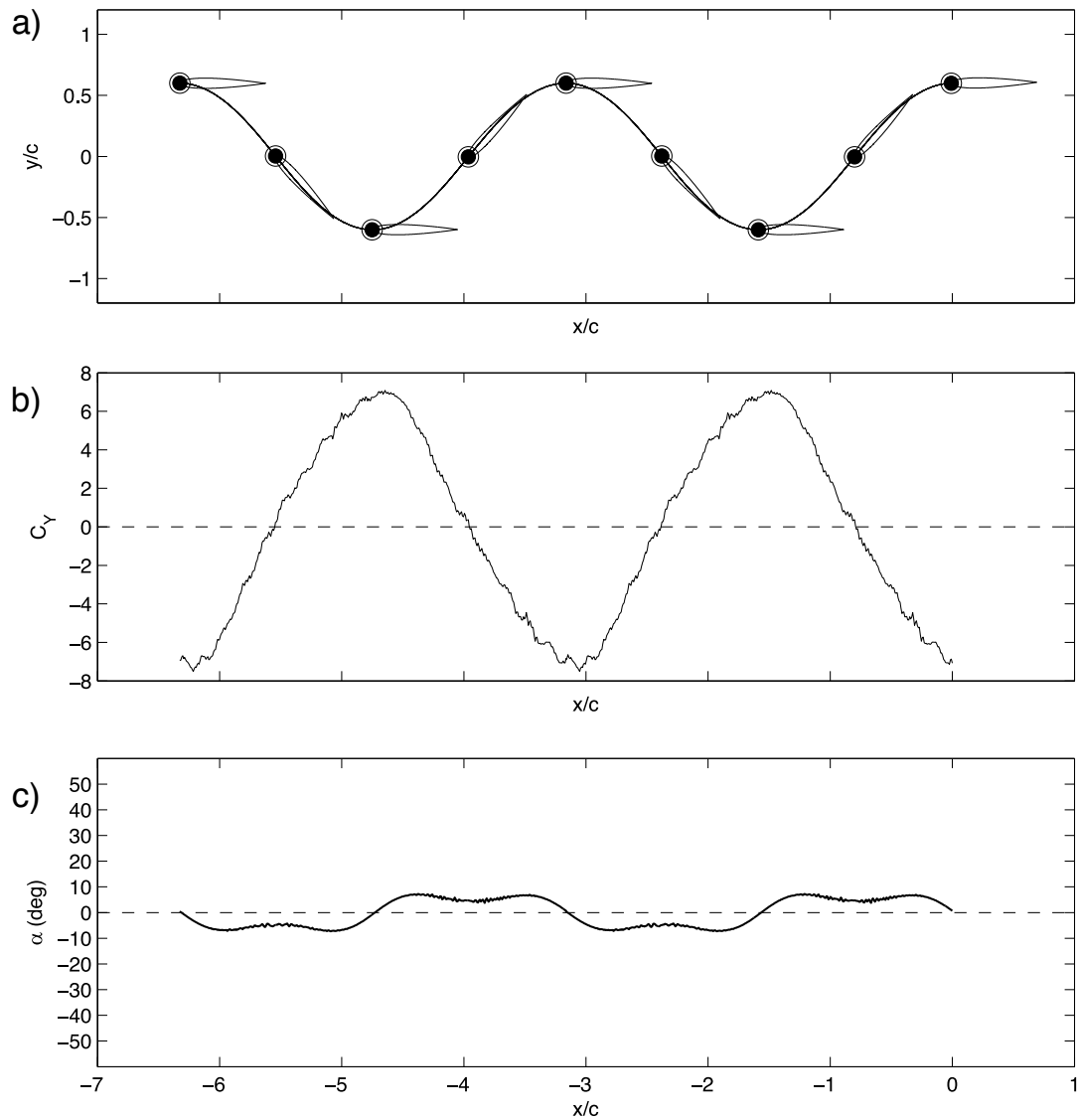


Figure 3.17: “Trajectory plot” for Case 3, High Pitching Amplitude: (a) Airfoil trajectory for $h_0/c = 0.60$, $\theta_0 = 47^\circ$, and $U^* = 3.20$ (b) Transverse force coefficient synchronized with the trajectory. (c) Instantaneous angle of attack synchronized with the trajectory.

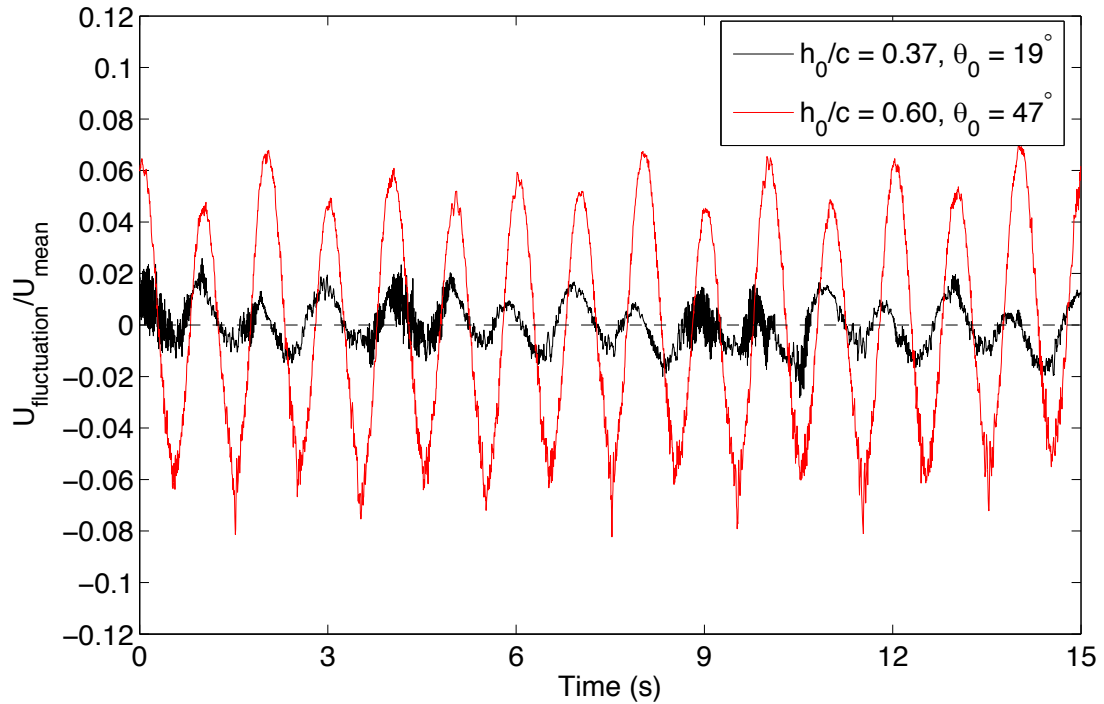


Figure 3.18: Velocity fluctuations, expressed as a fraction of the mean cruising velocity ($U^* = 3.20$), for two operating regimes representing optimal propulsive economy, $h_0/c = 0.37$ and $\theta_0 = 19^\circ$, and a high pitching amplitude motion, $h_0/c = 0.60$ and $\theta_0 = 47^\circ$, illustrating the much larger velocity excursions produced by increasing the pitch amplitude.

propulsive economy, there is no discernible leading edge vortex, indicating that the flow remains attached over the airfoil.

In stark contrast to this configuration, a heaving airfoil produces a large leading edge vortex. The low pressure that exists in this vortex is therefore responsible for the large increase in transverse force that is measured for this operating condition and which does not contribute to the forward motion of the vehicle. In these and all subsequent plots of vorticity contours, red represents positive (counter-clockwise) vorticity, and blue represents negative (clockwise) vorticity. The range of colors represents vorticity magnitudes from $-6s^{-1}$ to $6s^{-1}$.

Similar to the pure heave motion, Case 3, in which the pitching amplitude

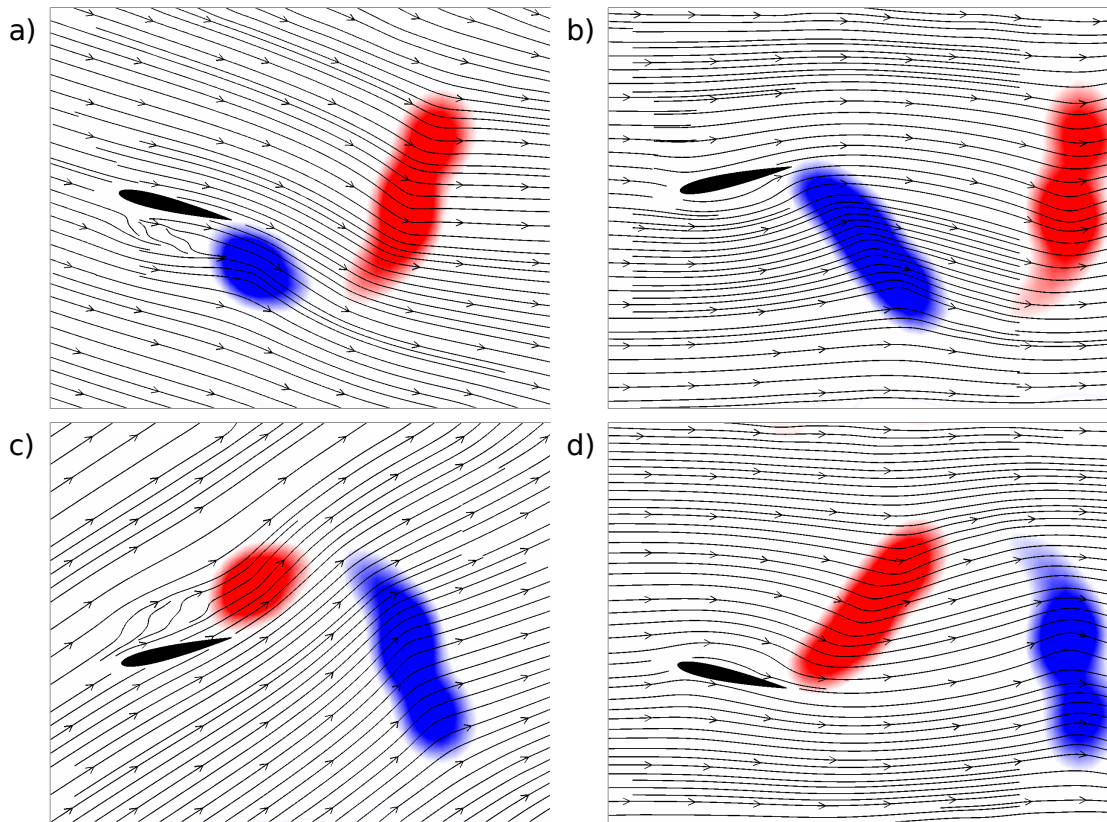


Figure 3.19: Case 1, Optimal Economy: Contours showing the vorticity distribution generated by the airfoil at four instances which represent a complete flapping cycle, beginning with the generation of the clockwise (blue) vorticity. The airfoil is using motion parameters that produce the best propulsive economy for $U^* = 3.20$ ($h_0/c = 0.37$ and $\theta_0 = 19^\circ$). Streamlines are shown in the airfoil reference frame.

is high, also produces significant flow separation. Examination of the vorticity contours for this case, shown in figure 3.21 reveals the presence of a large region of shed vorticity positioned along the upper surface of the airfoil, similar to that generated when the airfoil is actuated in heave only. In this case, again, we can observe that the presence of vorticity in this position is associated with large transverse forces and less economical propulsion.

From these three cases, it seems apparent that the less efficient airfoil motions produce large quantities of “excess vorticity” which do not contribute to

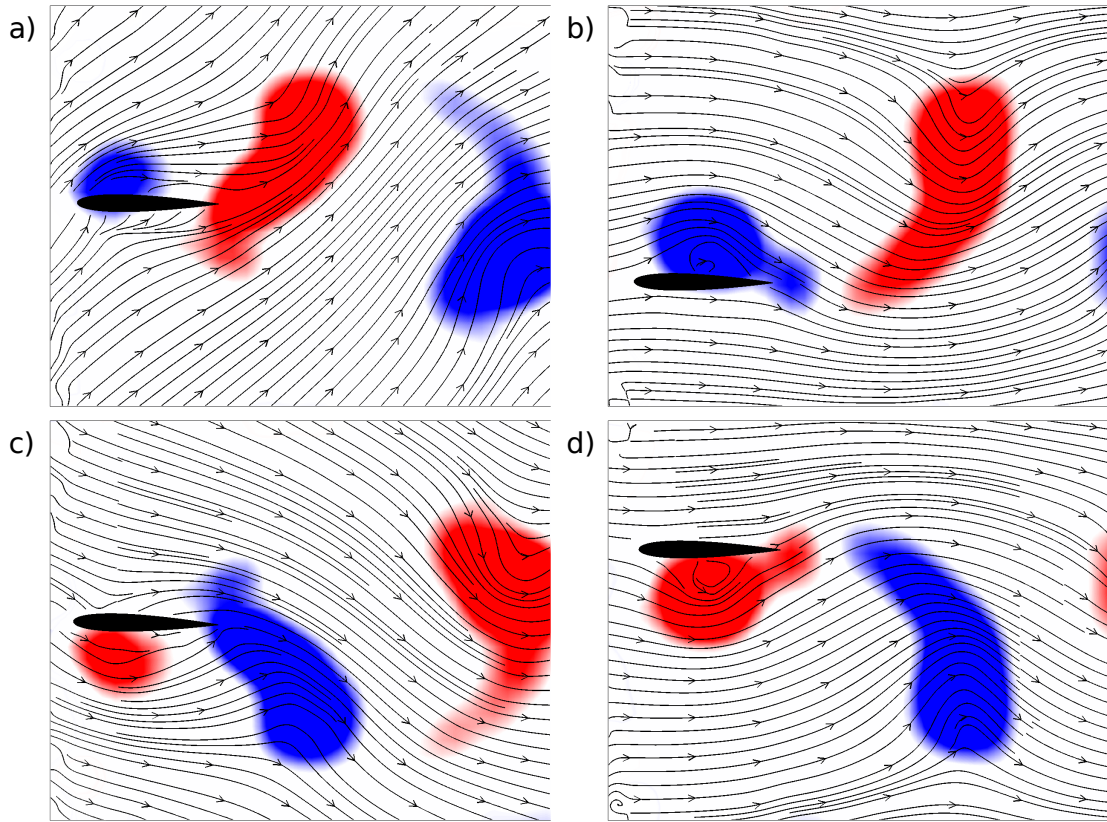


Figure 3.20: Case 2, Pure Heave: Contours showing the vorticity distribution generated by the airfoil at four instances which represent a complete flapping cycle, beginning with the generation of the clockwise (blue) vorticity. The airfoil is executing a pure heave motion that delivers the same forward velocity as the case depicted in figure 3.19 but with greatly reduced efficiency ($h_0/c = 0.57$ and $\theta_0 = 0^\circ$). Streamlines are shown in the airfoil reference frame.

propulsion in the desired travel direction. In order to quantify this effect, we can compute the circulation of the vorticity produced during each cycle, as defined by equation 3.12.

$$\Gamma = \int (\vec{\omega} \cdot d\vec{A}) \quad (3.12)$$

where $\vec{\omega}$ is the vorticity in a given region and $d\vec{A}$ is the area of that region.

Figure 3.22 shows this variation of circulation as a function of time for the

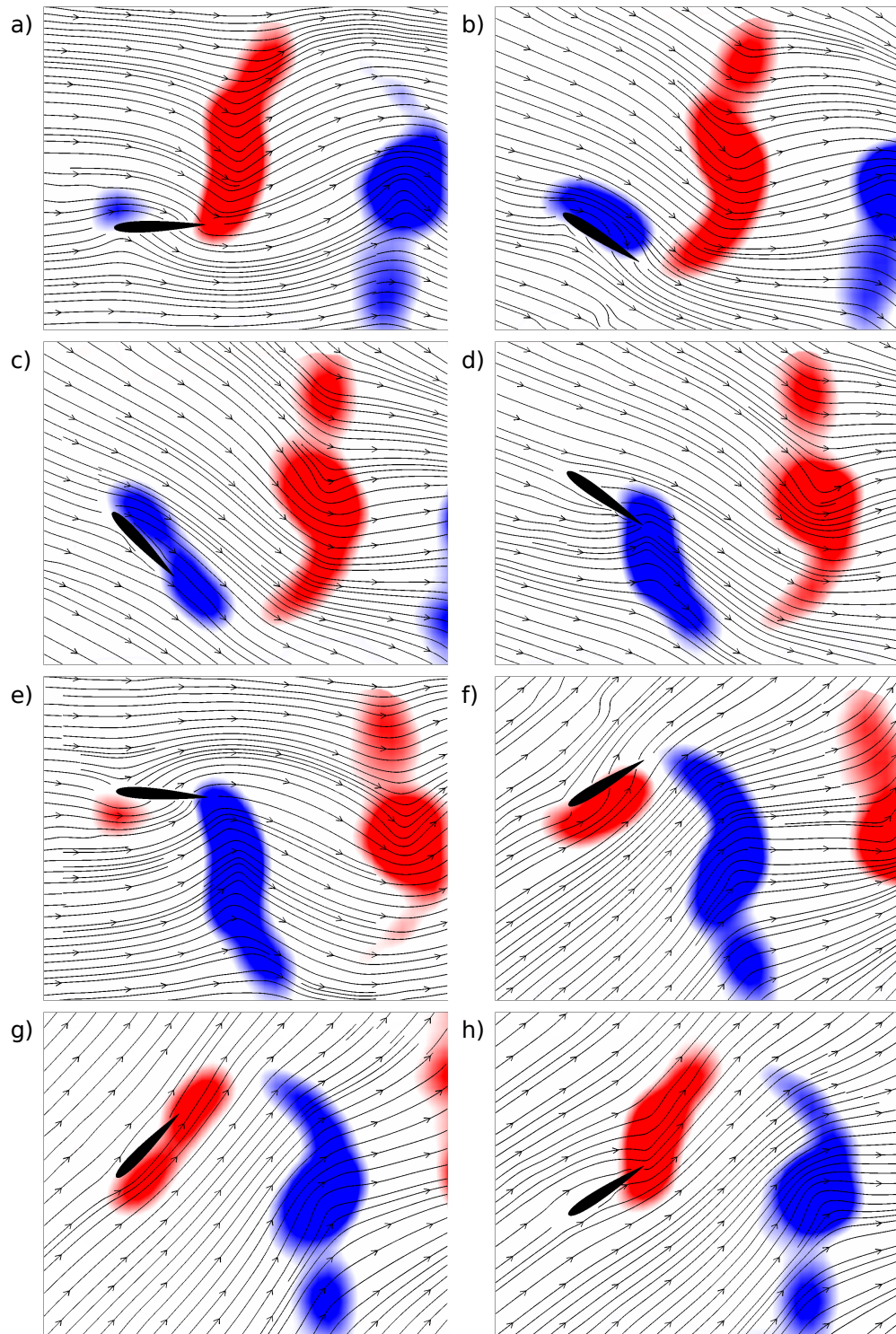


Figure 3.21: Case 3, High Pitch Amplitude: Contours showing the vorticity distribution generated by the airfoil at eight instances which represent a complete flapping cycle. The airfoil is executing a high-pitch amplitude motion ($h_0/c = 0.60$ and $\theta_0 = 47^\circ$) which results in suboptimal propulsive economy for $U^* = 3.20$. Streamlines are shown in the airfoil reference frame.

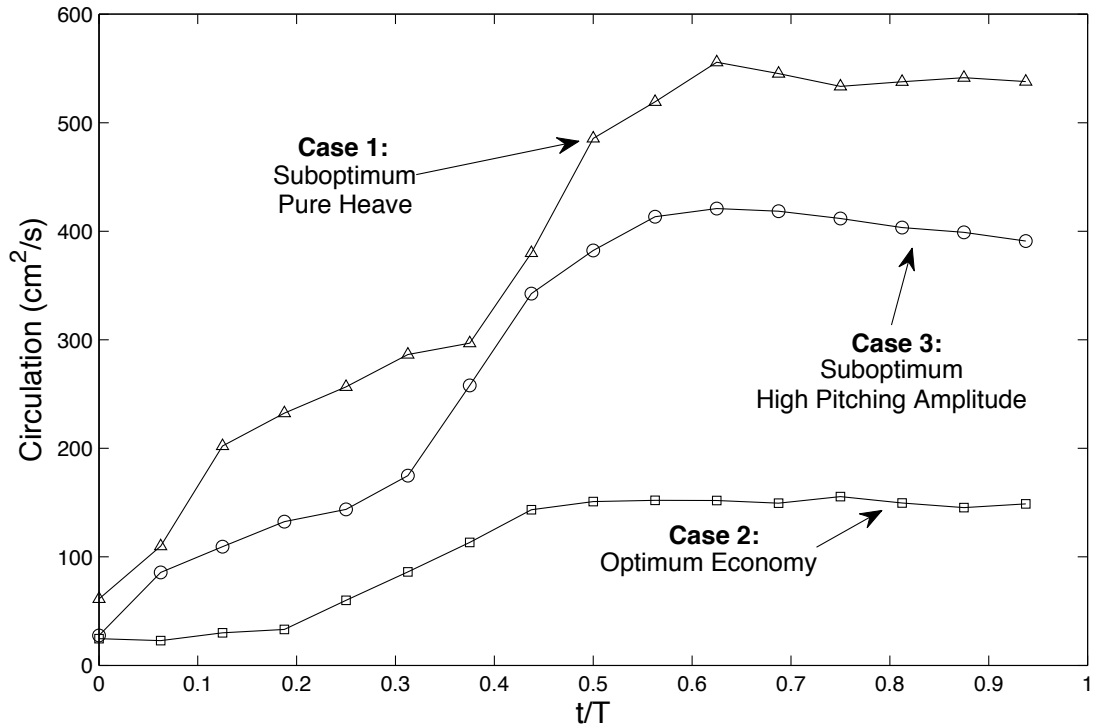


Figure 3.22: Circulation generated by the airfoil during half of a flapping cycle as a function of time for the three cases shown in figure 3.14. Operating points which deliver suboptimal propulsive economy also produce significantly more circulation than the point of optimum economy.

three cases shown in figure 3.14. The circulation shown is the magnitude of the clockwise (blue) vorticity as it evolves over a full flapping cycle. Airfoil kinematics which produce the most efficient propulsion also produce the least circulation. As all three of these cases propel the airfoil at the same velocity, the extra circulation observed for the suboptimal motions represents wasted energy.

The three operating conditions discussed so far suggest that minimizing the leading edge vortex is an important characteristic of efficient propulsion. Further evidence for this claim is provided in figure 3.23, in which the maximum circulation shed by the airfoil during a cycle is plotted against the pitching amplitude. All points shown deliver the same reduced velocity, $U^* = 3.20$, and

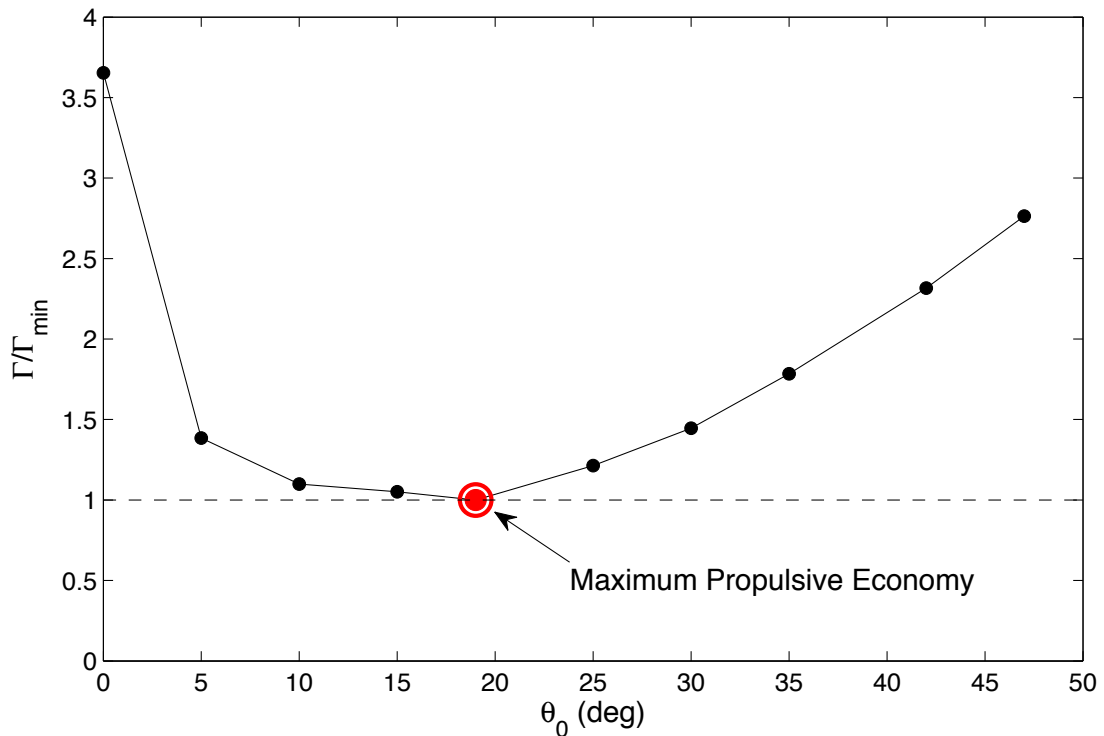


Figure 3.23: Maximum circulation generated by the airfoil as a function of the pitching amplitude, θ_0 , for $U^* = 3.20$. The maximum propulsive economy corresponds to the condition which produces the least overall circulation in each cycle.

therefore the same average thrust force on the body. The pitching amplitude producing maximum economy also produces the smallest amount of circulation per cycle. It seems apparent, then, that the most efficient propulsion schemes are judicious in their use of energy, only generating as much circulation as is needed to propel the body forward. Other, suboptimal motions waste significant energy, which is associated with the generation of additional circulation.

An obvious source for this additional circulation is the production of the leading edge vortex. Figure 3.24 shows the maximum circulation attained by the leading edge vortex before it merges with the vorticity being generated at the trailing edge. This curve follows the same trend shown in figure 3.23, with

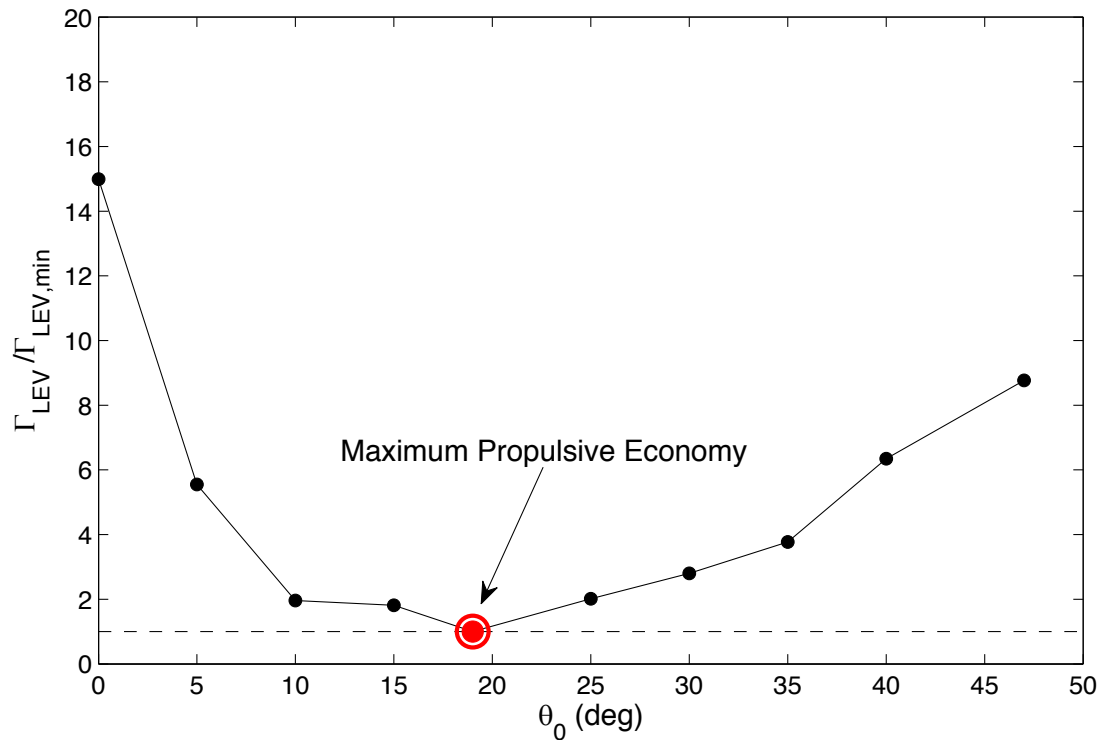


Figure 3.24: Maximum circulation contained in the leading edge vortex as a function of the pitching amplitude, θ_0 , for $U^* = 3.20$. The maximum propulsive economy corresponds to the condition which produces the weakest leading edge vortex.

the minimum circulation in the LEV occurring for the case of optimal propulsive economy and suboptimal operating points producing up to 15 times the circulation in the leading edge vortex.

To further illustrate the changes occurring in the leading edge vortex, we show in figure 3.25 contours of vorticity depicting the point at which the leading edge vortex strength is maximized for several airfoil operating conditions. Each produces the same reduced velocity, $U^* = 3.20$, but uses different pitching amplitudes, θ_0 , to do so. Initially, when $\theta_0 = 0$, and the airfoil executes a purely heaving motion, the LEV is large. The addition of pitch steadily reduces its strength until it effectively disappears when the airfoil operates at maximum

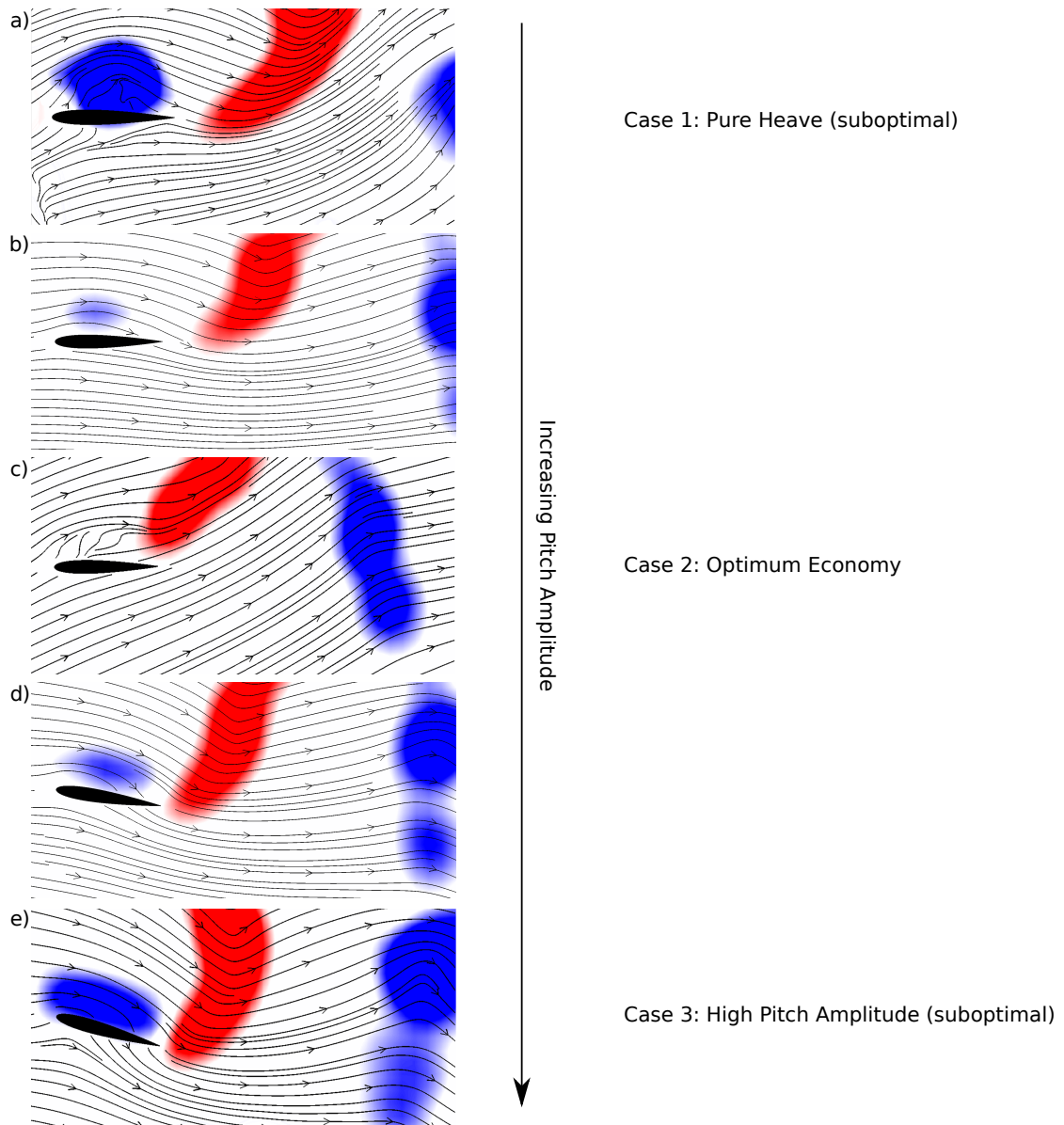


Figure 3.25: Contours of vorticity showing the point at which the leading edge vortex reaches its maximum strength for several motion profiles, all delivering the same reduced velocity, $U^* = 3.20$ (a) Case 1, Pure Heave: $h_0/c = 0.57, \theta_0 = 0^\circ$ (b) $h_0/c = 0.39, \theta_0 = 10^\circ$ (c) Case 2, Optimum Economy: $h_0/c = 0.37, \theta_0 = 19^\circ$ (d) $h_0/c = 0.41, \theta_0 = 30^\circ$ (e) Case 3, High Pitch Amplitude $h_0/c = 0.60, \theta_0 = 47^\circ$

propulsive economy. Beyond this pitching amplitude, however, the LEV resumes growing, eventually developing into the strong vortex shown in figure 3.25(e) for Case 3.

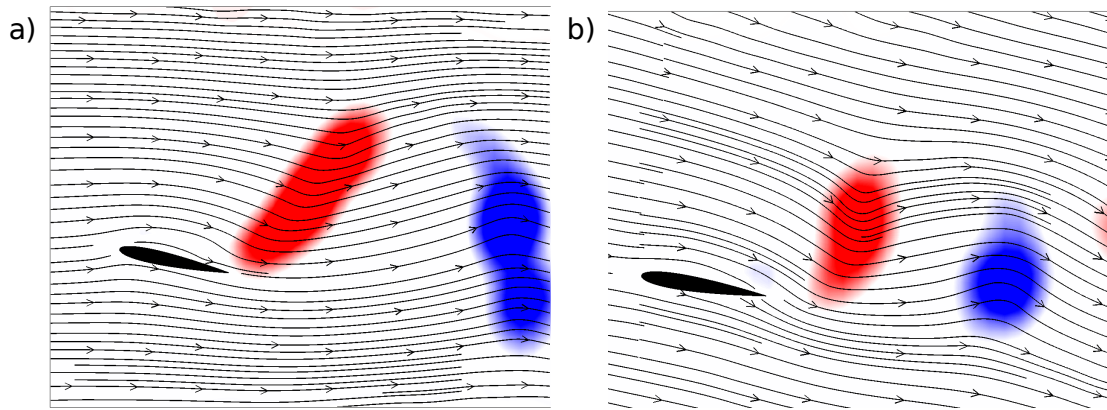


Figure 3.26: Contours of vorticity acquired at approximately the same phase in the flapping cycle for (a) $U^* = 3.20$, $h_0/c = 0.37$, and $\theta_0 = 19^\circ$ and (b) $U^* = 2.10$, $h_0/c = 0.22$, and $\theta_0 = 15^\circ$. Both frames depict operation of the airfoil at the point of optimum economy for the respective reduced velocities. In both cases, the leading edge vortex strength is minimized when propulsive economy is maximized.

Finally, we note that the tendency for the leading edge vortex to be minimized is also persistent across multiple velocity contours, as shown in figure 3.26. Here, the operating point delivering maximum propulsive economy is shown for reduced velocities of $U^* = 2.10$ and $U^* = 3.20$. In both cases, there is no significant leading edge vorticity. The principal difference between the wakes appears to be the extent of the shed vorticity, with the higher velocity motion producing much more elongated vortices. This may be expected, as the airfoil executes a higher amplitude motion in order to produce more thrust, and the trailing edge displacement is consequently larger. The behavior of the sub-optimal propulsive cases for this velocity is also similar, with significant flow separation at operating points away from the optimum.

3.6 Chordwise Variation of Angle of Attack

In §3.4, we discussed Case 3, which drives the airfoil with large pitching and heaving amplitudes. Figure 3.17(c) shows the evolution of the angle of attack, measured at the leading edge of the airfoil, for this case. The maximum value of α attained is approximately 10° . Interestingly, however, we find in §3.5 that there is significant flow separation in this case, despite the small angle of attack. Under static conditions, the flow would be attached along the entire surface of the airfoil. However, in the highly dynamic environment in which the airfoil operates here (figure 3.17a), this may not be true. In fact, the instantaneous angle of attack varies considerably if it is evaluated at different points along the chord of the airfoil. This effect is especially pronounced when the airfoil rotates rapidly as it approaches the upper and lower limits of its heaving motion. Rotation about the leading edge requires all other points along the airfoil chord to move, both in the streamwise and transverse directions.

As a result of this additional heaving motion, the angle of attack increases with position along the airfoil chord, according to equation 3.11 and also illustrated in figure 3.27 for the simplified case of a purely pitching airfoil. In this case, the angle of attack at the pivot point (the leading edge in this example) is given simply by the pitching angle because there is no heaving motion at this point. At all other points along the airfoil chord, however, the rotation creates velocities in the streamwise and transverse directions. The transverse velocity added by rotation is given by equation 3.13, and the streamwise velocity by equation 3.14. Both contribute to the angle of attack via equation 3.15.

$$\dot{y} = -r \cos(\theta)\dot{\theta} \quad (3.13)$$

$$\dot{x} = r \sin(\theta)\dot{\theta} \quad (3.14)$$

$$\alpha_{heave} = \arctan\left(\frac{-\dot{y}(t)}{U_\infty + \dot{x}(t)}\right) \quad (3.15)$$

where r is the distance from the pivot location (the leading edge in all cases discussed here) to the point in question, measured along the airfoil chord.

This heaving contribution to the angle of attack increases as \dot{x} and \dot{y} increase. Since both are dependent on distance from the pivot point, r , and on the rotation rate of the airfoil, $\dot{\theta}$, the effect is more pronounced for points far from the pivot and during portions of the oscillation cycle where the rotation rate is large.

For Case 3, we present the instantaneous angle of attack profiles for three chordwise positions in figure 3.28, which shows that the trailing edge of the airfoil sees an incident flow velocity angle of about 60° , far higher than that at the leading edge. This large variation indicates that it is inappropriate to consider the angle of attack to be a constant quantity across the entire airfoil. The maximum value of α measured at the leading edge does not properly reflect the highly dynamic behavior of the airfoil when it is executing this trajectory.

This phenomenon is similar to that observed in various vertical axis wind turbines, such as the Darrieus design (Darrieus, 1931). In such wind turbines, it is typical to use straight symmetric airfoils mounted vertically to a central rotating shaft. As the ratio of chord length to turbine radius increases, and the

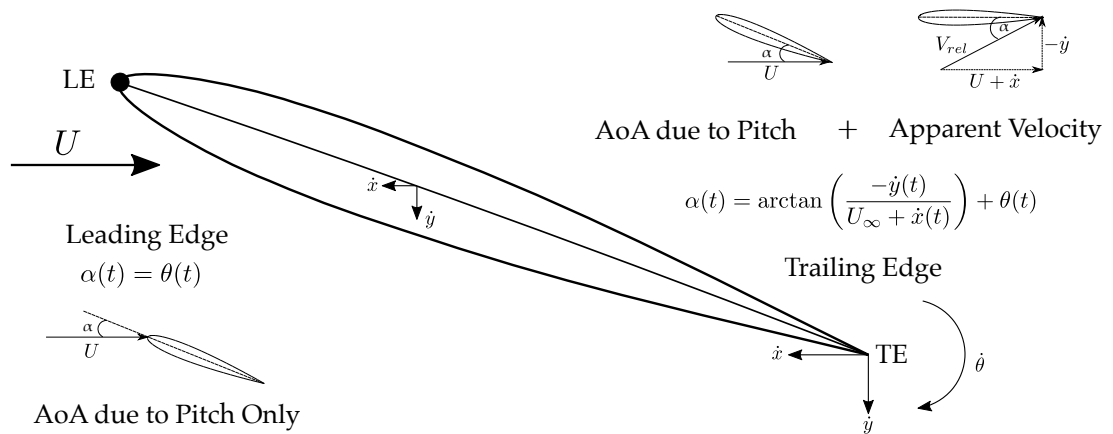


Figure 3.27: Schematic of an airfoil executing a purely pitching motion about its leading edge, illustrating that the angle of attack is dependent on the position along the airfoil chord at which it is calculated. At the pivot point, the airfoil simply rotates, and the angle of attack is equal to the pitching angle. At the trailing edge (and all intermediate points along the chord), the angle of attack is a combination of the pitching angle and the heaving motion that results from rotation.

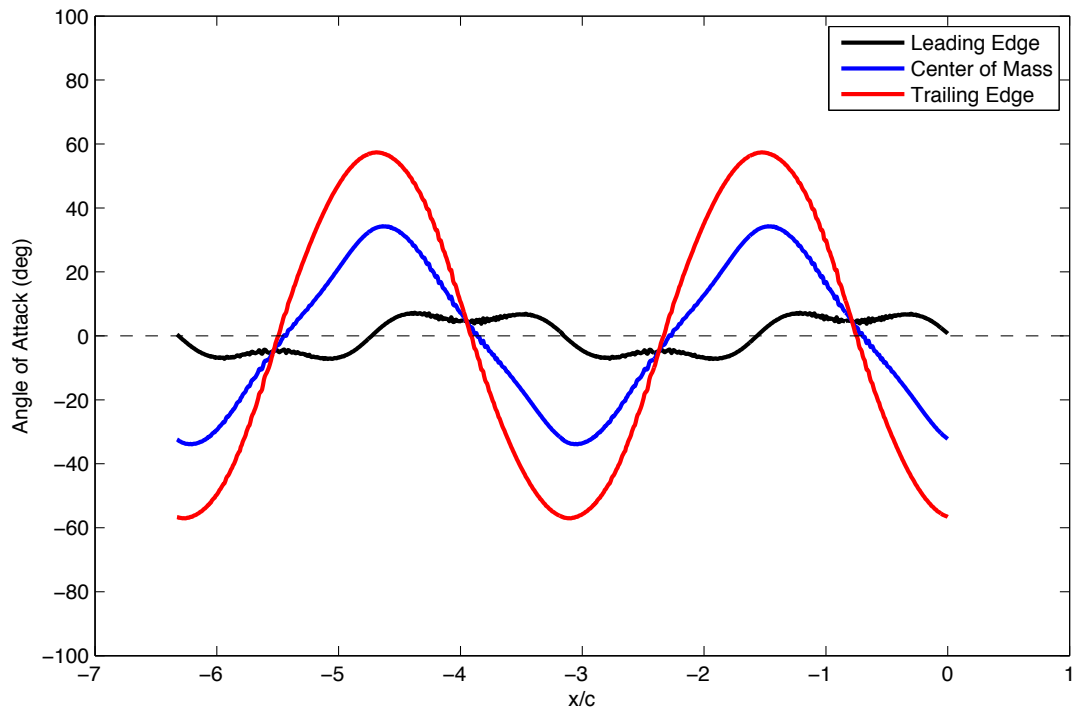


Figure 3.28: Angle of attack over two complete flapping cycles for Case 3: High Pitch Amplitude, calculated at the leading edge, the airfoil center of mass, and the trailing edge. The angle of attack increases substantially as distance from the pivot point increases.

airfoil therefore occupies a greater portion of its curved trajectory at one time, the incident flow velocity seen by the blade at each chordwise position becomes significantly different. Migliore *et al.* (1980) analyzed this situation using conformal mapping and found that this “flow curvature” effect influences the performance of the airfoil in negative ways. Principally, the curvilinear flow causes the airfoil to behave as though it has a built-in virtual angle of attack. When this virtual angle of attack is added to the geometric angle of attack determined by the motion of the airfoil (equation 3.11), the overall angle of attack becomes larger, and the airfoil stalls prematurely.

In our experiment, the airfoil is large compared to its trajectory. Defining the wavelength as the distance traveled by the airfoil in one flapping period, the ratio of airfoil chord to wavelength is 0.42. Consequently, the airfoil physically occupies 42% of its wavelength, a measurement which is analogous to the high chord-to-radius ratio of the wind turbines. In our experiment, the curvilinear flow is a result of airfoil rotation, which is maximized at the extremes of the airfoil’s heaving motion. It does not exist for the case of pure heave, in which the angle of attack is uniform along the entire chord. However, this effect becomes increasingly important as the pitching amplitude is increased and larger angular velocities are needed to turn the airfoil as it reverses direction, eventually leading to large areas of flow separation.

3.7 Conclusions

Oscillating airfoils have attracted considerable recent interest for their possible use as propulsive devices for small vehicles which travel through the air or

underwater. These vehicles have significant practical applications as platforms for scientific remote sensing, reconnaissance, and long-term environmental and disaster monitoring. The great maneuverability and agility of the animals employing flapping techniques has led to interest in understanding the fundamental behavior of airfoil shapes operating in this manner.

The vast majority of studies completed to date, however, have decoupled the airfoil motion from the incoming flow velocity; that is, the velocity of the flow over the airfoil does not necessarily correspond to that which would exist if the airfoil were actually used to propel a vehicle. In an effort to begin exploring the performance of flapping airfoils under more realistic conditions, we have conducted self-propulsion experiments using a cyber-physical fluid dynamics technique. This technique uses force feedback to determine the acceleration of the airfoil at each time step and then to control the flow speed of a water channel so that the freestream flow always reflects the forward velocity at which the airfoil should be traveling. Consequently, we can conduct experiments of indefinite duration and also change experiment parameters such as the virtual drag imposed on the airfoil completely in software.

We employ a NACA 0012 airfoil which undergoes pitching and heaving oscillations, with a pivot point located at its leading edge. Results for reduced velocity and propulsive economy are presented in the form of contour plots as functions of heaving and pitching amplitudes, which we refer to as the heave-pitch diagram. These diagrams are very useful for determining relationships between the various parameters of interest. In general, the steady-state velocity achieved by the airfoil is more sensitive to the heaving amplitude than to the pitching amplitude. However, we find that the addition of even moder-

ate amounts of pitching motion can significantly reduce the energy required to move the airfoil at a given speed. Maximum propulsive economy occurs for moderate values of the maximum angle of attack attained by the airfoil during its motion, just before stall occurs. There is also excellent agreement between this operating point and the point at which the transverse forcing on the airfoil is minimized, suggesting that reducing the amount of power expended to oscillate the airfoil in this direction is key to achieving good performance.

Particle image velocimetry measurements of the wake show that high efficiency is also strongly correlated with minimizing the strength of the leading edge vortex and the total circulation produced by the airfoil during a cycle. The separated flow represented by the LEV contributes to inefficient propulsion, including the generation of transverse forces. The excess circulation produced is not required to propel the airfoil at the desired speed and is therefore associated with wasted energy.

As the pitching amplitude is changed away from the optimum point in either direction, the amount of circulation produced increases, particularly in the leading edge vortex, the transverse force becomes larger, and the propulsive economy decreases. We find that the propulsive economy is quite sensitive to the selection of the pitching amplitude.

The results we describe here appear to be generally applicable to airfoils operating at other velocities and drag coefficients. We observe the same characteristics of optimal propulsion regardless of these parameters: small transverse forces, minimal flow separation, and minimum total circulation generated.

The performance of flapping airfoils as propulsive devices has been exten-

sively explored in the tethered configuration, with results indicating that they show great promise for use in small vehicles. This study examines a more realistic self-propelled condition, in which the cruising velocity is determined by the physics of the vehicle and its motions. We hope that studies such as these will be useful to the design and development of small, autonomous flying and swimming vehicles.

This work was supported by the Air Force Office of Scientific Research Grant No. FA9550-15-1-0243, monitored by Dr. Douglas Smith.

REFERENCES

- ABBOTT, I.H. & VON DOENHOFF, A.E. 1959 *Theory of Wing Sections*. Dover.
- ALBEN, S. & SHELLEY, M. 2005 Coherent locomotion as an attracting state for a free flapping body. *Proc. Nat. Acad. Sci.* **102** (32), 11163–11166.
- ALBEN, S., WITT, C., BAKER, T.V., ANDERSON, E. & LAUDER, G.V. 2012 Dynamics of freely swimming flexible foils. *Phys. Fluids* **24**, 051901.
- ANDERSON, J.M., STREITLIEN, K., BARRETT, D.S. & TRIANTAFYLLOU, M.S. 1998 Oscillating foils of high propulsive efficiency. *J. Fluid Mech.* **360**, 41–72.
- ASSELIN, D.J., YOUNG, J.D. & WILLIAMSON, C.H.K. 2018 Addition of passive dynamics to a heaving airfoil to improve performance. *J. Fluid Mech.* (in preparation) .
- BETZ, A. 1912 Ein beitrag zur erklärung des segelfluges. *Zeitschrift für Flugtechnik und Motorluftschiffahrt* **3** (21), 269–272.
- BUCHHOLZ, J.H.J. & SMITS, A.J. 2008 The wake structure and thrust performance of a rigid low-aspect-ratio pitching panel. *J. Fluid Mech.* **603**, 331–365.
- DARRIEUS, G.J.M. 1931 Turbine having its rotating shaft transverse to the flow of the current (U.S. Patent No. 1,835,018).
- ELOY, C. 2012 Optimal strouhal number for swimming animals. *J. Fluids Struct.* **30**, 205–218.
- HEATHCOTE, S. & GURSUL, I. 2007 Flexible flapping airfoil propulsion at low reynolds numbers. *AIAA J.* **45** (5), 1066–1079.
- JONES, K.D., BRADSHAW, C.J., PAPADOPOULOS, J. & PLATZER, M.F. 2005 Bio-inspired design of flapping-wing micro air vehicles. *Aero. J.* pp. 365–393.
- KATZMAYR, R. 1922 Effect of periodic changes of angle of attack on behaviour of airfoils. *Tech. Rep.*. National Advisory Committee on Aeronautics.
- KIM, B., PARK, S.G., HUANG, W. & SUNG, H.J. 2016 Self-propelled heaving and pitching flexible fin in a quiescent flow. *Inter. J. Heat and Fluid Flow* **62**, 273–281.
- KNOLLER, R. 1909 Die gesetze des luftwiderstandes. *Flug und Motortechnik* **3** (21), 1–7.
- LAUDER, G.V., ANDERSON, E.J., TANGORRA, J. & MADDEN, P.G.A. 2007 Fish biorobotics: kinematics and hydrodynamics of self-propulsion. *J. Exp. Bio.* pp. 2767–2780.

- LEWIN, G.C. & HAJ-HARIRI, H. 2003 Modelling thrust generation of a two-dimensional heaving airfoil in a viscous flow. *J. Fluid Mech.* **492**, 339–362.
- MACKOWSKI, A.W. 2014 A cyber-physical approach to experimental fluid mechanics. PhD thesis, Cornell University.
- MACKOWSKI, A.W. & WILLIAMSON, C.H.K. 2011 Developing a cyber-physical fluid dynamics facility for fluid-structure interaction studies. *J. Fluids Struct.* **27** (5), 748–757.
- MACKOWSKI, A.W. & WILLIAMSON, C.H.K. 2015 Direct measurement of thrust and efficiency of an airfoil undergoing pure pitching. *J. Fluid Mech.* **765**, 524–543.
- MCCROSKEY, W.J. 1982 Unsteady airfoils. *Annu. Rev. Fluid Mech.* **14** (1), 285–311.
- MIGLIORE, P.G., WOLFE, W.P. & FANUCCI, J.B. 1980 Flow curvature effects on darrieus turbine blade aerodynamics. *J. Energy* **4** (2), 49–55.
- MOORED, K.W. & QUINN, D.B. 2017 Inviscid scaling laws of a self-propelled pitching airfoil. *J. Fluid Mech.* .
- OLIVIER, M. & DUMAS, G. 2016 Effects of mass and chordwise flexibility on 2d self-propelled flapping wings. *J. Fluids Struct.* **64**, 46–66.
- PLATZER, M.F., JONES, K.D., YOUNG, J., & LAI, J.C.S. 2008 Flapping-wing aerodynamics: Progress and challenges. *AIAA J.* **46** (9), 2136–2149.
- READ, D.A., HOVER, F.S. & TRIANTAFYLLOU, M.S. 2003 Forces on oscillating foils for propulsion and maneuvering. *J. Fluids Struct.* **17**, 163–183.
- ROZHDESTVENSKY, K.V. & RYZHOV, V.A. 2003 Aerohydrodynamics of flapping-wing propulsors. *Prog. Aerosp. Sci.* **39** (8), 585–633.
- SPAGNOLIE, S.E., MORET, L., SHELLEY, M.J. & ZHANG, J. 2010 Surprising behaviors in flapping locomotion with passive pitching. *Phys. Fluids* **22**, 041903.
- THIELICKE, W. 2014 The flapping flight of birds - analysis and application. PhD thesis, Rijksuniversiteit Groningen.
- THIELICKE, W. & STAMHUIS, E.J. 2014a Pivlab – towards user-friendly, affordable and accurate digital particle image velocimetry in matlab. *J. Open Research Software* **2** (1).
- THIELICKE, W. & STAMHUIS, E.J. 2014b Pivlab - time-resolved digital particle image velocimetry tool for matlab (version: 1.40).

- THIRIA, B. & GODOY-DIANA, R. 2010 How wing compliance drives the efficiency of self-propelled flapping flyers. *Phys. Rev. E* **82**, 015303.
- VANDENBERGHE, N., CHILDRESS, S. & ZHANG, J. 2006 On unidirectional flight of a free flapping wing. *Phys. Fluids* **18**, 014102.
- VANDENBERGHE, N., ZHANG, J. & CHILDRESS, S. 2004 Symmetry breaking leads to forward flapping flight. *J. Fluid Mech.* **506**, 147–155.
- WANG, S., HE, G. & ZHANG, X. 2016 Self-propulsion of flapping bodies in viscous fluids: Recent advances and perspectives. *Acta Mech. Sin.* **32** (6), 980–990.
- WEN, L., WANG, T.M., WU, G.H. & LIANG, J.H. 2012 Hydrodynamic investigation of a self-propelled robotic fish based on a force-feedback control method. *Bioinspir. Biomim.* **7**, 036012.
- YEH, P.D. & ALEXEEV, A. 2016 Effect of aspect ratio in free-swimming plunging flexible plates. *Computers and Fluids* **124**, 220–225.
- YOUNG, J. & LAI, J.C.S. 2007 Mechanisms influencing the efficiency of oscillating airfoil propulsion. *AIAA J.* **45** (7), 1695–1702.
- ZHANG, X., NI, S., WANG, S. & HE, G. 2009 Effects of geometric shape on the hydrodynamics of a self-propelled flapping foil. *Phys. Fluids* **21**, 103302.